

Filamentary Threshold Switching in Niobium Oxides



A thesis submitted for the degree of Doctor of
Philosophy of The Australian National University.

Shimul Kanti Nath

May 5, 2021

© Copyright by [Shimul Kanti Nath] [2021]

All Rights Reserved

Dedication

To my mother Mrs. Anu Radha Debi

Declaration

I declare that this thesis has been composed by me and that the work has not been submitted by me, in whole or in part, for any other degree or professional qualification. I further note that the experimental chapters in this thesis are based on journal publications that I have authored or co-authored during the course of my PhD at the Australian National University. While these received input from collaborators and coworkers, I was primarily responsible for the planning and executing the experimental work, for analysing the results and for drafting the manuscript. A complete list of these and related publications is given in the "List of Publications".

Shimul Kanti Nath

May 5, 2021

Acknowledgements

I would like to thank the people who provided their unwavering support and encouragement, and without whom it would not be possible to complete this journey.

First and foremost, I want to express my deep sense of gratitude and indebtedness to the chair of my supervisory panel, Prof. Robert Elliman, whose insight and knowledge into the subject matter and great mentorship steered me through this research. With both the utmost enthusiasm and patience, he taught me how to design experiments, and then understand and analyse the data from different perspectives. Apart from being a fine scientist, he is a compassionate and sincere human being who always provided instant support whenever needed. His thoughtful comments and recommendations greatly helped to improve my understanding and explore the details of my PhD topic.

I would like to acknowledge the great support received from my primary supervisor, Dr. Sanjoy Nandi, from the beginning of this journey and sincerely thank him for his wonderful guidance, and hands-on trainings on device fabrication and electrical measurements. He has been a great mentor and I am deeply impressed by his supportive nature and caring attitude. I am grateful for his encouragement and the invaluable suggestions during the period of this thesis work.

I am grateful to my associate supervisor Dr. Tom Ratcliff for his excellent cooperation, encouragement and support for different experiments and data analysis. His comments and feedback on my manuscripts and thesis were invaluable for improving the contents in these documents. I am thankful for our friendly chats during the tea breaks and for his personal support in my academic endeavours.

My heartfelt gratitude to the benefactors of the ANU International PhD Scholarship and the COVID Extension Scholarship for their generous support which made it possible to attend and complete my PhD program.

I would like to express gratitude to my collaborators, Dr. Shuai (Jack) Li for the hands-on training on FIB and EBL, Associate Prof. Xinjun Liu for helping with LT Spice Modelling, and Dr. Assaad El-Helou and Prof. Peter Raad for their support in thermo-reflectance

imaging.

I feel I owe a great deal to many people of ANFF, ANU CAM and UNSW whose technical support is vital for our working. My grateful thanks to the following people from these institutes: Dr. Kaushal Vora, Dr. Li Li, Ms Gayatri Vaidya, Dr. Mark Lockrey, Dr. Fouad Karouta, Dr. Felipe Kremer and Dr. Bill Gong for their technical support for thin films deposition, device fabrication, FIB, TEM and XPS analysis.

I would also like to thank Ms Julie Arnold, Ms Karen Nulty and Ms Liudmila Mangos for being friendly and supportive in dealing with administrative issues from the first day of my enrolment at ANU.

On a personal level, I would like to express gratitude to Prof. Lan Fu, Prof. Chennupati Jagadish, Prof. Hoe Tan, A/Prof. Jennifer Wong-Leung, Dr. Ziyuan Li and Dr. Siva Karuturi for their continuous encouragement and advices during the PhD program.

I want to convey my regards and gratitude to all of my group members and friends from ANU, including James, Sujan, Helen, Eve, Siti, Harry, Dipankar, Vidur, Sonachand and Zahra, to name a few.

Special thanks to my wife Nishita Chowdhury for her encouragement and great support during my PhD journey. Without her endless support and sacrifice it would not be possible to complete this thesis. I am grateful to her and feel proud of her own achievements as she works towards her own PhD.

Finally, I would like to express endless gratitude to my parents, Mrs. Anu Radha Debi and Mr. Prafulla Kumar Nath, who shaped my dreams during my teenage years, supported me in every steps of life, and constantly encouraged me to achieve my goals. Thanks to my extended family and friends for their continuous support and encouraging me in all spheres of my life.

Author

Shimul Kanti Nath

List of Publications

1. **S. K. Nath**, S. K. Nandi, T. Ratcliff and R. G. Elliman, ‘Engineering the threshold switching response of Nb₂O₅-based memristors by Ti doping’, **ACS Applied Materials and Interfaces**, Vol. 13, No. 2, pp. 2845-2852 (2021).
2. **S. K. Nath**, S. K. Nandi, A. E. Helou, X. Liu, S. Li, T. Ratcliff, P. E. Raad and R. G. Elliman, ‘Schottky barrier induced asymmetry in the negative differential resistance response of Nb/NbO_x/Pt cross-point devices’, **Physical Review Applied**, Vol. 13, No. 6, pp. 064024 (2020).
3. **S. K. Nath**, S. K. Nandi, S. Li, and R. G. Elliman, ‘Metal-oxide interface reactions and their effect on integrated resistive/threshold switching in NbO_x’, **Nanotechnology**, Vol. 31, No. 23, pp. 235701 (2020).
4. S. K. Nandi, **S. K. Nath**, A. E. Helou, S. Li, T. Ratcliff, M. Uenuma, P. E. Raad and R. G. Elliman, ‘Electric field and current induced electroforming modes in NbO_x’, **ACS Applied Materials and Interfaces**, Vol. 12, No. 7, pp. 8422-8428 (2020).
5. **S. K. Nath**, S. K. Nandi, S. Li, and R.G. Elliman, ‘Detection and spatial mapping of conductive filaments in metal/oxide/metal cross-point devices using a thin photoresist layer’, **Applied Physics Letters**, Vol. 114, pp. 062901 (2019).
6. S. K. Nandi, **S. K. Nath**, A. E. Helou, S. Li, X. Liu, P. E. Raad and R. G. Elliman, ‘Current localisation and redistribution as the basis of discontinuous current controlled negative differential resistance in NbO_x’, **Advanced Functional Materials**, Vol. 29, Issue 50, pp.1906731 (2019).
7. S. Li, X. Liu, S. K. Nandi, **S. K. Nath**, and R. G. Elliman, ‘Origin of current-controlled

negative differential resistance modes and the emergence of composite characteristics with high complexity', **Advanced Functional Materials**, Vol. 29, Issue 44, pp. 1905060 (2019).

8. X. Liu, P. Zhang, **S. K. Nath**, S. Li, S. K. Nandi, and R. G. Elliman, 'Understanding and exploiting composite negative differential resistance in niobium oxide memristors', (submitted).

Conference Presentations

1. **S. K. Nath**, S. K. Nandi, A. Helou, S. Li, P. E. Raad and R. G. Elliman, ‘Distinct modes of filament formation in Niobium Oxide’, presented (oral) in ‘International Conference on Nano Science and Nanotechnology (ICONN)’, 09 February -13 February 2020, Brisbane, Australia.
2. S. K. Nandi, **S. K. Nath**, X. Liu, S. Li, A. Helou, P. E. Raad and R. G. Elliman, ‘Electroforming and spatial distribution of conductive filaments in NbO_x ’, presented (oral) in ‘International Conference on Memristive Materials, Devices & Systems (MEMRISYS)’, 08-11 July 2019, Dresden, Germany.
3. **S. K. Nath**, S. K. Nandi, S. Li, and R.G. Elliman, ‘Threshold switching in NbO_x studied by impedance spectroscopy’, presented (poster) in International Conference on Nano Science and Nanotechnology (ICONN), 29 January -2 February 2018, Wollongong, Australia.

Abstract

Two-terminal metal/oxide/metal (MOM) structures are known to exhibit characteristic resistance changes when subjected to electrical stress, i.e., voltage or current stimuli. The resistance changes of interest include both non-volatile memory and volatile threshold switching behaviour, as well as combination of these responses which are of interest as active elements in non-volatile memory arrays and neuromorphic computing. While volatile threshold switching has been observed in many materials and device structures, two terminal MOM devices using vanadium oxides (VO_x) and niobium oxides (NbO_x) have attracted particular attention due to their simple structure and reliable threshold switching characteristics.

The non-volatile and volatile resistance changes in MOM structures are typically initiated by a one-step electroforming process that forms a filamentary conduction path which subsequently governs the device characteristics. Knowledge about the structure, composition and spatial distribution of these filaments is essential for a full understanding of filamentary resistive/threshold-switching and for effective modelling and optimisation of associated devices. Additionally, NbO_x -based devices exhibit a wide range of resistive and threshold switching responses that critically depend on operating condition, composition and device geometry. Thus, a proper understanding of these factors is important for achieving reliable switching with desired characteristics.

This thesis focuses on understanding the electroforming process and subsequent threshold switching responses in NbO_x by employing numerous techniques, including electrical testing and in-situ thermo-reflectance imaging. At first, a simple means of detecting and spatially mapping conductive filaments in MOM cross-point devices is introduced, and the utility of this technique is demonstrated to identify distinct modes of electroforming in low- and high-conductivity NbO_x films. After that, the role of metal/oxide interface reactions on the post-forming characteristics of reactive-metal/ Nb_2O_5 /Pt devices is demonstrated. Specifically, devices are shown to exhibit stable threshold switching under negative bias but the response under positive bias depends on the choice of metal. Based on thermodynamic data and lumped element modelling, these effects are attributed to the formation of a metal-oxide

interlayer and its response to field-induced oxygen exchange. Then, the threshold switching and current-controlled negative differential resistance (NDR) characteristics of cross-point devices fabricated from undoped Nb_2O_5 and Ti-doped Nb_2O_5 are compared. In particular it is shown that doping offers an effective means of engineering the device response, including the device reliability, the threshold and hold voltages, the hysteresis window and the magnitude of the negative differential resistance. Based on temperature dependent current-voltage characteristics and lumped-element modelling, these effects are attributed to doping-induced reductions in the device resistance and its rate of change with temperature. Finally, the physical origin of a discontinuous ‘snapback’ NDR is investigated. Specifically, it is shown that the snapback response is a direct consequence of current localisation and redistribution within the oxide film. Furthermore, it is demonstrated that material and device dependencies are consistent with predictions of a two-zone parallel memristor model of NDR which is based on a non-uniform current distribution after electroforming.

These results advance the current understanding of the threshold switching response in amorphous NbO_x films and provide a strong basis for engineering devices with specific NDR characteristics. Significantly, these results also resolve a long-standing controversy about the origin of the snapback response.

Contents

Dedication	i
Declaration	ii
Acknowledgements	iii
List of Publications	v
Conference Presentations	vii
Abstract	viii
1 Introduction	1
1.1 Motivation	1
1.1.1 From von Neumann to neuromorphic computing	1
1.1.2 Emerging areas in hardware-based neuromorphic computing	3
1.1.3 Memristor-based neuromorphic computing	4
1.2 Overview of this thesis	5
2 Background	8
2.1 Memristive switching in two terminal MOM structures	8
2.1.1 Non-volatile memory switching	9
2.1.2 Threshold switching or Current-controlled NDR	10
2.1.3 Hybrid threshold-memory (1S1M) switching	11
2.2 Current transport properties in dielectric oxide films	12
2.2.1 Interface-controlled conduction	12
2.2.2 Bulk-limited conduction	14
2.3 Metal-insulator Transition	16
2.3.1 Mott transition	16

2.3.2	Peierls Transition	17
2.3.3	Anderson Localisation	18
2.4	Material properties and memristive switching responses of the Nb-O system .	18
2.4.1	The Nb-O system	18
2.4.2	Switching phenomena in Niobium Oxides	23
2.5	State of the art	24
2.5.1	Understanding the electroforming process in MOM structures	24
2.5.2	Material and device dependencies of memristive switching in MOM structures	25
2.5.3	The physical origin of diverse threshold switching modes in NbO _x . .	27
3	Experimental and Modelling Details	29
3.1	Device Fabrication	29
3.2	Thin Films Deposition and Analysis	32
3.2.1	Electron-beam Evaporation	32
3.2.2	Sputter Deposition	32
3.2.3	Compositional Analysis	33
3.2.4	X-ray Photoelectron Spectroscopy	34
3.2.5	Crystallinity of the films	34
3.3	Electrical Measurements	35
3.4	In-situ Temperature Mapping	35
3.5	Modelling of Device Behaviour	37
4	Electroforming in Niobium Oxides: Filament detection and analysis	40
4.1	Experiments	41
4.2	Electroforming and filament detection	41
4.3	Sensitivity of the filament detection technique: Finite Element Modelling . .	43
4.4	Utility of the filament detection technique	45
4.4.1	Influence of device geometry on the stochastic nature of forming . .	45
4.4.2	Distinct modes of electroforming depending on oxide stoichiometry .	47
4.5	Electroforming in sub-stoichiometric NbO _x and in-situ temperature mapping	50
4.6	Finite Element Modelling	51
4.7	Summary	53
5	Threshold Switching Reliability: Role of metal/oxide interface reactions	55
5.1	Experiments	55
5.2	Current-controlled NDR characteristics	56

5.3	Voltage-controlled switching characteristics	57
5.4	Role of Metal/Oxide reactions on the switching response	58
5.5	Modelling of the observed switching phenomena	60
5.6	Switching in Pt/Nb ₂ O ₅ /Pt structures	63
5.7	Summary	64
6	Dopant-controlled threshold switching and S-type NDR	65
6.1	Experiments	65
6.2	Thin Films Analysis	67
6.3	Electroforming and the switching response	69
6.4	Temperature dependence	71
6.5	Lumped Element Modelling	72
6.6	Summary	75
7	Physical origin of the discontinuous ‘snapback’ NDR	76
7.1	Experimental Methods	77
7.2	Effect of film conductivity on NDR modes	77
7.3	In-situ temperature mapping	79
7.4	Area dependence of NDR modes	81
7.5	Thickness dependence of NDR modes	82
7.6	Temperature dependence of NDR modes	84
7.7	Discussion	84
7.8	Summary	85
8	Asymmetric NDR and the role of interface barriers	86
8.1	Experiments	86
8.2	Electroforming and NDR characteristics	87
8.3	In-situ temperature mapping	89
8.4	Schottky barriers and polarity dependent conduction	90
8.5	Effect of oxide stoichiometry and device scaling	92
8.6	Modelling of asymmetric NDR characteristics	93
8.7	Summary	96
9	Conclusion and outlook	98
9.1	Summary and Conclusion	98
9.2	Future research	101

9.2.1	Detailed understanding of the nature of Nb/Nb ₂ O ₅ interface reactions and their effect on threshold switching	101
9.2.2	Micro-structural analysis of the threshold switching volume	102
9.2.3	Understanding the composite NDR characteristics observed in NbO _x and investigate their dynamical characteristics	102
A	Appendix	104
A.1	Parameters used in the simulation of the parallel-memristor model in Chapter 3	104
A.2	Further example of edge effect in MOM structures	105
A.3	Forming voltage distribution for low- and high- conductivity NbO _x films . . .	105
A.4	Polarity dependent current-controlled responses in reactive metal/Nb ₂ O ₅ /Pt	106
A.5	List of Possible Reactions at 298.15K using thermodynamic analysis	106
A.6	Device-to-device and cycle-to-cycle variability: threshold switching parameters of undoped and Ti-doped Nb ₂ O ₅ devices	108
A.7	Bipolar resistive switching observed in Ti/TiO ₂ /Pt structures	109
A.8	Switching dynamics of undoped Nb ₂ O ₅ and Ti:Nb ₂ O ₅ (Ti/Nb ~ 0.1) devices	110
A.9	Area and thickness dependent forming currents in the sub-stoichiometric NbO _x films	113
	Bibliography	114

List of Figures

1.1	(a-b) Schematic representation showing comparison between von Neumann computing architecture, and the brain computing system respectively, and (c) artificial neuron architecture (reproduced from Ref. [2, 3]).	2
1.2	Schematic representation of the four fundamental circuit elements, namely: resistor, capacitor, inductor and memristor [27].	4
2.1	Schematics of the I-V curves for memory switching (a) unipolar switching, and (b) bipolar switching.	9
2.2	Schematics of the I-V curve for volatile threshold switching: (a) voltage-controlled mode, and (b) current-controlled mode.	10
2.3	(a) Schematic of the I-V curve for hybrid threshold-memory (1S1M) switching behaviour, and (b-e) schematic diagrams of the operating mechanism of 1S1M switching at different bias voltages indicated in Fig. 2.3(a). TE and BE represent the top electrode and bottom electrode respectively in a two terminal MOM structure (reproduced from Ref. [61]).	11
2.4	Schematics of the energy band diagram for interface-controlled and bulk-limited conduction in MOM structures: (a) Schottky emission and Fowler-Nordheim tunnelling, (b) direct tunnelling, (c) Poole-Frenkel emission, and (d) hopping conduction.	12
2.5	Band diagram of Mott-Hubbard Insulator (reproduced from Ref.[67]).	16
2.6	Dimerisation in a one-dimensional chain of atoms.	17
2.7	Schematic representation of different charge states of niobium (reproduced from Ref. [101]).	19
2.8	Phase diagram of Nb-O system (reprinted from Ref. [101]).	19
2.9	Crystal structure of NbO ₂ : (a) tetragonal, and (b) rutile structures (reprinted from Ref. [101]).	22
2.10	Crystal structure of H-Nb ₂ O ₅ (reprinted from Ref. [101]).	22

2.11	Different current-controlled NDR modes observed in NbO _x -based MOM devices: (a) snapback NDR, and (b) combined S-type and snapback NDR. . . .	28
3.1	Three-dimensional schematic of the cross-point device structure with corresponding material layers. Inset shows an optical microscopy image of typical Au/Nb/NbO _x /Pt cross-point device with 20 μm × 20 μm active device area.	30
3.2	Optical micrograph of different steps of device fabrication: (a) image of a bottom electrode (BE) after the lift-off process for the Pt bottom electrode with a Ti adhesion layer, (b) image of four cross-point devices formed with a common bottom electrode after oxide and bottom electrode deposition, (c) the same devices after etching the oxide layer to expose the BE and, (d) after the final step (here wafer is coated with photoresist everywhere except the contact pads (BE and TE)).	31
3.3	(a) Thickness of the photoresist measured using a surface profilometer and, (b) the position of the line scan shown on the device structure (the yellow line corresponds to the red line in Fig. 3.3(a)).	31
3.4	Representative RBS spectrum obtained from a dc reactively sputtered NbO _x (x = 2.2) thin film deposited on a Si substrate at Ar/O ₂ (18.5/1.5) atmosphere.	33
3.5	Representative XPS spectrum obtained from a dc reactively sputtered NbO _x thin film deposited on a Si substrate at Ar/O ₂ (19/1) atmosphere: (a) Nb 3d core level spectrum, and (b) valence band spectrum for a sub-stoichiometric NbO _x (x ~ 1.98 ± 0.02) film.	34
3.6	Representative XRD spectrum obtained from a sub-stoichiometric NbO _x (x = 1.98 ± 0.02) thin film deposited on a Si substrate (a weak signal from (110) plane of Si substrate is observed).	35
3.7	Thermoreflectance measurement setup. (a) A simple representation of the thermoreflectance measurement system with an objective lens and 490 nm illumination wavelength, (b) duration of the hot and cold cycles, where hot refers to the time when a current was applied to the device and cold refers to the time when the device was not electrically activated, and (c) thermoreflectance response of the gold surface under different illumination wavelengths.	36

- 3.8 The two-zone (core-shell) parallel memristor model and switching characteristics. (a-b), Schematic of the core-shell representation of the current distribution, and an equivalent lumped-element circuit model of the core-shell structure, where R_m represents a memristive element that reflects the temperature-dependent conductivity of the core region and R_s is the parallel shell resistor. (c-f): Simulated current-voltage characteristics of devices under current-controlled operation showing (c), maximum negative differential resistance (d) continuous S-type NDR where the shell resistance is constant and greater than the negative differential resistance of the core, (e) discontinuous snapback NDR where the shell resistance is constant and lower than the negative differential resistance of the core, and (f) composite NDR when the shell resistance changes with current and is treated as a second memristor (inset). 38
- 4.1 (a) A schematic of the device structure, (b) a typical current-voltage (I-V) characteristic of the electroforming process for a $20\ \mu\text{m} \times 20\ \mu\text{m}$ Pt/Cr/ NbO_x /Pt device under voltage-controlled testing. Inset is a semi-log plot of the I-V characteristic. (c-d) Optical microscope images of the same device before (c) and after (d) the electroforming process. The dark spot on the device after forming indicates the location of a conducting filament. 42
- 4.2 (a) Temperature distribution in the active volume of the device for a current of 2.0 mA. The depicted structure represents a cross section of an axisymmetric model with the axis of rotation shown, (b) maximum temperature in Nb_2O_5 filament compared to the maximum temperature at top-electrode/PMMA interface, (c) maximum temperature at the top-electrode/photoresist interface as a function of device current and top electrode (Pt) thickness, and (d) maximum temperature at the top-electrode/photoresist interface as a function of top electrode (Pt) thickness. 44
- 4.3 (a-b) Location of the filaments of $20\ \mu\text{m} \times 20\ \mu\text{m}$ and $5\ \mu\text{m} \times 5\ \mu\text{m}$ cross-point devices respectively (each red dot represents a filament in a single device and each map collates data for 50 different devices). The overlaid lines show the position of the electrode edges in the cross-point structure. (c) Percentage of devices formed at the edge of the cross-point as a function of device area. (d) Variation of forming voltage as a function of device area (The error bars in **Fig. 4.3 (c-d)** represent standard deviation from the mean value of the data taken from more than 20 devices in each case. The dashed line in **Fig. 4.3(d)** shows a conventional fit to the experimental data). 46

4.4	Cross-sectional TEM of a cross-point device at (a) the bottom edge, and (b) top edge.	47
4.5	Resistivity of the NbO_x film as a function of stoichiometry (x). These data were extracted from the resistance of the as-fabricated devices measured at a low bias voltage.	48
4.6	Electroforming and filament distributions in $5\text{ }\mu\text{m} \times 5\text{ }\mu\text{m}$, Pt/Nb/ NbO_x /Pt cross-point devices: (a) Electroforming characteristic of a NbO_x ($x = 2.6$) device, (b) electroforming characteristic of a NbO_x ($x = 1.92$) device, (c) filament distribution in low-conductivity, NbO_x ($x = 2.6$) devices, (d) filament distribution in high-conductivity, NbO_x ($x = 1.92$) devices, (e) schematic of oxygen vacancy filament formed by field-induced generation, drift and diffusion of oxygen vacancies, and (f) schematic of a transient current filament due to current bifurcation. Note that each point in (c-d) represents a single device and the filament distributions represent 75 separate measurements for each film.	49
4.7	In-situ thermorefectance measurements: (a) in-situ (points) and ex-situ (line) current-voltage characteristics of a $10\text{ }\mu\text{m} \times 10\text{ }\mu\text{m}$ cross-point device with a high-conductivity NbO_x ($x = 1.99$) film, and the temperature of the film in the filamentary (red) and surrounding regions (blue), (b) 2D temperature maps of the top electrode surface for different device currents, and (c) temperature profile through the filamentary region for different device currents. Inset of Fig. 4.7 (c) shows a back-scattered electron image of the filamentary region in the oxide film after removing the top electrode.	51
4.8	Schematic of the axisymmetric device structure employed for finite element simulations including boundary conditions.	52
4.9	Finite element simulation: (a) current-voltage characteristics during bidirectional current sweep, (b) maximum temperature in oxide film as a function of device current, (c) current density distribution before and after bifurcation, (d) temperature distribution before and after bifurcation, and (e-f) 3D temperature distribution: (e) before (point A) and (f) after current bifurcation (point B).	53
5.1	Cross-sectional transmission electron micrographs of the device structures: (a) Pt/Nb/ NbO_x /Pt, and (b) Pt/Cr/ NbO_x /Pt. Corresponding EDX maps are shown on the right of each image and were obtained from the line scan through the thickness of the device.	56

5.2	(a) A typical electroforming step under current-controlled testing, (b) negative differential resistance (NDR) characteristic observed under current-controlled mode (black solid line) and volatile threshold switching (red dashed line) under voltage-controlled operation in a typical device with Nb top electrode, and (c) threshold- and hold-voltages as a function of electrode material extracted from the corresponding NDR response (data were taken for 8 devices for each electrode metal).	57
5.3	Voltage-controlled threshold switching in typical devices with Nb, Ti and Cr top electrodes respectively (from top to bottom) (20 consecutive switching cycles are shown for each case). Note that Nb and Ti top electrode devices exhibited symmetric threshold switching, while the Cr-top electrode devices exhibited asymmetric threshold switching.	58
5.4	Temperature dependent change of resistance calculated at -0.5 V for electroformed devices with Nb, Ti and Cr top electrodes.	59
5.5	1S1M behaviour observed under voltage-controlled mode in typical devices with (a) Pt/Ta/NbO _x /Pt and (b) Pt/Hf/NbO _x /Pt structures respectively (20 consecutive switching cycles are shown for each case).	59
5.6	Schematic of the switching elements in a Pt/Hf/Nb ₂ O ₅ /Pt device after electroforming (left) and a corresponding circuit representation (right). The value of R_1 varies under positive and negative bias conditions due to field driven oxygen transport at the top electrode/oxide interface resulting in the rupture or reconstruction of the memory filament.	61
5.7	Effect of series resistance on the (a) threshold switching hysteresis and, (b) negative differential resistance window.	63
5.8	Unipolar/non-polar switching in a representative 5 μm \times 5 μm cross point device with Pt/Nb ₂ O ₅ /Pt structure : (a) SET-RESET observed under negative bias, (b) SET-RESET observed under positive bias, and (c) SET-RESET observed under opposite bias polarity (negative polarity SET and positive polarity RESET).	63
6.1	(a) Cross-sectional transmission electron micrograph of a Ti:Nb ₂ O ₅ device with a Ti/Nb fraction of 0.72, (b-d): 2D elemental maps for Ti, Nb, and O respectively and, (e) corresponding EDX line-scan.	67
6.2	(a) Representative RBS spectra from Ti:Nb ₂ O ₅ film (rf power \sim 120 W) deposited on a Si substrate; clear Ti, Nb and O peaks are observed, and (b) Ti/Nb ratio as a function of rf power of the Ti target.	67

6.3	X-ray photoelectron spectra: (a) Nb-3d core level spectrum from Nb ₂ O ₅ , (b) Nb-3d and Ti-2p _{3/2} (inset) spectra from Ti:Nb ₂ O ₅ (Ti/Nb \sim 0.31), (c) Ti-2p _{3/2} core level spectrum from TiO ₂ , and (d) valence band spectra for the Nb ₂ O ₅ , Ti:Nb ₂ O ₅ and TiO ₂ films. The symbols in Fig. 6.3(a-c) represent experimental data and the solid lines show conventional fits to the data.	68
6.4	(a) Preformed resistances of 20 μ m \times 20 μ m cross point MOM devices (data were averaged for 20 devices in each case, error bars represent standard deviation from the mean value), and (b) a representative electroforming step of a Ti:Nb ₂ O ₅ device; inset shows representative low-field (measured at 0.1V) device resistances after electroforming.	69
6.5	(a) Current-controlled I-V characteristics of 20 μ m \times 20 μ m cross-point devices with Nb ₂ O ₅ , Ti:Nb ₂ O ₅ and TiO ₂ thin films, (b) voltage-controlled threshold switching of 20 μ m \times 20 μ m cross-point devices with Nb ₂ O ₅ and Ti:Nb ₂ O ₅ thin films (50 consecutive switching cycles are shown for each case).	70
6.6	(a): Device-to-device variability of threshold and hold voltages for different devices with Nb ₂ O ₅ and Ti:Nb ₂ O ₅ (Ti/Nb \sim 0.1) thin films (data were extracted from stable NDR response obtained using current sweeps from 0 to 2.5 mA and compared for 12 devices in each case), and (b-c): cycle-to-cycle variability of threshold and hold voltages for representative Nb ₂ O ₅ and Ti:Nb ₂ O ₅ (Ti/Nb \sim 0.1) devices, respectively (data were obtained from 6000 consecutive threshold switching cycles (quasi-static I-V) for both cases).	71
6.7	Representative temperature dependent resistance values for different devices obtained at 500mV (the data for the extracted E _{ac} were averaged for minimum three devices in each case)	72
6.8	Simulated device characteristics: (a) effect of film conductivity represented by resistance pre-factor R ₀ , and (b) effect of activation energy on current-controlled NDR response.	73
6.9	Lumped element modelling: (a-b) effect of resistance pre-factor (R ₀) on the threshold voltage hysteresis and R _{NDR} , respectively, and (c-d) role of activation energy E _{ac} on the same.	74

7.1	Electroforming and NDR characteristics as a function of stoichiometry. (a) Electroforming, and (b) subsequent S-type NDR characteristics of a $10\text{ }\mu\text{m} \times 10\text{ }\mu\text{m}$ cross-point device of 25 nm Pt/5nm Nb/NbO _{2.6} /25 nm Pt structure. (c) Electroforming at 15 mA, and (d) subsequent snapback NDR characteristics of a $10\text{ }\mu\text{m} \times 10\text{ }\mu\text{m}$ cross-point device of 25 nm Pt/5nm Nb/44 nm NbO _{1.92} /40 nm Pt structure. (e) Electroforming at 12 mA, and (f) subsequent switching snapback characteristics a $10\text{ }\mu\text{m} \times 10\text{ }\mu\text{m}$ cross-point device with 25 nm Pt/5nm Nb/44 nm NbO _{1.92} /40 nm Pt structure indicating switching due to current bifurcation. Note that switching characteristics of all samples were measured with negative bias applied to the top electrode unless otherwise stated.	78
7.2	In-situ temperature measurements of S-type and snapback NDR. (a) Current-voltage characteristics and average temperature rise of the filament and surrounding area (the area used for averaging is indicated by boxes in (b)) as a function of applied current. (b) 2D maps of the surface temperature rise in a $5\text{ }\mu\text{m}$ device operating at 1 mA and 6 mA. (c) Current localisation of S-type NDR in the post-formed device at different current levels as shown in (a). (d) The average temperature rise of the permanent filament and surrounding area (indicated by boxes in (e)) as a function of applied current, and (e) 2D map of the surface temperature in a $10\text{ }\mu\text{m}$ device at pre-threshold (4mA) and post-threshold (10 mA) regions. (f) Current localisation in post-formed device at different current levels as shown in (d) (the blue arrow indicates snapback transition). (g) The average temperature rise of the current filament and surrounding area (indicated by boxes in (h)) as a function of applied current, and (e) 2D map of the surface temperature in a $10\text{ }\mu\text{m}$ device at pre-threshold (4 mA) and post-threshold (12 mA) regions. (i) Current localisation due to current bifurcation in the device without permanent filament as shown in (g) (the blue arrow indicates snapback transition). The device structure used in thermoreflectance measurements is 25 nm Au/5 nm Nb/35 nm NbO _{2.05} /40 nm Pt. The circles overlaying the I-V curves represent in-situ I-V measurements during thermoreflectance measurements.	80
7.3	Area dependent switching properties of NbO _x with $x = 1.92$. (a) NDR characteristics as function of area showing area dependent S-type NDR and snapback (SB)-type NDR, and (b) threshold voltage and current as a function of area.	81
7.4	Matrix representation (schematic) of dependency of S-type and snapback NDR (red lines) as a function of stoichiometry and area.	82

7.5	Thickness dependence of switching properties of NbO_x with $x = 2.05$. (a) Thickness dependent current-voltage characteristics of $10\text{ }\mu\text{m} \times 10\text{ }\mu\text{m}$ devices showing S-type NDR and snapback (SB-NDR). (b) Threshold voltage and current as a function of thickness with switching mode depicted by shading. Data points represent averages for ten devices of each thickness	83
7.6	Matrix representation (schematic) of dependency of S-type and snapback NDR (red lines) as a function of thickness.	83
7.7	Effect of substrate temperature on NDR behaviour. (a) Examples of NDR responses at two distinct substrate temperatures, and (b) extracted threshold -voltages and -currents as a function of substrate temperature. The shaded region in (b) identify devices that exhibit S-type (S-NDR-grey) and snapback (SB-NDR-red) responses.	84
8.1	Polarity dependent electroforming and NDR characteristics of Pt/Nb/ $\text{NbO}_{1.92}$ /Pt devices: (a) electroforming of a $5\text{ }\mu\text{m} \times 5\text{ }\mu\text{m}$ cross-point device under positive bias, (b) electroforming of a different $5\text{ }\mu\text{m} \times 5\text{ }\mu\text{m}$ cross-point device under negative bias; and (c) typical polarity-dependent switching characteristics of electroformed devices showing a transition from S-type to snapback NDR irrespective of electroforming polarity.	88
8.2	(a-b), In-situ I-V characteristics of a $10\text{ }\mu\text{m} \times 10\text{ }\mu\text{m}$ $\text{NbO}_{1.99}$ device showing (a) S-type NDR under positive bias, and (b) snapback under negative bias. Insets show the in-situ thermorefectance maps of the device during I-V testing, (c) Temperature profile through the filamentary region for different current-voltage values during positive bias. (d) Temperature profile of the same device for different current-voltage values during negative bias. The dashed curves in (c) and (d) represent the experimental data and the smooth lines show Gaussian fits of the data. A, B, and C denote subthreshold, threshold, and post-threshold points respectively in the I -V characteristic obtained under positive bias, while D, E, and F denote the same for negative bias polarity. . .	89

8.3	(a) Temperature dependent I-V characteristics of a typical sub-stoichiometric NbO_x device ($x = 2.22$), equivalent circuit element is shown inset, (b-c) signature plots confirming thermionic emission as the major mechanism for Nb top and Pt bottom electrodes ($x = 2.22$), (d) extraction of zero bias potential barrier at top and bottom interfaces for a typical sub-stoichiometric NbO_x ($x = 2.22$) device, (e) asymmetry plot of the data presented in Fig. 8.3(a), current asymmetry η_{asym} is defined as the ratio of device current under negative bias to that under positive bias ($I_{\text{negative}}/I_{\text{positive}}$), and (f) current asymmetry before and after electroforming for devices with different oxide stoichiometry. The dashed lines in Fig.8.3 (f) represent the experimental data after electroforming and the smooth lines are the experimental data of the corresponding devices before electroforming.	91
8.4	(a-c), Polarity dependent NDRs observed in Nb/ $\text{NbO}_{x \sim 1.99}$ /Pt MOM cross-point devices with $5 \mu\text{m} \times 5 \mu\text{m}$, $10 \mu\text{m} \times 10 \mu\text{m}$ and $20 \mu\text{m} \times 20 \mu\text{m}$ active area, and (d) matrix representation of dependency of S-type and snapback NDR as a function film stoichiometry, device area and bias polarity. The notations S/S and SB/SB are used for S-type NDR and snapback NDR respectively under subsequent opposite polarity biasing conditions, while S/S-B is used to indicate S-type NDR under positive bias and snapback NDR under negative bias.	92
8.5	(a-b): Asymmetric and symmetric threshold switching depending on oxide stoichiometry.	94
8.6	(a) Schematic of the core-shell model of memristor, (b) circuit model showing a threshold switch (TS) as the core element, a variable resistor indicating the interface resistances at the metal-oxide interfaces and R_{film} represents the oxide resistance in the shell area, which is modelled by the Poole-Frenkel equation, (c) effect of shell resistance on the NDR response, (d) effect of interface resistance (as a function of increasing barrier heights) on the NDR response when the shell resistance (R_{film}) is fixed for a given device area, thickness and oxide stoichiometry. Note that for opposite polarity biasing one interface becomes forward-biased and the other becomes reverse-biased and vice versa, as a result the interface resistance experiences significant change when the polarity is reversed.	96
A.1	(a-b): The undercut effect in Pt/ HfO_2 /Pt/Ti/ SiO_2 /Si structure is clearly observed in the left and right edges of bottom electrode.	105

A.2	Histogram of forming voltage of (a) low-conductivity- stoichiometric NbO_x ($x = 2.6$) and (b) high-conductivity- sub-stoichiometric NbO_x ($x = 1.92$) films.	105
A.3	Effect of polarity reversal on the current-controlled switching in typical devices with (a) Nb, (b) Ti, (c) Cr, (d) Ta and (e) Hf top electrodes respectively.	106
A.4	Device-to-device variability: Variation of threshold and hold voltages for devices with undoped and Ti-doped Nb_2O_5 films (V_{TH} and V_{H} were extracted from current-controlled NDR for 12 devices in each case). The error bars represent standard deviation from the mean value	108
A.5	(a-b) Cycle-to-cycle variability: (a-b) voltage-controlled threshold switching of $20\text{ }\mu\text{m} \times 20\text{ }\mu\text{m}$ cross-point devices with Nb_2O_5 and $\text{Ti:Nb}_2\text{O}_5$ ($\text{Ti/Nb} \sim 0.1$) thin films respectively (6000 consecutive switching cycles are shown for each case). (c) Variation of threshold and hold voltages for two identical devices with Nb_2O_5 and $\text{Ti:Nb}_2\text{O}_5$ films respectively (V_{TH} and V_{H} were extracted from ~ 6000 consecutive threshold switching cycles in each case), and (d) histograms showing the data plotted in (c).	109
A.6	Bipolar memory switching observed in a $\text{Ti/TiO}_2/\text{Pt}$ device.	110
A.7	(a) Schematic of the circuit used to measure dynamical characteristics, (b) switching cycles under triangular voltage pulse for devices with Nb_2O_5 and $\text{Ti:Nb}_2\text{O}_5$ films respectively, (d-f) switching time characteristics of a representative device with Nb_2O_5 , and (g-i) switching time characteristics of a representative device with $\text{Ti:Nb}_2\text{O}_5$ ($\text{Ti/Nb} = 0.1$). The ‘delay time’ (τ_{delay}) was defined as the time to reach 50% value of the low-to-high switching current across the device (indicated by point B in (d)); The ‘switch on’ time (τ_{on}) was defined as the time interval between the 10% and 90% value of the low-to-high switching current across the device (indicated by the time between points A and C in (d)); The ‘switch off’ time (τ_{off}) was defined as the time interval between 10% and 90% value of the high-to-low switching current across the device (indicated by the time between points D and E in (e)).	111

A.8	(a) Schematic of the circuit used to measure oscillation dynamics, (b) measured threshold switching and current controlled NDR under quasi-static current-voltage measurements for a device with Nb_2O_5 film (b) measured oscillation waveform of the device current in the $50\ \Omega$ resistor when a voltage pulse $\sim 4\ \text{V}$ was applied for $3\ \mu\text{s}$, (c) extracted oscillation frequency and energy/spike for the device with undoped Nb_2O_5 film, (d) measured threshold switching and current controlled NDR under quasi-static current-voltage measurements for a device with $\text{Ti:Nb}_2\text{O}_5$ film ($\text{Ti/Nb} \sim 0.1$), (e) measured oscillation waveform of the device current in the $50\ \Omega$ resistor when a voltage pulse $\sim 4\ \text{V}$ was applied for $3\ \mu\text{s}$, and (f) extracted oscillation frequency and energy/spike for the device with $\text{Ti:Nb}_2\text{O}_5$ film ($\text{Ti/Nb} \sim 0.1$).	112
A.9	Electroforming current (I_F) as a function of (a) cross-point device area and (b) oxide thickness for devices with sub-stoichiometric NbO_x films.	113

List of Tables

2.1	Material properties of Niobium and Niobium Oxides	20
3.1	Sputter deposition conditions of NbO _x films	32
4.1	Properties of NbO _x layer used in the simulation.	52
5.1	Summary of the MOM stacks with different top electrodes, their thermodynamic stability and switching characteristics. Thermochemical data for different oxides were extracted from Ref. [252].	60
5.2	Memristor parameters used in the simulation for the Poole-Frenkel model. .	62
6.1	Deposition parameters for Nb ₂ O ₅ , Ti-doped Nb ₂ O ₅ (Ti:Nb ₂ O ₅) and TiO ₂ films.	66
6.2	Memristor parameters used in the simulation for the Poole-Frenkel model. .	73
8.1	Memristor parameters used in the simulation for core memristor and shell resistance	95
A.1	Memristor parameters used in the simulation for core memristor and shell resistance where both are represented by similar threshold switches with slightly different parameters.	104
A.2	Thermochemical data extracted from Ref. [252].	106

Introduction

1.1 Motivation

1.1.1 From von Neumann to neuromorphic computing

Scientific advancements and technological breakthroughs address considerable personal and societal need and have brought many life-saving solutions over hundreds of years. Among countless man-made innovations, power-generators and computers have brought significant advancements that are accelerating the development of current human civilisation. Modern digital computers are highly advanced and have become an indispensable part of everyday life. Today, computers are used to control devices and machines that perform a broad range of specific tasks spanning from entertainment to communication, from medical treatments to office works, etc. This is possible due to their ability to perform sophisticated tasks and solve structured problems. Most digital computers are designed in such a way that they can perform Boolean mathematics under the von Neumann approach [1] in which the central processing unit (CPU) and the memory unit are physically separated. In this configuration these two units are connected through a communication channel referred to as a parallel data bus as shown in **Fig. 1.1(a)**. The data is retrieved from the memory unit upon specified instructions and the computation takes place in the CPU, while the data is continuously transferred back and forth between the two units.

Despite their excellent performance in general purpose computing, conventional computers have limitations in terms of power efficiency and in solving complex and unstructured problems, including voice and image recognition [4]. This is primarily due to the considerable power consumption required for the transfer of a large amount of data between the CPU and the memory unit. The parallel data bus (i.e., the connecting channel) then be-

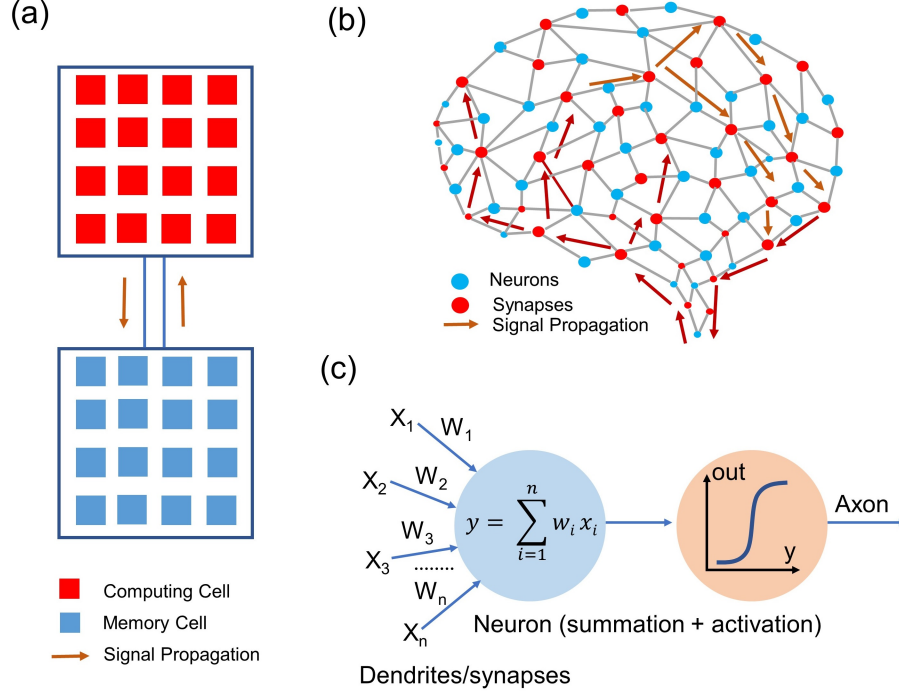


Figure 1.1: (a-b) Schematic representation showing comparison between von Neumann computing architecture, and the brain computing system respectively, and (c) artificial neuron architecture (reproduced from Ref. [2, 3]).

comes a bottleneck for an energy-efficient data transfer, which is often referred to as ‘von Neumann bottleneck’. In order to enhance the energy efficiency of digital computers two general approaches are commonly followed: the scaling down of the size of the transistor (enabling increased switch density) and elevating the data transfer rate between the CPU and the memory unit [5]. However, transistors are currently reaching their scaling limits and achieving maximum data transfer rates [5, 6]. In this circumstance, exploring an alternative computing paradigm that is efficient, scalable and power saving is of great importance. Moreover, with the emergence of artificial intelligence (AI), robotics, big data, and the internet of things (IoT), there is a growing demand for major breakthroughs to address the associative challenges of these emerging technologies, including classifying objects, capable and adaptive learnings and proactive decision making, etc. [7, 8].

A biological brain is one of the most robust and amazing information processors that can easily tackle a complex problem and make judgments based on surrounding conditions. Several issues, such as the brain’s sensing capabilities, problem-solving skills and its low power consumption make it an ideal model [9]. Indeed, current von-Neumann computers are outperformed by the human brain in a plethora of applications, including voice and pattern recognition, understanding and learning from data and finally, classifying and resolving

problems. The effectiveness of the human brain stems from its fundamental difference to the von Neumann architecture where distributed parallel processing is enabled by interconnected neural elements (e.g., neurons and synapses) as shown in **Fig. 1.1(b)**. The synapses modify the strength of the signals propagating between neurons to enable learning and memory, while the neurons integrate the synaptic inputs into a decision to fire a single or multiple electrical spike [10, 11].

The superior functionalities of human brain and an improved understanding of its morphology during the late 1980s has led to the development of a new computational paradigm referred to as ‘neuromorphic computing’. It embraces both hardware- and software-based approaches that receive inspiration from mimicking neural functionalities and is able to achieve features such as reduced power consumption, adaptive learning, classifying objects, and processing probabilistic fault-tolerant information [12–14]. In brief, the promise of data processing speed, computing capacity and attractive power efficiency has made neuromorphic computing as a potential alternative of traditional computing architecture and an active area of substantial research and development.

1.1.2 Emerging areas in hardware-based neuromorphic computing

A true neuromorphic computing architecture takes inspiration from the computational capabilities of human brain and needs basic circuit elements that correspond to both synapses and neurons as in the case of a biological brain. Importantly, both of these circuit elements need to address some important criteria, including scalability, power efficiency and ability to implement relevant learning rules that can facilitate large-scale neural functionalities [15]. It is anticipated that building neuromorphic hardware can achieve better energy efficiency and will reduce considerable space required to enable parallel distributed computing.

Neuromorphic computing devices can be realised by using Si-MOSFETs [16], but the requirement of tens of transistors to build a single neuron limits energy efficiency and their utility for a large scale computing system [17]. Recently, a number of technologies have been explored to enable hardware implementation of artificial neurons and synapses, including complementary metal-oxide-semiconductor (CMOS) analogue circuits, digital logic circuits, ferroelectric transistors, phase change memory, and different types of memristors [4, 15, 18–21]. Among them, memristor-based approaches have obtained increasing attention due to their CMOS compatibility, low power consumption, small form-factor, analogue behaviour and rich dynamical characteristics [22–25].

1.1.3 Memristor-based neuromorphic computing

The term ‘Memristor’ is derived from the words ‘Memory’ and ‘Resistor’ predicted by Leon Chua in 1971 from symmetry arguments, and was defined as the fourth fundamental circuit element after resistor, capacitor and inductor [26, 27]. Chua identified mathematical relationships that connect the four fundamental circuit variables, namely electric current i , voltage v , charge q and magnetic flux ϕ , as shown in **Fig. 1.2**.

Here, the term ‘memristance (M)’ is defined as the property that connects the electric charge q and magnetic flux ϕ by the relation, $d\phi = M dq$. A key feature of memristance is the fact that it depends on the past current through dependence on magnetic flux ϕ which is generalised from the circuit characteristic of an inductor and regarded as the time integral of voltage (see **Fig. 1.2**) [28]. According to Chua, any circuit element can be classified as a memristor if it shows a pinched hysteresis loop (a Lissajous figure) when a bi-directional periodic voltage or current is applied, and the hysteresis loop passes through the origin in the corresponding current-voltage plot [29, 30].

Memristive-like phenomena have been observed since a couple of decades ago [31–33], but were not referred to the Chua’s concept of ‘memristor’ until 2008, when a research group from Hewlett-Packard reported a two-terminal electrical device using TiO_2 that behaved like a memristor [34]. Since then, many systems and devices have been categorised as memristive, including spin-torque transfer random access memory (RAM) devices, resistive switching devices (often referred to as RRAM or ReRAM), phase-change memories, atomic switches and other devices and systems based on diverse materials and working principles [28, 35–37]. It is important to note, however, that the interpretation of such behaviour as ‘memristive’ remains controversial [38–43]. Nevertheless, the term is adopted throughout this thesis for

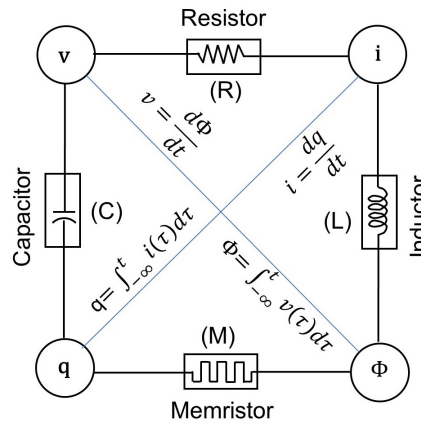


Figure 1.2: Schematic representation of the four fundamental circuit elements, namely: resistor, capacitor, inductor and memristor [27].

consistency with most recent reports [3, 39, 42, 44–46].

In the recent years, ‘memristive’ devices have established themselves as important technological elements for a wide range of applications, including Boolean logic circuits, image processors, sensors, and neuromorphic hardware etc. [15, 42]. Studies have shown that important functions of biological synapses can be emulated using two-terminal memristors that have the ability to achieve multiple, reversible resistance states with the application of an appropriate electrical stress (e.g. current or voltage stimuli) [47]. An emulator of neuronal functions (termed as ‘neuristor’) was proposed by Pickett et al. [44] which was based on a Mott-memristor (categorised in the class of ‘extended memristor’ [45]) driven by threshold switching response in NbO_x . Indeed, a threshold switching device can exhibit self-sustained oscillation when configured in a Pearson-Anson circuit [48], and a combination of two or more such relaxation oscillators facilitate the imitation of neuronal functionalities, including threshold spiking and voltage dependent frequency modulation when coupled capacitively or resistively [13, 46]. For example, VO_2 -based coupled threshold switches combined with passive circuit elements have been shown to mimic the rich behaviours of biological neurons [46]. Interestingly, a recent study has also demonstrated that multiple neuronal functionalities can be achieved in a single-memristor-based oscillator that is powered by complex threshold switching or current-controlled negative differential resistance modes in NbO_x [49]. Recently, the utilisation of a memristor-based approach has been extended to other emerging areas such as non-volatile memory technology and neuro-robotics, where these devices are used to build high-density memory arrays and artificial sensory systems (e.g., nociceptors, afferent nerves, somatosensors, optic sensory units etc.) respectively [50–54].

Therefore, with these diverse range of applications, realising memristors and memristive systems, understanding their physical mechanism and engineering different functionality becomes significantly important.

1.2 Overview of this thesis

Oxide-based memristors and memristive systems are highly desirable, since they offer many advantages over other competing technologies in terms of cost effectiveness, speed and thermal stability [55, 56]. However, to meet the growing needs of emerging technologies, selecting an appropriate material, and engineering the device aspects are at the heart of their future developments and integration with the current technology [23, 55, 56]. To this end, two terminal MOM devices based on niobium oxide (NbO_x) thin films are particularly interesting, as they exhibit a wide range of reliable memristive switching phenomena, including threshold switching or current-controlled negative differential resistance (NDR) which has important

applications in non-volatile memory and hardware-based neuromorphic computing [32, 57–60]. Specifically, the threshold switching response of NbO_x can be used to build selector elements that eliminate the sneak current path problem in cross-bar memory arrays [61], and the spiking response of coupled NDR devices can be used to implement artificial neurons [13], as mentioned earlier. However, many critical issues and challenges still remain unresolved, including a proper understanding of their physical mechanism (including the origin of different switching modes), scaling, uniformity, robustness, and the dependence of the switching modes and parameters on material and device-specific properties.

This study aims to investigate the filamentary threshold switching and current-controlled negative differential resistance in niobium oxides and understand their physical origin as well as materials and device dependencies. This thesis is structured in 9 chapters.

The motivation and background justification are introduced in **Chapter 1** and **Chapter 2**. A brief overview of the memristive switching is presented in **Chapter 2**, and the discussion proceeds by covering fundamental concepts of non-volatile and volatile resistance changes and transport properties in two terminal MOM structures. With a particular focus on niobium oxides the material characteristics of the Nb-O family, and then memristive switching phenomena in niobium oxides are reviewed. This chapter also presents a brief review of recent progresses in understanding the electroforming process and subsequent switching characteristics of two-terminal MOM devices, including their material and device dependencies with a particular emphasis on niobium oxides.

Chapter 3 contains a brief overview of the experimental techniques employed in the studies described in the subsequent chapters. These include thin films deposition, device fabrication, thin films analysis and device characterisation techniques. A two-zone parallel memristor model is introduced to account for the diverse range of NDR modes observed in MOM structures.

In **Chapter 4** a simple means of detecting and spatially mapping volatile and non-volatile conductive filaments in MOM cross-point devices is introduced. This technique is further utilised to investigate the modes of electroforming in low- and high-conductivity NbO_x films, where it is used to map the spatial distribution of conductive filaments. Results from these analyses are further correlated with the current-voltage characteristics, in situ thermorefectance measurements, and finite element modelling.

Chapter 5 investigates the role of metal/oxide interface reactions in determining the threshold switching response of metal/ Nb_2O_5 /Pt devices. The experimental results are then correlated with thermodynamic data and lumped element modelling.

In **Chapter 6**, a comparison of the threshold switching and current-controlled negative differential resistance (NDR) characteristics of cross-point devices fabricated from undoped

Nb_2O_5 and Ti-doped Nb_2O_5 is presented. A systematic study is carried out to understand the role of doping in controlling the switching response. The observed dependencies are then explained using data from temperature dependent current-voltage characteristics and correlated with a lumped-element circuit model.

Understanding the physical origin of the discontinuous snapback NDR is the focus of **Chapter 7**. In this chapter, the observed post-forming device characteristics are correlated with in-situ thermorefectance imaging and predictions of a simple model to identify the physical origin of snapback NDR.

In **Chapter 8**, a polarity-dependent negative-differential-resistance (NDR) response is shown for Nb/ NbO_x /Pt cross-point devices. Role of the metal-oxide Schottky barriers in determining the polarity-dependent response is investigated. Results from temperature-dependent electrical measurements, in-situ thermorefectance imaging and lumped element modelling are used to reveal the origin of different NDR responses.

Finally, in **Chapter 9** the thesis is concluded with a summary of the experimental observations correlated with model predictions, significance of the research outcomes and outlining future research directions.

Background

2.1 Memristive switching in two terminal MOM structures

Two terminal metal/oxide/metal (MOM) structures exhibit a diverse range of memristive phenomena, including non-volatile resistance switching, volatile threshold switching and a combination of both. Upon application of an external electrical stress (e.g., voltage or current pulses) these devices can achieve distinct resistance states determined by the operating conditions. The resistance switching is often mediated by the formation and rupture of conductive filaments (CFs) that are composed of interstitial metal atoms, oxygen vacancies or both. Depending on the physical mechanism and morphology of the CF these devices can be classified into three dominant classes, namely electrochemical metallisation (ECM) cells, valence change memory (VCM) and thermochemical memory (TCM), respectively [62, 63]. While the CFs in the VCM and TCM devices are created by anions (e.g., oxygen vacancies), those in ECM cell is composed of cations (typically metal ions originated from one of the electrodes) and these devices are broadly termed as charged-based random access memory (CBRAM) [63, 64]. The primary difference between the VCM and TCM devices lies in the mechanism of rupture and reconstruction of the oxygen-vacancy-CF. Specifically, in the former case these processes can be controlled by reversing the voltage polarity, where in the latter case the CF is thermally ruptured by passing a high current through the device [63]. Several studies have shown that the CFs are much smaller than the overall device area and their dimensions are typically on the order of a few nanometres to a few tens of nanometres [55, 65]. Interestingly, non-filamentary processes can also be observed in two terminal MOM structures. For example, the resistance change can be mediated by the formation of a tunnel junction or modification of the Schottky barriers across the whole metal-oxide interface.

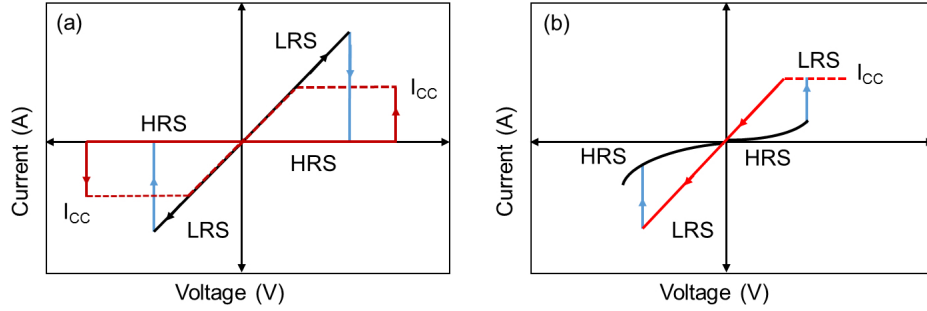


Figure 2.1: Schematics of the I-V curves for memory switching (a) unipolar switching, and (b) bipolar switching.

Moreover, instead of binary states, multiple resistance states can be achieved which is determined by the operating condition, device structure and governing physical processes [66]. The following section contains a brief description of the three common memristive switching phenomena observed in two terminal MOM structures, including non-volatile memory switching, volatile threshold switching and hybrid memory-threshold (1S1M) switching.

2.1.1 Non-volatile memory switching

The non-volatile change of electrical resistance in two terminal MOM devices is referred to as ‘memory’ switching and two basic types, namely unipolar and bipolar switching are generally observed depending on the device structure and operating condition. Among them, the unipolar switching is a thermally driven process in which the switching effect is independent of the polarity of the applied voltage but depends on its amplitude [67]. To observe a non-volatile memory switching, an initial electroforming (or simply called ‘forming’) process is needed which creates a soft conductive filament with a controlled resistance. After that, the device can be switched between a high resistance state (HRS) and a low resistance state (LRS) interchangeably upon application of appropriate electrical stresses. The transition from LRS to HRS is termed as a ‘RESET’ process and the subsequent transition from HRS to LRS is termed as a ‘SET’ process. Specifically, in unipolar switching the RESET and SET processes are mediated by the dissolution/rupture and re-construction of the conductive filament due to temperature-controlled diffusion of defects (e.g. oxygen vacancies) [67]. In contrast, the polarity of the applied bias determines the resistance state of bipolar switching [68]. In this case, the voltage polarity must be reversed to achieve the ‘SET’ (HRS \rightarrow LRS) and ‘RESET’ (LRS \rightarrow HRS) operations (**Fig. 2.1**) and these are mediated by an electric-field-controlled drift of oxygen vacancies. It is interesting to note that, a bipolar-like behaviour can be observed in a device that exhibits unipolar switching, because the RESET process in the

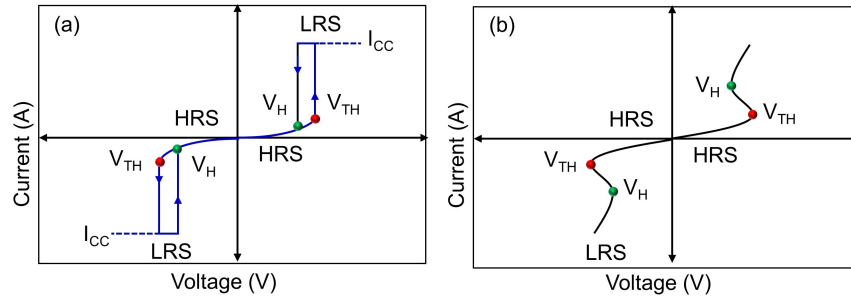


Figure 2.2: Schematics of the I-V curve for volatile threshold switching: (a) voltage-controlled mode, and (b) current-controlled mode.

latter case can be achieved by using a bias of either polarity [63].

2.1.2 Threshold switching or Current-controlled NDR

Volatile threshold switching is shown in **Fig. 2.2(a)** in which the MOM device exhibits a large non-linear change in electrical conductivity. In this case, the device initially remains in HRS and the resistivity of the device drops abruptly when the applied voltage exceeds a threshold value (V_{TH}). This leads to a transition from HRS to LRS and the device reverts back to its initial HRS as the voltage is reduced to a value called hold voltage (V_H). Since such type of device response is transient, i.e., the device comes back to its initial HRS (during the reverse sweep), this type of switching is termed as ‘volatile’ switching. Under current-controlled testing these devices typically exhibit a smooth transition from positive to negative differential resistance (NDR) as shown in **Fig. 2.2(b)** (hereafter referred to as S-type NDR) due to a rapid increase in device conductance.

Threshold switching or current-controlled NDR has been observed since 1960s [58] and often reported for chalcogenides [69, 70], and a broad range of transition metal oxides, including VO_x [71], NbO_x [72], TaO_x [73], TiO_x [74] etc. In general, this type of response can arise from diverse processes, including electronic, thermal or a combination of both [72, 75, 76]. Explicitly for amorphous transition metal oxides, the S-type NDR is well explained by a thermally induced conductivity change mediated by local Joule heating [77]. Significantly, this type of response can arise as the result of uniform conduction in the oxide film or filamentary conduction resulting from an electroforming process [78, 79]. For the latter case, threshold switching can co-exist with a non-volatile memory element [80, 81] and the switching occurs in a small volume between a residual conductive filament and the reactive electrode as inferred from area- and thickness-dependent current-voltage characteristics [82].

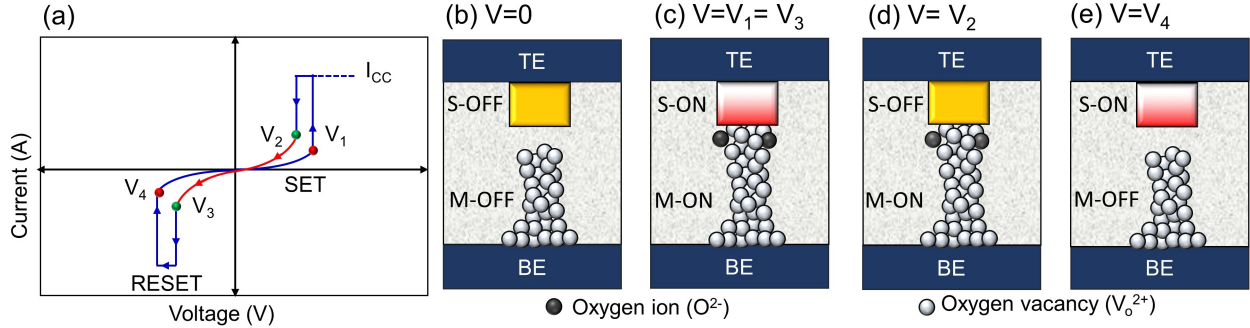


Figure 2.3: (a) Schematic of the I-V curve for hybrid threshold-memory (1S1M) switching behaviour, and (b-e) schematic diagrams of the operating mechanism of 1S1M switching at different bias voltages indicated in Fig. 2.3(a). TE and BE represent the top electrode and bottom electrode respectively in a two terminal MOM structure (reproduced from Ref. [61]).

2.1.3 Hybrid threshold-memory (1S1M) switching

The term 1S1M stands for ‘one selector one memory’ and refers to a hybrid type of switching that incorporates a threshold switching filament (termed as ‘selector, S’) serially connected with a memory filament (M). This type of switching arises from active contributions of both components [61]. **Fig. 2.3** shows a schematic of a typical 1S1M switching response with a positive polarity SET and a negative polarity RESET.

During the positive cycle, the device is initially in HRS and as the voltage reaches to the threshold value V_1 , the threshold element switches from insulating to a conducting state (Selector (S) ON). This also causes the memory filament to switch from HRS to LRS (memory (M) ON). When the applied voltage is reduced, the threshold element reverts back to an insulating state at the hold point V_2 (S-OFF), while leaving the memory filament still in ON state (shown by the red line). During the subsequent negative cycle, the device initially shows an intermediate resistance state (red line) with the memory filament in ON and the threshold (selector) element in OFF states. With a further increase of voltage, the threshold element transitions to a LRS (S-ON) as soon as the voltage arrives at the threshold point V_3 . When the voltage is further increased the memory filament resets at V_4 (M-OFF) and consequently the device reverts back to its initial HRS once again [83]. Note that, the SET or RESET processes can be observed using either bias polarity depending on the device structure and operating condition.

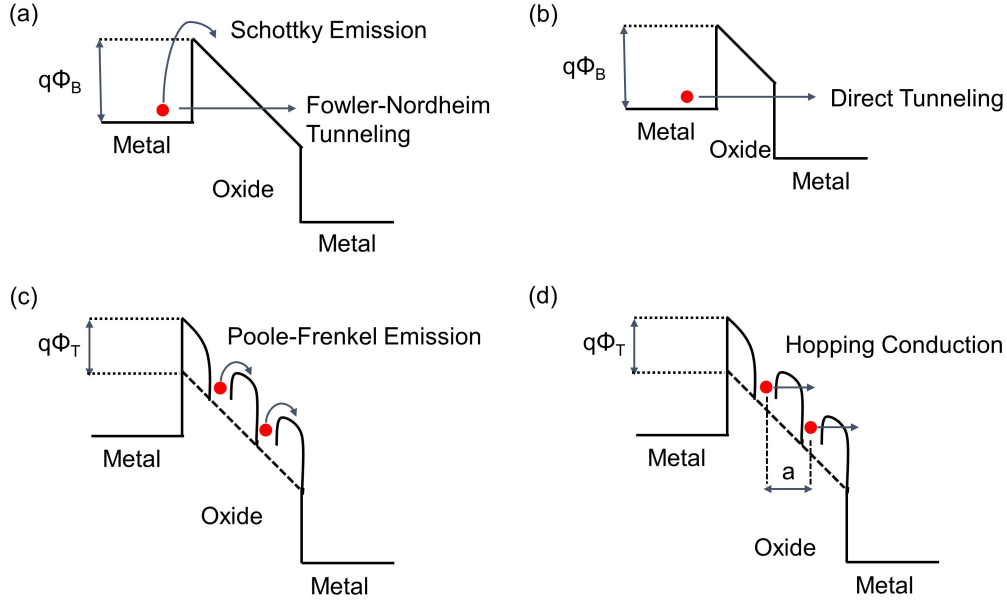


Figure 2.4: Schematics of the energy band diagram for interface-controlled and bulk-limited conduction in MOM structures: (a) Schottky emission and Fowler-Nordheim tunnelling, (b) direct tunnelling, (c) Poole-Frenkel emission, and (d) hopping conduction.

2.2 Current transport properties in dielectric oxide films

The current-voltage characteristics in MOM devices are governed by interface-controlled and bulk-limited conduction mechanisms. A brief description of the dominant mechanisms is outlined below.

2.2.1 Interface-controlled conduction

When a metal electrode is placed in a direct contact with an oxide layer, a potential barrier is formed at the metal/oxide interface due to the difference of their work functions which subsequently governs their electron transport properties. The magnitude of this interface barrier (often termed as Schottky barrier) is determined from the difference between the work function of the metal and the electron affinity of the oxide layer [84]. Depending on different factors (e.g., oxide thickness) a diverse range of interface-controlled conduction can be observed, including Schottky emission, Fowler-Nordheim tunnelling and direct tunnelling.

Schottky Emission

Schottky emission is a thermally-activated conduction process in which the current-voltage characteristic is governed by thermionic emission over the potential barrier formed at the

metal/oxide interface and has the form [85]

$$I = AA^*T^2 \cdot \exp\left(-\left(\phi_{B0} - \alpha\sqrt{V}\right)/k_B T\right) \quad (2.1)$$

Where k_B is the Boltzmann constant, T is the absolute temperature, ϕ_{B0} is the zero bias potential barrier height at the metal/oxide interface, α is the barrier lowering factor, A is the device area, A^* is the Richardson constant ($A^* = \frac{4\pi q m^* (k_B)^2}{h^3}$) and m^* is the effective mass of electron.

From the above equation it is evident that the current density in this case is a function of electric field and temperature, and the data for a given electric field (V) should exhibit a linear trend on a $\ln(I/T^2)$ vs $1000/T$ plot [$I = J \times A$; A is the total device area]. The slope of this curve yields an activation energy corresponding to the effective potential barrier (corresponding to V),

$$E = \phi_{\text{eff}} = \phi_{B0} - \alpha\sqrt{V} \quad (2.2)$$

Thus, in this case the obtained activation energy or the effective barrier height decreases with increasing applied bias V .

Fowler-Nordheim Tunnelling

Fowler-Nordheim tunnelling is observed in MOM devices with a thin oxide layer and in this case electrons are conducted from metal electrode to the oxide layer through a quantum mechanical ‘tunnel effect’ [86]. Specifically, when a large electric field (E) is applied the effective potential barrier narrows, and the electrons tunnel through a triangular potential barrier into the conduction band as shown in **Fig. 2.4 (a)**. This type of conduction is expressed as [87]:

$$J_{\text{FN}} = \frac{q^3 E^2}{8\pi h q \phi_B} \cdot \exp\left(-\frac{8\pi\sqrt{2qm_T^*}}{3hE} \cdot \phi_B^{3/2}\right) \quad (2.3)$$

Where, m_T^* is the tunneling effective mass in oxide (dielectric); the other notations have their usual meanings.

The tunnelling current can be effectively extracted from current-voltage characteristics that are obtained at extremely low temperatures where it is dominant over the currents from thermionic emission. In this case, the data for a given electric field (E) exhibits a linear trend on a $\ln(J/E^2)$ vs $1/E$ plot.

Direct Tunnelling

Direct tunnelling is often observed when an ultra-thin oxide layer is used in the MOM structure [87, 88] and the process is shown schematically in **Fig. 2.4 (b)**. The direct tunnelling current can be approximated as [87],

$$J_{DT} = \frac{q^3 E^2}{8\pi h q \phi_B} \cdot \exp \left(-\frac{8\pi \sqrt{2q m_T^* \phi_B}}{3h} k \cdot t_{ox,eq} \right) \quad (2.4)$$

Where, k and $t_{ox,eq}$ represent dielectric constant of the oxide material and equivalent oxide thickness respectively.

2.2.2 Bulk-limited conduction

Bulk-limited conduction in MOM structures is governed by the switching material, i.e., the oxide itself. This type of conduction is mediated by the transport of either electrons moving from one defect site to another, or ions travelling between defect sites. Some of the common bulk-limited conduction are Poole-Frenkel conduction, hopping conduction and ionic conduction.

Poole-Frenkel Conduction

A schematic of the energy band diagram for Poole-Frenkel (P-F) conduction is shown in **Fig. 2.4 (c)**. This process is analogous to Schottky emission, but in this case the conduction is bulk-limited and the electrons are emitted from the trap-sites into the conduction band [89]. In P-F emission, the trap-barriers are overcome by the carriers through thermionic emission [87], and the applied electric field lowers the potential barrier of the electrons, which in turn increases the probability of electron emission. The current density under P-F emission is expressed as [87]

$$J = q\mu N_C E \cdot \exp \left(-q \left(\phi_T - \sqrt{\frac{qE}{\pi \epsilon_0 \epsilon_i}} \right) / k_B T \right) \quad (2.5)$$

Where, μ is the electron mobility, N_C is the density of states in the conduction band, E is the electric field, $q\phi_T$ is the trap-level energy (activation energy). Since the activation energy can be regarded as the effective potential barrier height seen by the trapped electron, a barrier lowering by the applied field also results in a decrease of activation energy. For any system

with a large trap density, the P-F emission can be expressed as [90]:

$$J = \alpha \cdot \exp\left(-q \frac{\phi_T}{k_B T}\right) \sinh\left(\frac{\beta E}{2k_B T}\right) \quad (2.6)$$

Where, α is a pre-exponential factor which depends on the trap density, β is a field enhancement factor, E is the local electric field, $q\phi_T$ is the trap-level energy (activation energy).

Hopping Conduction

A schematic of the energy band diagram for hopping conduction is shown in **Fig. 2.4 (d)**. In this case, electrons hop between trap sites when an electric field is applied [89, 91]. In contrast to the P-F conduction the carrier energy is lower than the energy of the potential barrier between two trap-sites and the hopping conduction is based on the tunnelling of trapped electrons from one trap-site to another [92]. The current density under hopping conduction is expressed as [87]:

$$J = qan\nu \cdot \exp\left(\frac{qaE - E_{ac}}{k_B T}\right) \quad (2.7)$$

Where, a is the average hopping distance, n is the concentration of electrons in the conduction band of the dielectric and ν is the (thermal) vibrational frequency of electrons at the trap sites and E_{ac} is the activation energy.

Ionic Conduction

As the name indicates, ionic conduction is mediated by the movement of ions when subjected to an external electric field. In this case, ions jump over a potential barrier under the influence of an electric field and move from one defect site to another. The current density under ionic conduction is expressed as [87]:

$$J = J_0 \cdot \exp\left(\frac{q\phi_B}{k_B T} - \frac{qdE}{2k_B T}\right) \quad (2.8)$$

Where, J_0 is the pre-exponential factor, d is the spacing between two adjacent hopping sites, ϕ_B is the activation energy, and E is the applied electric field. The other terms have their usual meanings.

2.3 Metal-insulator Transition

Many transition metal oxides (TMO) exhibit a metal-insulator transition (abbreviated as MIT or IMT) in which the oxide conductivity increases by several orders of magnitude in response to an external stimulus (e.g., electrical, magnetic, optical, mechanical, and thermal stresses etc.). IMT can be introduced due to a diverse range of phenomena, including Mott transition (which involves electron-electron interaction), Peierls transition (which involves electron-phonon interaction), or Anderson localisation (which arises from a disorder-induced localisation) [93].

2.3.1 Mott transition

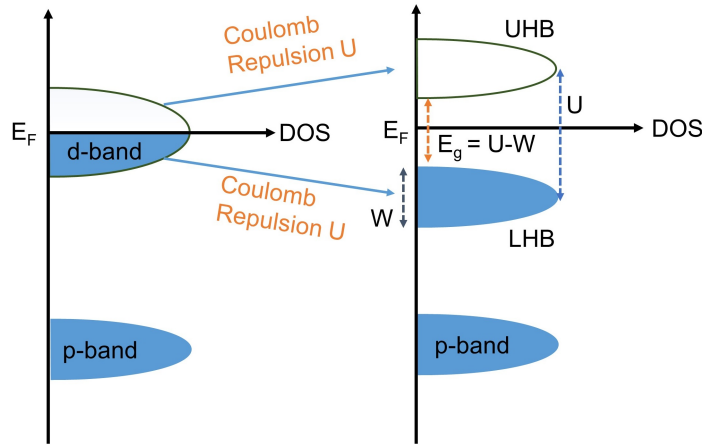


Figure 2.5: Band diagram of Mott-Hubbard Insulator (reproduced from Ref.[67]).

Classical band theory successfully explained the distinction between metals and insulators by showing their difference in electronic structures. From a classical viewpoint, metals have a zero bandgap, and their conduction band is partially filled with electrons. In contrast, insulators have a well-defined band gap (typically large) with a fully occupied valance band and completely empty conduction band. Interestingly, some transition metal oxides with an odd number of electrons per lattice site were found to be insulators, contrary to the expected metallic behaviour based on the classical band theory [94]. These materials are now termed as ‘Mott’, or ‘Mott-Hubbard’ insulators and their behaviour was explained by Nevill Mott a couple of decades ago [95], who considered a strong electron-electron correlation effect that occurs in the d- or f- orbitals of the transition metal. Mott described that the metal-insulator transition can be understood due to a variation of lattice constant ‘a’ by imagining a periodic arrangement of hydrogen-like atoms. According to Mott, the criterion for a metal-insulator

transition is [94]: $n^{1/3}$. $a_H = 0.2$ where, ‘n’ is the number of electrons per unit volume and ‘ a_H ’ is the hydrogen radius.

This theory was further developed by Hubbard by neglecting the long-range Coulomb forces between electrons and only considering electron-electron interaction when they are on the same atom. A band splitting occurs for large values of ‘a’ and arises from a competition between the kinetic energy of electrons to hop from one lattice site to another (which is already occupied by another electron) and the coulomb repulsion energy (U) between the electrons. As the coulomb potential energy (U) increases the energy band starts to split and two non-degenerate bands form when it surpasses the band width (W). As a result, the initial half-filled single energy band disintegrates into two bands with one fully occupied band named as lower Hubbard band (LHB) and another completely empty band named as upper Hubbard band (UHB) (see **Fig. 2.5**). A band overlap between the LHB and UHB then triggers the insulator-to-metal transition induced by external factors like temperature, pressure or electric fields [94]. Mott MIT is observed in numerous inorganic and organic materials, such as transition metal based oxide and sulphide systems and layered organic compounds [92, 94, 96]. VO_2 and V_2O_3 are among the well established materials that exhibit such type of transition [94, 97].

2.3.2 Peierls Transition

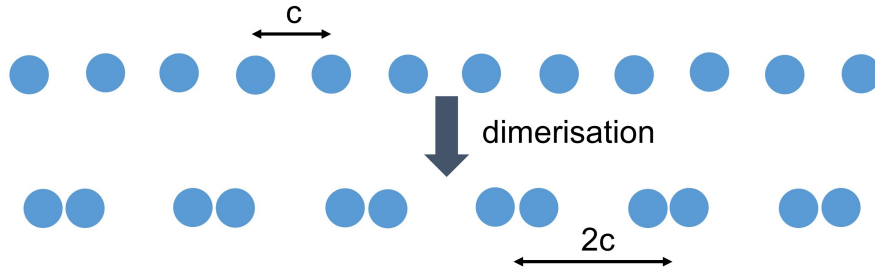


Figure 2.6: Dimerisation in a one-dimensional chain of atoms.

Peierls transition occurs from an electron-phonon interaction mediated by a structural change, such as dimerisation of atoms [98]. In this case, the ground state energy is minimised by a lattice distortion due to contributions from electronic and elastic energy of ions. Specifically, at a critical temperature a structural transformation occurs between a periodic lattice and a distorted phase which modifies the band structure of the material, thus leading to a change of its electronic properties, including conductivity and band gap.

Fig. 2.6 shows an example of a lattice distortion due to dimerisation in a one-dimensional chain of lattice containing one electron per lattice point. Above a critical temperature (T_p)

the atoms are periodically arranged with equal spaces between them (with lattice constant ‘ c ’) and the chain of atoms shows metallic conduction. Below this temperature T_p , a dimerisation occurs to minimise the energy and the lattice constant doubles ($2c$). This in turn modifies the band structure leading to an opening of a band gap and the material becomes insulating. Thus, a metal-to-insulator transition occurs by cooling down the material below the critical temperature T_p , or vice-versa. As an example, $K_{0.3}MoO_3$ is a Peierls insulator which exhibits MIT associated with a structural change at a critical temperature around 181 K [96, 98].

2.3.3 Anderson Localisation

In crystalline solids (e.g., metals) the electrical conduction can be assumed as non-scattering propagation of electron waves termed as ‘Bloch waves’. However, in his seminal work in 1958 [99], Anderson proposed that a large number of randomly distributed impurities or defects can induce localisation of electron waves. In other words, electron transport in crystalline solids can be attenuated due to scattering by impurities or defects which eventually reduce their mean free path, thus affecting their electrical conductivity. Anderson localisation is based on the phenomena of electron trapping in random potential leading to a disorder-driven metal-insulator transition [94]. In this case, the electronic states in metals can transform from extended states into localised states depending on the degree of disorder in potential [100]. Under such condition the Eigen states of the Hamiltonian are localised and electromagnetic waves cannot penetrate the medium and thus thermalisation fails to occur. Although originally predicted for electron systems, Anderson localisation is also observed for photons, classical waves, matter waves, and cold atoms [100]. MIT driven by Anderson localisation is commonly observed in strongly disordered material systems, including selenium-doped germanium, phosphorus-doped silicon, etc. [96]

2.4 Material properties and memristive switching responses of the Nb-O system

2.4.1 The Nb-O system

In the niobium-oxygen system, niobium can exist in four distinct chemical states (0 , 2^+ , 4^+ , and 5^+), which are generally assigned to the phases of metallic niobium (Nb), NbO, NbO₂ and Nb₂O₅ respectively [101, 102], as shown schematically in **Fig. 2.7**. The earliest phase diagram of Nb-O system was proposed by Elliot [103] in 1960 which described these four thermodynamically stable phases. In addition, a range of stable and metastable non-

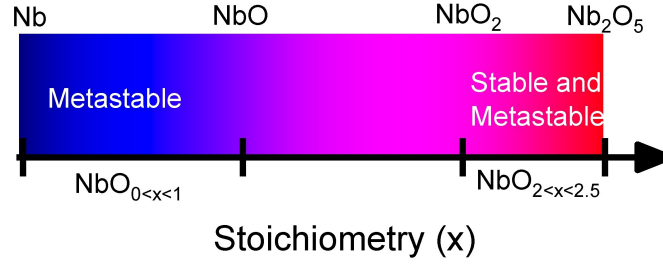


Figure 2.7: Schematic representation of different charge states of niobium (reproduced from Ref. [101]).

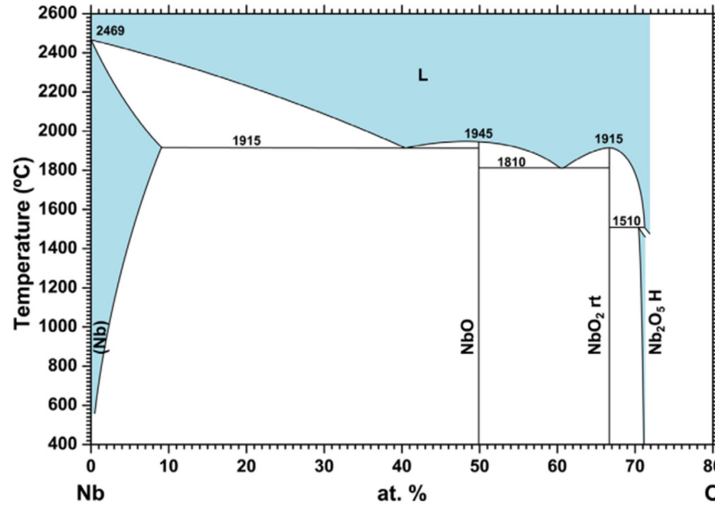


Figure 2.8: Phase diagram of Nb-O system (reprinted from Ref. [101]).

stoichiometric niobium oxides (NbO_x ($0 < x < 1$ and $2 < x < 2.5$)) have been reported [104–110]. The following section provides a brief overview of the abovementioned niobium oxides as well as pure metallic niobium characteristics along with their technological interests.

Niobium (also called columbium) is a metallic element in the group 5 of periodic table with an atomic number 41 and density of 8.57 g/cm^3 [111]. The electronic configuration of Nb is $[\text{Kr}].4d^4.5s^1$ and in pure metallic form it has a body-centred-cubic (bcc) crystal structure. Nb is a refractory metal with a relatively high thermal conductivity (52 W/m/K), high melting point (2750 K), and high boiling point (5017 K) [111]. The reported electrical conductivity of Nb is of the order of 10^4 S/cm (see **Table 2.1**) and it becomes superconductive below a critical temperature (T_c) of 9.3K [111]. It also possess high affinity and binding energy to oxygen, which often leads to a surface oxide layer when exposed to air [108]. Oxygen inclusion in the Nb matrix affects the electrical conductivity, which decreases with an

Table 2.1: Material properties of Niobium and Niobium Oxides

Phase	Electrical conductivity at 300K, (σ_{dc}) (S cm ⁻¹)	Ref.	Dielectric Constant (ϵ) at 300K,	Ref.	Band gap (eV)	Ref.
Nb	6.5×10^4 2.5×10^4	[111] [112]				
NbO	4.8×10^4	[113]				
Amorphous NbO ₂	$\sim 10^{-1}$	[114]				
NbO ₂ (tetragonal)	$\sim 10^{-4}$	[115]	~ 10 (1kHz to 10 MHz)	[116]	~ 0.5 ~ 0.7 ~ 0.88 ~ 1.0	[117] [118] [119] [120]
NbO ₂ (rutile)	$\sim 10^3$	[115]				
Poly-crystalline NbO ₂	$\sim 10^{-4}$	[121]				
Amorphous Nb ₂ O ₅	$\sim 10^{-11}$ $\sim 10^{-13}$ $\sim 10^{-12}$ - $\sim 10^{-11}$	[122] [126] [128]	41 (dc)	[123, 124]	3.4 3.4 - 5.3	[125] [127]
T-Nb ₂ O ₅	3.7×10^{-10} $\sim 10^{-13}$ - $\sim 10^{-11}$	[129] [130]	39 (100 kHz) 60-77 (100 kHz)	[129] [130]	3.4	[129]
H-Nb ₂ O ₅	7.6×10^{-7} 3×10^{-6} 10^{-8} - 10^{-6}	[129] [131] [130]	38 -160 (100 kHz) 16-130 (100 kHz)	[129] [130]	3	[129]
M-Nb ₂ O ₅					3.75	[132]
B-Nb ₂ O ₅			~ 5 (dc)	[133]	2.55	[118]
NbO _x	$\sim 10^{-6}$ - $\sim 10^3$ $\sim 2 \times 10^{-5}$ - $\sim 3.2 \times 10^0$	[131] [134]			3.8 -2 (optical)	[134]

increase of oxygen content [101, 108, 135]. The application of Niobium and Nb-based alloys is spread over a range of technological areas, including high-grade structural steel, corrosion-preventive coatings, superalloys for jet engine components, gas turbines, heat resisting and combustion equipment, superconducting systems, bio-compatible implants, electrode material for electronic devices etc. [13, 101, 136–138]

Niobium monoxide (NbO) has a face-centred cubic (fcc) crystal structure [139] and often contains a significant concentration of point defects [102]. NbO typically exhibits metallic conductivity [101] (see **Table 2.1**) and becomes superconductive below a transition temperature (T_c) of ~ 1.4 K [140]. It has been reported that the electrical resistivity of this oxide is highly sensitive to the oxygen-to-niobium ratio, and a slight decrease in oxygen concentration leads to an increase of conductivity and an increase of T_c [140, 141]. Apart from superconducting applications of NbO, its interesting oxygen diffusion properties is utilised for some electronic devices, including field-effect transistor and solid electrolytic capacitors [72, 142–144].

Niobium dioxide (NbO₂) is an n-type semiconductor with a band gap varying between 0.5 eV and 1.2 eV [101, 145] (also see **Table 2.1**). Stoichiometric NbO₂ can be obtained by oxidising Nb or NbO, or reducing Nb₂O₅ [146]. It has a melting point ~ 2174 K [102, 111]. In crystalline form it has a tetragonal structure with a distorted rutile sub-lattice at room temperature. The tetragonal unit cell is shown in **Fig. 2.9 (a)** which is characterised by pairs of edge-shared NbO₆ octahedrons that are cross-linked by corner sharing [101, 147]. When heated to around 1070 K, NbO₂ undergoes a reversible structural phase transition leading to a regular rutile structure as shown in **Fig. 2.9 (b)** [115]. This gives rise to an insulator-to-metal-transition (IMT) which results in an abrupt increase of electrical conductivity [101, 148]. A similar transition is also observed in VO₂ which is generally understood as a Mott-Peierls transition [101, 145, 149, 150]. NbO₂ has been of great interest for technological applications including circuit component for neuromorphic computing [49, 151, 152], electrocatalysts [153], optical modulators [119], diode and electron emitters, thermoelectric devices [154] etc.

Niobium pentoxide (Nb₂O₅) is an insulator with a large band gap (see **Table 2.1**). Nb₂O₅ can exist in an amorphous phase, but can also take form of several crystalline polymorphs, including TT, T, M, and H-Nb₂O₅ depending on the deposition or post-deposition annealing condition [101] (The name of these polymorphs are derived from the German words Tief-Tief, Tief, Medium and Hoch, respectively denoting low-low, low, medium and high, which is based on the temperature required to obtain a particular phase [155]). Several other polymorphs were named as B, N, R (derived from German Blätter, Nadeln and Prismen, respectively which denote leaves/plates, needles and prisms respectively) based on

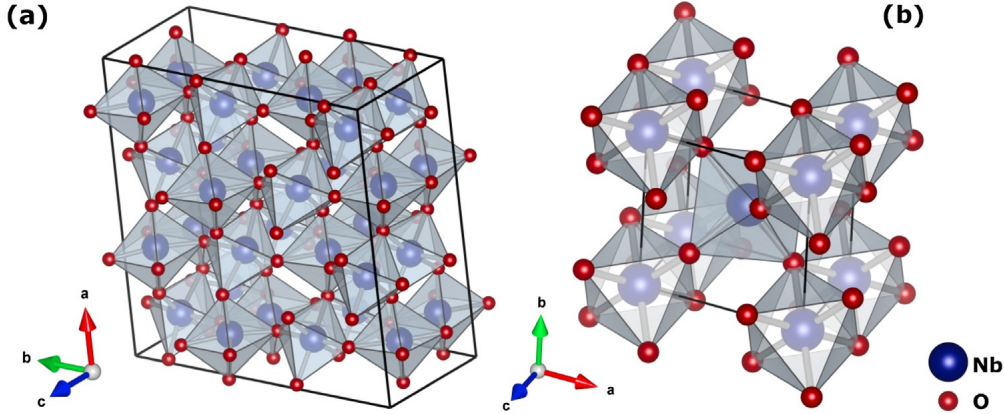


Figure 2.9: Crystal structure of NbO_2 : (a) tetragonal, and (b) rutile structures (reprinted from Ref. [101]).

the shape of the crystallites [101]. Among different polymorphs $\text{H-Nb}_2\text{O}_5$ is the most commonly obtained phase and the structure is shown in **Fig. 2.10**. It has been reported that the type of polymorph and its synthesis condition control the physical properties of Nb_2O_5 [101, 156, 157]. Among different niobium oxides Nb_2O_5 has a relatively lower electrical conductivity varying between 10^{-6} S/cm and $\sim 10^{-13}$ S/cm (see **Table 2.1**). The technological interest of Nb_2O_5 is in the areas of memristor, sensors, MIM capacitors and catalysts, to name a few [82, 158–161].

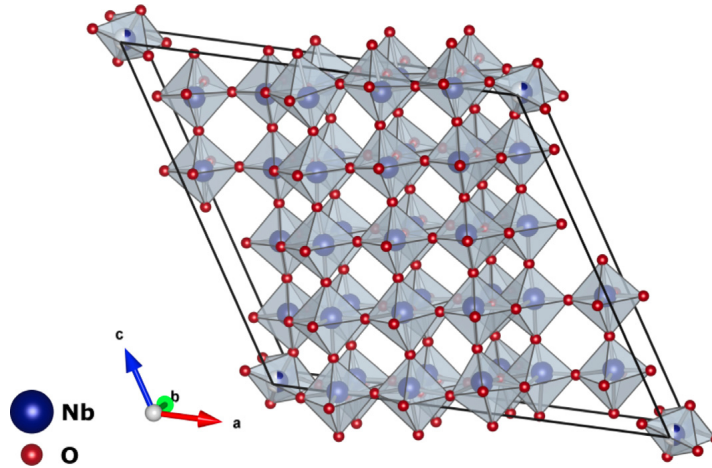


Figure 2.10: Crystal structure of $\text{H-Nb}_2\text{O}_5$ (reprinted from Ref. [101]).

Apart from the above distinct stoichiometric phases, a range of non-stoichiometric niobium oxides (NbO_x with $0 < x < 1$ and $2 < x < 2.5$) have also been reported. While those in the range $0 < x < 1$ were metastable, stable phases were observed in the range $2 < x < 2.5$, i.e., stoichiometry between NbO_2 and Nb_2O_5 [101, 134]. The variation in the stoichiometry was linked to the presence of point defects, Nb interstitials and oxygen vacancies [101].

In particular, variation in the oxygen vacancy concentration has been reported to cause a significant change of the oxide conductivity [162]. These non-stoichiometric phases can be achieved by controlled oxidation of lower stoichiometric niobium oxides (such as NbO, or NbO₂), reducing Nb₂O₅ at high temperatures, or by sequential deposition of metal-rich and oxygen-rich layers to form a graded composition [101, 134].

2.4.2 Switching phenomena in Niobium Oxides

Memristive switching phenomena have been reported for niobium oxides since 1960s, including non-volatile resistive switching, volatile threshold switching (or, current-controlled NDR) and a combined resistive and threshold switching [32, 57–60]. These diverse responses offer great advantages for different applications, but the particular response depends on the film stoichiometry, crystallinity, electrode metals, device geometry and operating conditions (e.g., maximum currents, bias direction etc.) [82, 163, 164]. For example, Nb₂O₅ shows high thermodynamic stability and it is one of the first materials that exhibited resistive switching effect [165]. A unipolar (or non-polar) switching effect is often reported when inert top and bottom electrodes are used [166]. In this case, due to the inert electrodes, the stoichiometry of the Nb₂O₅ is maintained, and a thermally driven unipolar switching mode dominates. On the other hand, structural asymmetry is often reported to favour an electric field dependent bipolar switching [167, 168]. Specifically, the switching response of Nb₂O₅ can be altered from a unipolar to a bipolar mode by replacing one of the inert electrodes with a reactive metal (e.g. Al) [167, 169]. In this case, the reactive electrode reacts with the stoichiometric Nb₂O₅ layer to form a thin interfacial oxide which in turn influences the switching mode [57].

In contrast, a volatile threshold switching or NDR response is often observed in NbO₂ and non-stoichiometric NbO_x phases [170, 171]. Interestingly, recent studies have shown that this particular response (i.e., threshold switching) can also be realised in Nb₂O₅ when specific reactive electrodes (e.g., Nb, Ti, TiN) are used. In this case the threshold switching often co-exists with a memory filament and the active threshold switching volume is localised in the vicinity of the oxide/metal interface [48, 82].

A wide range of synthesis routes have been employed to achieve niobium oxides that exhibit memristive switching phenomena, including non-reactive and reactive sputter deposition, pulsed laser deposition, molecular beam epitaxy, thermal oxidation and reactive bias target ion beam deposition [32, 44, 172–177]. While epitaxial or poly-crystalline NbO₂ and Nb₂O₅ phases are typically achieved through high temperature processing routes [175, 178], the sub-stoichiometric NbO_x phases can be obtained by either controlling the atmospheric conditions inside the deposition chamber [80, 173, 179], using a reactive electrode (e.g. Nb or TiN) [13] or by using ion-implantation in a stoichiometric Nb₂O₅ layer [163]. The latter

has the advantage that it can be limited to localised regions [57].

2.5 State of the art

2.5.1 Understanding the electroforming process in MOM structures

The memristive responses in MOM devices are commonly mediated by filamentary conduction, either in the form of a semi-permanent filament created by compositional changes in the oxide or as a transient filament created by inhomogeneous current or field distributions (e.g., current bifurcation). In the former case, semi-permanent filaments are created by an initial electroforming step and are typically comprised of oxygen vacancies mediated by the generation, drift and diffusion of oxygen ions in response to the applied electrical stress (i.e., bias voltage) and local Joule heating [180, 181]. In this case, the forming voltage generally scales with the thickness of the oxide layer. As such, the process is consistent with an electric-field-induced soft dielectric breakdown process, [182–184] in which defects are believed to be generated heterogeneously at the oxide/electrode interface by local redox (oxidation/reduction) reactions. These defects then further drift and diffuse to create a conduction path between the electrodes [90, 185, 186]. In contrast, transient filaments (e.g., current filaments) can be formed in materials that exhibit S-type negative differential resistance (NDR) due to current bifurcation, a process in which a uniform current divides into domains of high and low current-density [75]. Significantly, both processes often lead to a local compositional change through the oxide film due to the motion of ions along the electric field or as a consequence of their lateral motion due to the temperature gradient (Soret effect) [187–189]. These in turn create low resistance paths through the device structure that can cause significant temperature increase due to local Joule heating when carrying current [78, 190]. Consequently, knowing the size, composition, structure and spatial distribution of the filamentary path is an essential requirement for a full understanding of filamentary memristive switching and for effective device modelling and optimisation.

Several studies have carried out the compositional analysis of the filamentary region by employing different techniques, including conducting atomic force microscopy (C-AFM) [191], transmission synchrotron x-ray spectromicroscopy [192], high-resolution transmission electron microscopy (HRTEM) and electron energy loss spectroscopy (EELS) [193, 194] etc. For example, Kumar et al. reported a thermal decomposition of TaO_x films when subjected to a voltage sweep and attributed this to thermophoresis of oxygen led by current density decomposition under voltage-controlled testing [192]. Other studies have also reported a thermal decomposition of the oxide film in a temperature field (Soret effect), but with a

migration of metal ions rather than oxygen [79, 195–197]. Additionally, a current bifurcation process has been reported in the latter studies [79, 197], distinct from that proposed by Kumar et al. who reported a field bifurcation process [192].

In addition to the electroforming mechanism, the operating condition such as the maximum current during the electroforming step has also been reported to play a critical role in determining the dimension, resistance and stability of the resulting filament [185, 198]. In particular, the associated compositional or structural changes in the oxide film or at the oxide/electrode interface can significantly affect the post-forming switching characteristics [199, 200]. Understanding details of the electroforming process is therefore a necessary requirement for developing devices with specific memristive-switching response. Moreover, understanding the differences between electric-field and thermally induced electroforming and the role of current bifurcation is also important from both scientific and technological viewpoints.

2.5.2 Material and device dependencies of memristive switching in MOM structures

Many materials have been found to exhibit memristive switching and binary oxides have attracted particular attention due to their simple structure, CMOS compatibility, low cost and great control over the material composition [56]. In MOM configuration binary oxides exhibit both volatile and non-volatile resistance changes [57, 201, 202] and significant advancements have been achieved in understanding their physical and physiochemical processes which govern the switching response, device reliability, uniformity and switching kinetics respectively [202–204].

Among different aspects of device and material dependencies, understanding the role of metal/oxide interfaces in determining the memristive switching mechanism has been an important area of recent investigation [205–210]. Indeed, the interaction between the metal-oxide interfaces plays a crucial role since it is reported as the dominant cause of contact-failure, chemical oxidation, morphological changes and dissolution of electrode metals [211–213]. Recent studies have shown that some electrode metals (e.g. Ta, Hf, Nb etc.) can be oxidised from the adjacent oxide to form an intermediate layer [202, 214], the extent of which is largely determined by the relative thicknesses of the oxide and the electrode metal [214], the oxygen affinity of the metal species and the decomposition stability of the oxide material, respectively [202]. This in turn determines the dominant switching mode, and plays a critical role to enhance device stability and reproducibility [202]. For example, it has been reported that using Al electrodes with an Nb_2O_5 layer leads to bipolar switching

rather than the unipolar response observed for Pt/Nb₂O₅/Pt structures [57, 167, 169]. A configurable switching response from a bipolar to threshold switching has also been reported in Nb/HfO₂/Pt structures where the transition in the dominant mode was attributed to self-assembly of an NbO_{2-δ} inter-layer formed by the metal/oxide interface reactions [83]. Similar characteristics have been observed in V/HfO₂/TiN structures where the threshold switching characteristics was attributed to the formation of a VO_x inter-layer at the V/HfO₂ interface [201]. Other studies have shown that a meta-stable TaO₂ was formed at the Ta/Ta₂O₅ interface which mediated the Ta oxidation process [215] and in Hf/HfO₂/Pt structures a HfO_x interlayer formed at the Hf/HfO₂ interface which improved the device performance and switching characteristics [202]. In addition to the interface reactions, the Schottky-barrier formed at the metal/oxide interface has also been demonstrated to modify the device response and can be used to make devices with lower leakage current, higher endurance and greater switching speed [216]. Thus, understanding details of the metal/oxide interfaces (including interface reactions and interface barriers) is an essential requirement for developing devices with specific memristive-switching response as well as improving their reliability and uniformity for practical applications.

Other important aspects that significantly affect the switching response include device scaling, oxide thickness, and oxide composition [164, 217, 218]. For example, the forming voltage of MOM devices scales with device area, and oxide thickness directly affects their important performance parameters, including SET/RESET voltages, leakage current, and switching window [56]. The dominant switching mode is determined by the film composition which is evident from the observed unipolar switching in Pt/Nb₂O₅/Pt structures, while threshold switching has been observed in Pt/NbO_x/Pt ($x < 2.5$) and Pt/NbO₂/Pt structures [174, 219] respectively. Interestingly, a thickness-dependent modulation of the threshold voltages has been reported for niobium-oxide-based MOM devices [220–222]. However, thickness independent characteristics have also been reported for amorphous NbO₂ [173] and Nb₂O₅ [82] films, but for the latter case, analysis of area-dependent characteristics indicated that the switching volume is localised after electroforming [82]. While these analyses were based on devices that underwent an initial electroforming condition, a forming-free response has also been reported recently [78, 164]. In brief, there are considerable variations in realising a particular memristive response depending on the oxide composition, and a great deal of difference is also observed in the reported switching parameters which are apparently influenced by the device area and oxide and metal thicknesses.

Furthermore, it is often reported that the memristive response of MOM structures can be improved by metal-doping of the functional oxide layer. For example, doping Ge (or Gd, or Cu) in HfO₂, Cr in ZnO, and Al in CeO₂ were reported to significantly improve the device

reliability, endurance, and switching stability [223–227]. The effectiveness of this approach was broadly attributed to the charge transfer ability of the dopant element and reduction of defect formation energy [56, 227].

Therefore, with all these implications for different oxides, characterising memristive switching property of niobium oxide-based MOM devices as a function of device area, film thickness, metal doping and oxide stoichiometry are important issues in their development and further systematic studies are clearly required to advance the understanding.

2.5.3 The physical origin of diverse threshold switching modes in NbO_x

As discussed earlier, the niobium-oxygen system exhibits complex and rich memristive responses that include non-volatile resistive switching, volatile threshold switching and a combined resistive-threshold switching. Since the functionality of such devices depends on their current-voltage characteristics [48, 49], it is important to understand the physical basis of switching and the way it is affected by film stoichiometry, crystallinity, device structure and operating conditions. A volatile threshold switching or NDR response is often observed in crystalline NbO_2 which was historically attributed to the reversible insulator-to-metal (IMT) phase transition in NbO_2 from a low temperature tetragonal structure to a high-temperature rutile structure near $T_c \sim 1100$ K. However, the responsible mechanism appeared to be more complex due to the fact that this type of switching was also reported in Nb_2O_5 and NbO_x thin films that were initially amorphous [82, 171]. Despite these complexities, multiple studies have shown that the S-type NDR in amorphous binary oxides can be well modelled by combining a temperature-dependent conduction (e.g., Poole-Frenkel emission) with local Joule heating [82, 171, 217, 228, 229]. Indeed, this understanding was recently generalised by Gibson, who has shown that the S-type NDR can arise from any conduction mechanism that exhibits a super-linear temperature dependence [77]. This study provides a basis for understanding the origin of S-type NDR characteristics and also provides pathway for engineering device response for different applications. However, the above studies do not provide any insight about the origin of other NDR characteristics exhibited by thin film oxides, including the discontinuous snapback response observed in NbO_x [78], TaO_x [79], and SiO_x [230]. This particular snapback response is characterised by an abrupt hysteretic voltage change when a bidirectional current sweep is employed (**Fig. 2.11 (a)**), and is also observed in chalcogenide glasses [231].

A more complex combinations of S-type and snapback characteristics (**Fig. 2.11 (b)**) have been reported recently which provides additional functionalities for emerging neuro-

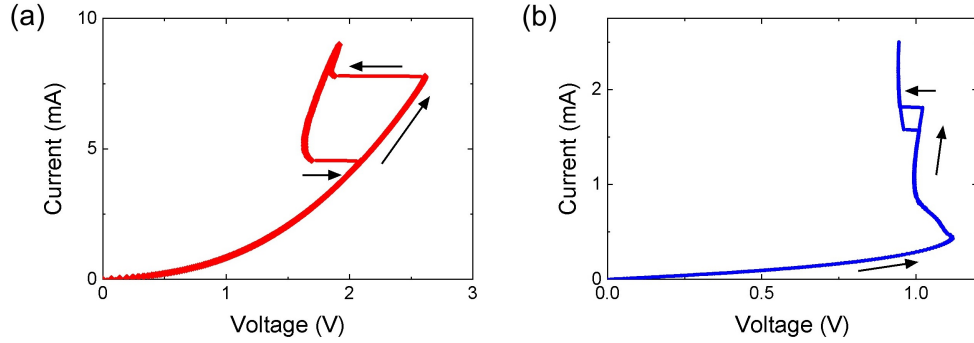


Figure 2.11: Different current-controlled NDR modes observed in NbO_x -based MOM devices: (a) snapback NDR, and (b) combined S-type and snapback NDR.

morphic computing [49, 151]. In an effort to understand the origin of such complex NDR response, Kumar et. al. [78] employed in-situ temperature mapping of amorphous NbO_x subjected to different current levels. In this study the S-type NDR was found to occur at ~ 400 K, consistent with trap-assisted Poole-Frenkel conduction, while the discontinuous snapback was found to occur at ~ 1000 K and was attributed to the known insulator-to-metal-transition (IMT) in NbO_2 [170]. However, the latter mechanism fails to account for similar snapback behaviour observed in other oxides such as TaO_x [79] that do not show a material specific phase transition. Further studies are clearly required to understand the physical origin of this snapback response and its dependencies on material and device-specific parameters.

Experimental and Modelling Details

This chapter contains an outline of the experimental procedures and characterisation techniques employed for the studies in the subsequent chapters. The NbO_x films with various composition were deposited by dc sputtering of Nb target with varying ambient and radio-frequency (rf) sputtering of a Nb_2O_5 target respectively. They were analysed by Rutherford back scattering spectroscopy (RBS), X-ray photoemission spectroscopy (XPS), X-ray diffraction (XRD) and transmission electron microscopy (TEM). Specifically, RBS and XPS were used to investigate the composition and oxidation states in the NbO_x films. XRD and TEM were used for structural analysis and thickness measurements, respectively. The latter was also used for elemental composition mapping. The electrical characteristics of the MOM device structures were investigated using a semiconductor parametric analyser and switching mechanism was studied with in-situ temperature mapping. **Chapter 3** concludes with the description of a simple two-zone model of threshold switching that is shown to explain diverse NDR characteristics in MOM structures. Details of the specific experimental procedures and model parameters are described in the following chapters.

3.1 Device Fabrication

MOM cross-point test structures with device dimensions ranging from $2 \times 2 \mu\text{m}^2$ to $20 \times 20 \mu\text{m}^2$ were fabricated on thermally oxidised silicon wafers, as shown in **Fig. 3.1**.

Bottom and top electrodes were defined by a standard photolithographic lift-off process, with metal layers deposited by electron-beam evaporation. The bottom electrode typically comprised of a Ti (or Cr or Nb) adhesion layer and a Pt contact layer, as shown for a $20 \times 20 \mu\text{m}^2$ device in **Fig. 3.2(a)**. NbO_x layers of varied composition were subsequently deposited using either rf sputtering of a Nb_2O_5 target in an Ar ambient or dc sputtering

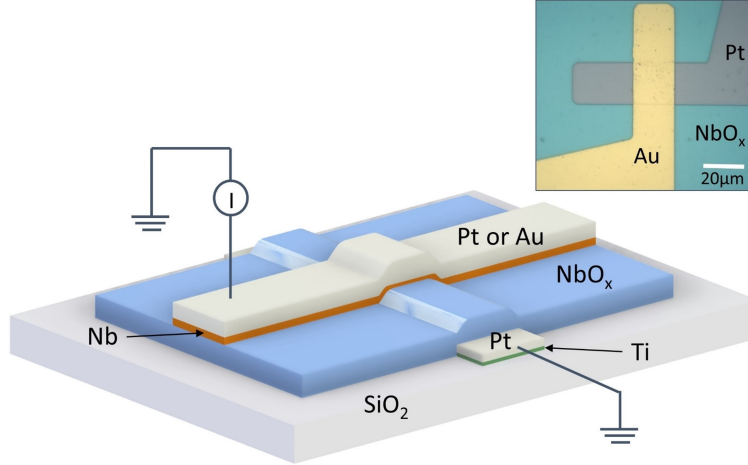


Figure 3.1: Three-dimensional schematic of the cross-point device structure with corresponding material layers. Inset shows an optical microscopy image of typical Au/Nb/NbO_x/Pt cross-point device with 20 μm × 20 μm active device area.

of a Nb target in an O₂/Ar ambient of varied gas ratio. The cross-point structures were completed by depositing the top electrodes (TE), which typically consisted of a Nb (or a reactive metal) adhesion layer of variable thickness and an inert Pt (or Au) contact layer, as shown in **Fig. 3.2(b)**. At this point the bottom contact pads remained covered with NbO_x and an etching step was required to access the bottom electrode (BE). This was achieved by photolithographically defining the access area and chemically etching the selected area in buffered hydrofluoric acid to remove the NbO_x layer. In specific cases, the removal of the oxide layer in the selected area was carried out by reactive ion etching (RIE) using chemically reactive plasma of ions generated from CHF₃ with a gas flow of 25 sccm and base pressure of ~ 20 mTorr. **Fig. 3.2(c)** shows the cross-point devices after etching the NbO_x layer to open the bottom contact pad. The substrate was then ultrasonically cleaned in acetone and isopropanol prior to deposition of an encapsulation layer. Finally, the devices were encapsulated with a thin positive photoresist layer (AZ 1512HS, MicroChemicals [232]), spun at 4000 rpm for 30 s. A photolithographic step was used to reopen access to the device contact pads (both top and bottom) by developing the exposed area for 1 min in AZ 726 (MicroChemicals [232]), as shown in **Fig. 3.2(d)**.

The measured top photoresist layer thickness was $\sim 1.1 \pm 0.12$ μm which was measured by a surface profilometer as shown in **Fig. 3.3**.

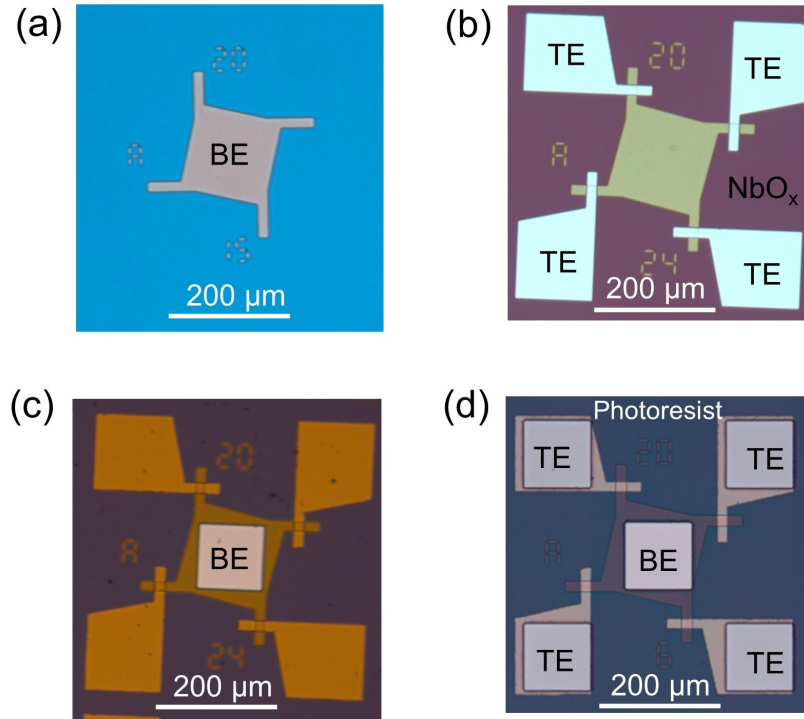


Figure 3.2: Optical micrograph of different steps of device fabrication: (a) image of a bottom electrode (BE) after the lift-off process for the Pt bottom electrode with a Ti adhesion layer, (b) image of four cross-point devices formed with a common bottom electrode after oxide and bottom electrode deposition, (c) the same devices after etching the oxide layer to expose the BE and, (d) after the final step (here wafer is coated with photoresist everywhere except the contact pads (BE and TE)).

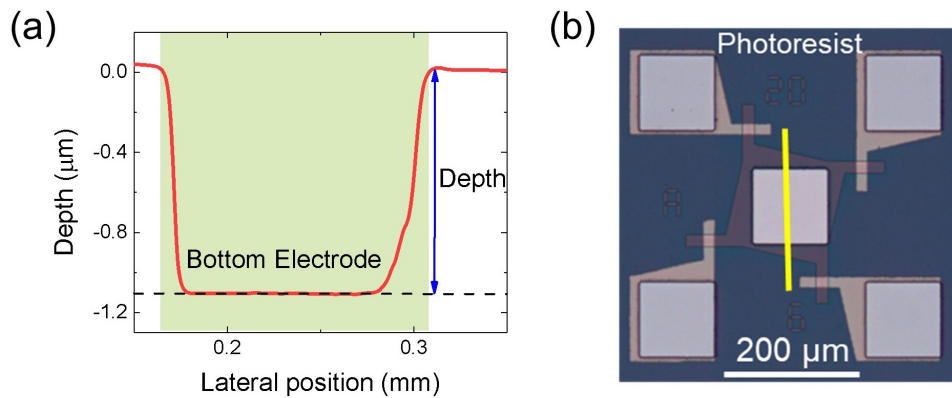


Figure 3.3: (a) Thickness of the photoresist measured using a surface profilometer and, (b) the position of the line scan shown on the device structure (the yellow line corresponds to the red line in Fig. 3.3(a)).

3.2 Thin Films Deposition and Analysis

3.2.1 Electron-beam Evaporation

The bottom and top electrode layers were deposited by e-beam evaporation using a Temescal BJD-2000 evaporator with a base pressure of $\sim 9 \times 10^{-6}$ Torr. The bottom electrodes typically consisted of a Ti adhesion layer followed by a Pt layer deposited onto a 300 nm thermal oxide layer on a Si (100) wafer without breaking vacuum. Variations on this typical device structure used Cr or Nb as the adhesion layer on a 200 nm thermally grown SiO₂. Inside the deposition chamber the metal layers were deposited by evaporating metal targets bombarded with focussed electron beams. The substrate temperature was maintained between 296.15 K and 333.15 K. The top electrode layers were deposited by the same procedure on top of the sputter deposited NbO_x films.

3.2.2 Sputter Deposition

Table 3.1: Sputter deposition conditions of NbO_x films

Deposition conditions of NbO _x thin films						
A. Near-stoichiometric NbO _x films (rf-sputtered)						
Target	Applied power (W)	Pressure (mTorr)	Gas flow (Ar/O ₂)	Thickness (nm)	'x' Value of NbO _x	of
Nb ₂ O ₅	180	4	20/0	60	2.6 ± 0.05	
Nb ₂ O ₅	180	4	20/0	60	2.6 ± 0.05	
Nb ₂ O ₅	180	4	20/0	45	2.6 ± 0.05	
Nb ₂ O ₅	180	4	20/0	40	2.6 ± 0.05	
Nb ₂ O ₅	180	4	20/0	30	2.6 ± 0.05	
Nb ₂ O ₅	180	4	20/0	20	2.6 ± 0.05	
B. Sub-stoichiometric NbO _x films (dc-sputtered)						
Nb	100	1.5	1 9/1	44.3	1.92 ± 0.03	
Nb	100	2	19/1	55	1.99 ± 0.03	
Nb	100	1.5	18.5/1.5	57.3	2.22 ± 0.03	
C. Sub-stoichiometric NbO _x films (dc-sputtered)						
Nb	100	2	18.5/1.5	93	2.15 ± 0.05	
Nb	100	2	18.5/1.5	77	2.1 ± 0.05	
Nb	100	2	18.5/1.5	55	1.95 ± 0.05	
Nb	100	2	18.5/1.5	35	1.95 ± 0.05	

NbO_x dielectric layers of varied composition were deposited using a commercial sputtering system (AJA ATC 2400 UHV). Stoichiometric Nb₂O₅ films were generally achieved by rf

sputtering of the Nb_2O_5 target at a base pressure ~ 4 mTorr and constant sputtering power of 180 W. In contrast, sub-stoichiometric NbO_x films with varying composition were achieved by dc sputtering of a Nb target by controlling the Ar/O_2 ratio of the process gas at a constant overall gas flow rate of 20 standard cubic centimetres per minute (sccm). All depositions were performed at room temperature (295 ± 5 K). Details of the deposition conditions are given in **Table 3.1**.

3.2.3 Compositional Analysis

The NbO_x stoichiometry was determined by Rutherford backscattering spectrometry (RBS) of films and was found to be in the range from $x = 1.92 (\pm 0.03)$ to $x = 2.6 (\pm 0.05)$. The thin films of NbO_x deposited on vitreous carbon or Si substrates were analysed with 2 MeV He^+ with detectors at scattering angles of 168° and 100° relative to the incident beam. The stoichiometry of the NbO_x was calculated by the ratio of the measured counts, and thickness was calculated by simulating the RBS spectra using RUMP [233].

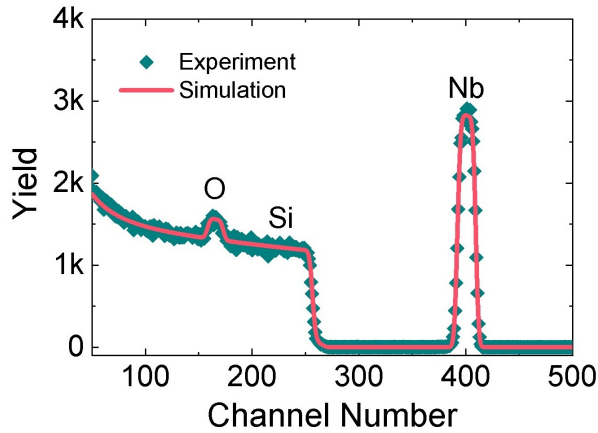


Figure 3.4: Representative RBS spectrum obtained from a dc reactively sputtered NbO_x ($x = 2.2$) thin film deposited on a Si substrate at Ar/O_2 (18.5/1.5) atmosphere.

Fig. 3.4 shows a representative RBS spectrum of a sub-stoichiometric NbO_x film deposited on a Si substrate obtained by dc reactive sputter deposition using a mixed Ar/O_2 (18.5/1.5) atmosphere (Pressure: 1.5 mTorr, Discharge power: 100 W). The spectrum shows well separated niobium and oxygen peaks that correspond to a stoichiometry of $x = 2.2 (\pm 0.03)$. The same analysis was used to determine the stoichiometry of films with x in the range from $1.92 (\pm 0.03)$ to $2.6 (\pm 0.05)$ (i.e., slightly over stoichiometric).

3.2.4 X-ray Photoelectron Spectroscopy

Selected NbO_x films were also analysed using X-ray photoelectron spectroscopy (XPS) performed in a Thermo Scientific (ESCALAB250Xi) instrument. In this case the NbO_x films were excited with a mono-chromatic Al $K\alpha$ X-ray source (energy 1486.68 eV) and the kinetic energy of the photo-emitted electrons were recorded and analysed.

A representative example of the XPS spectra from a sub-stoichiometric NbO_x ($x \sim 1.98$) film deposited on a Si substrate is shown in **Fig. 3.5**. Conventional peak fitting of the Nb 3d core level spectra shows contributions from the Nb^{2+} and Nb^{4+} oxidation states [234, 235] in the sub-stoichiometric NbO_x film. Similar analysis was used to determine the Nb oxidation states in stoichiometric Nb_2O_5 and Ti-doped Nb_2O_5 films. The XPS valence band spectra from the sub-stoichiometric NbO_x is shown in **Fig. 3.5(b)**, which exhibited a characteristic low energy band at lower binding energies (< 3 eV) due to unbonded Nb [236].

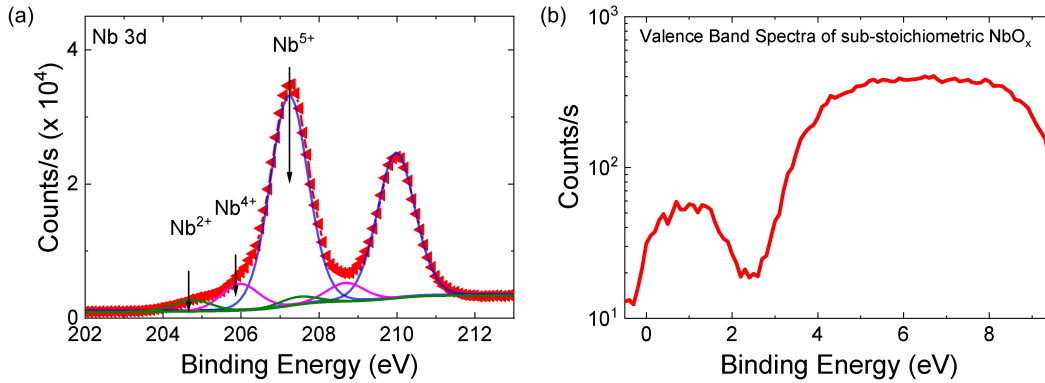


Figure 3.5: Representative XPS spectrum obtained from a dc reactively sputtered NbO_x thin film deposited on a Si substrate at Ar/O_2 (19/1) atmosphere: (a) Nb 3d core level spectrum, and (b) valence band spectrum for a sub-stoichiometric NbO_x ($x \sim 1.98 \pm 0.02$) film.

3.2.5 Crystallinity of the films

The structural properties of the as-deposited films were studied by grazing incidence X-ray diffraction (GIXRD) in a Hi-Resolution PANalytical X'Pert PRO MRD system with Cu- $K\alpha$ radiation using a wavelength of 1.545 Å. The X-ray diffractometer was operated at a fixed grazing angle of 0.6° to maximise sensitivity to the oxide film. **Fig. 3.6** shows a representative XRD spectrum of a sub-stoichiometric NbO_x ($x \sim 1.98$) film which confirms an amorphous film was obtained by sputtering at room temperature.

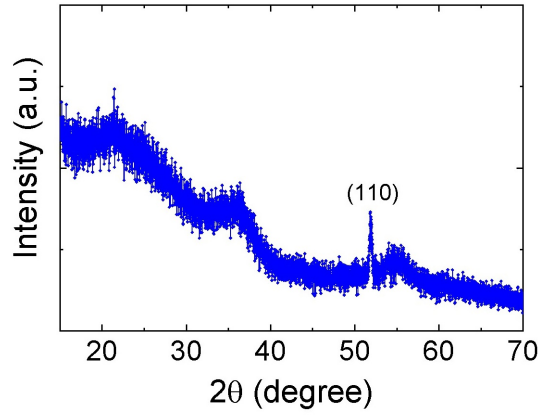


Figure 3.6: Representative XRD spectrum obtained from a sub-stoichiometric NbO_x ($x = 1.98 \pm 0.02$) thin film deposited on a Si substrate (a weak signal from (110) plane of Si substrate is observed).

3.3 Electrical Measurements

Electrical measurements were performed in atmospheric conditions using an Agilent B1500A semiconductor parameter analyser attached to a Signatone probe station (S-1160) and generally consisted of bidirectional quasi-static current sweeps. The resistive/threshold switching response was also studied using bidirectional voltage-controlled I-V sweeps. Temperature dependent electrical measurements were performed in air by heating the sample stage. In all cases the bias was applied through the top electrode while the bottom electrode was grounded.

3.4 In-situ Temperature Mapping

In-situ thermal imaging of the cross-point devices was performed using a TMX T°Imager®, a camera-based thermorefectance imaging system. The thermorefectance method is a non-contact and non-destructive method that is based on the temperature dependent optical properties of reflective surface materials. This method uses visible light illumination to provide deep submicron resolutions (100 nm – 300 nm), well beyond what is possible with other imaging techniques, such as infrared (3 – 10 μm) [237]. This technique is therefore well suited for the wide range of materials present in microelectronic devices.

The temperature-reflectance relation, represented by the Coefficient of Thermorefectance, C_{TR} , describes the unit change of reflectance per degree change in temperature, and is dependent on the surface material, roughness, illumination wavelength and optical aperture.

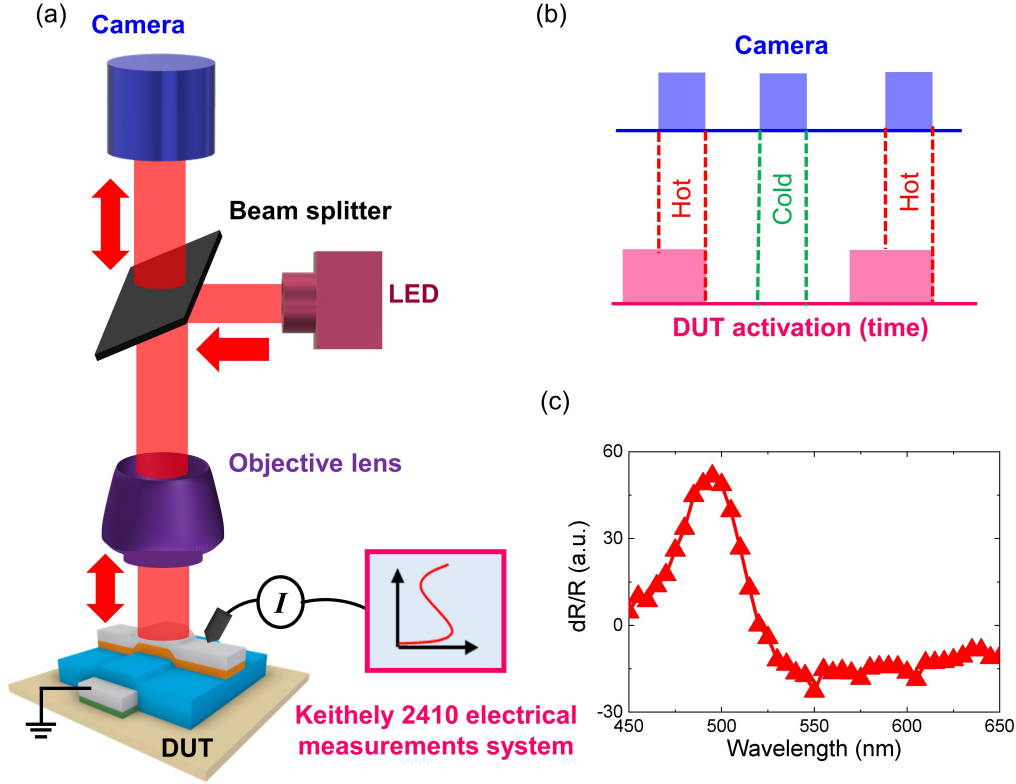


Figure 3.7: Thermoreflectance measurement setup. (a) A simple representation of the thermoreflectance measurement system with an objective lens and 490 nm illumination wavelength, (b) duration of the hot and cold cycles, where hot refers to the time when a current was applied to the device and cold refers to the time when the device was not electrically activated, and (c) thermoreflectance response of the gold surface under different illumination wavelengths.

For that reason, the C_{TR} coefficient must be obtained for each device through an in-situ calibration procedure where the temperature change is set using a controllable heating stage. During an activation experiment, the change in reflectance intensity due to Joule heating is acquired as the device is electrically activated, and the temperature rise is inferred from the reflectance change using the sample specific C_{TR} . The reflectance change is obtained from the change of light intensity collected on a photosensitive detector of a camera for both the activation and calibration sequences, providing a 1000×1000 pixel intensity map of the region of interest. For calibration, two temperatures of 20 °C and 40 °C are set within 0.1 °C using a Peltier heating stage, and 50 intensity frames are obtained at each of the two temperatures. During the measurement, the device is activated with a modulated pulse train while the camera collects 50 “hot” frames during the ON states and 50 “cold” frames during the OFF states alternating according to the pulsed electrical input. The “hot” and “cold” frames are then used to calculate the unit change in reflectance due to Joule heating

during the activation $\frac{\Delta R}{R}(i, j)_{\text{activ.}}$ and due to Peltier induced temperature change during the calibration $\frac{\Delta R}{R}(i, j)_{\text{calib.}}$.

$$C_{\text{TR}}(i, j) = \frac{1}{\Delta T_{\text{Stage}}} \left(\frac{\Delta R}{R}(i, j) \right)_{\text{calib.}} \quad (3.1)$$

$$T(i, j) = T_{\text{base}} + \frac{1}{C_{\text{TR}}(i, j)} \left(\frac{\Delta R}{R}(i, j) \right)_{\text{activ.}} \quad (3.2)$$

Equation (3.1-3.2) show the relations governing the calibration for C_{TR} and the activation temperature relative to the base temperature for each pixel (i, j) .

In-situ electrical measurements during thermoreflectance imaging were performed with a Keithley 2410 parameter analyser and included both dc and pulsed testing. In all cases the bias was applied through the top electrode while the bottom electrode was grounded.

3.5 Modelling of Device Behaviour

As discussed earlier (**Chapter 2, section 2.5.3**), a range of NDR modes including two basic types, continuous ‘S-type’ and discontinuous ‘snapback’ NDR, as well as more complex combinations can be observed in two terminal MOM devices [78, 152]. Understanding the physical origin of these modes is an essential requirement for realising devices with a specific response tailored for practical applications. To understand the origin of the snapback response and also to explain the diverse range of NDR modes observed in MOM devices, a two zone parallel-memristor model was recently developed [152]. This model is based on the fact that the current distribution in MOM structure is highly localised after electroforming, with the NDR response dominated by the region of highest current density (core) and the surrounding film (shell) acting as a parallel resistance (current divider) as shown in **Fig. 3.8 (a-b)**.

The threshold switching response then depends on the relative magnitudes of the maximum negative differential resistance (R_{NDR}) of the core (**Fig. 3.8(c)**) and the shell resistance (R_{S}). Although the total device current remains constrained under current controlled operation, the current ratio in the core and shell regions can freely respond to local conductivity changes. This can further facilitate a sudden decrease in core resistance if that of the shell is sufficiently low. When the parallel resistance R_{S} is much larger than R_{NDR} ($R_{\text{S}} \gg R_{\text{NDR}}$) the source current, I_{m} , flows predominantly through the core and gives rise to a continuous S-type NDR characteristics similar to that shown in **Fig. 3.8(d)**. In contrast, when R_{S} is less than R_{NDR} ($R_{\text{S}} < R_{\text{NDR}}$) the current flows mainly through the shell region and can

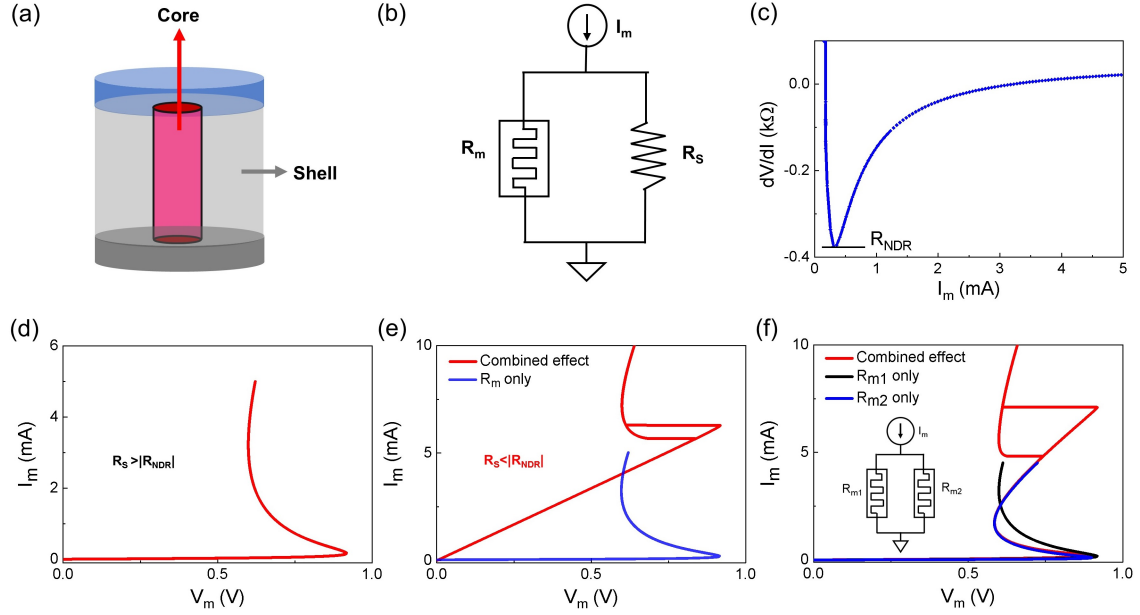


Figure 3.8: The two-zone (core-shell) parallel memristor model and switching characteristics. (a-b), Schematic of the core-shell representation of the current distribution, and an equivalent lumped-element circuit model of the core-shell structure, where R_m represents a memristive element that reflects the temperature-dependent conductivity of the core region and R_s is the parallel shell resistor. (c-f): Simulated current-voltage characteristics of devices under current-controlled operation showing (c), maximum negative differential resistance (d) continuous S-type NDR where the shell resistance is constant and greater than the negative differential resistance of the core, (e) discontinuous snapback NDR where the shell resistance is constant and lower than the negative differential resistance of the core, and (f) composite NDR when the shell resistance changes with current and is treated as a second memristor (inset).

have a lower current density than the core due to their relative areas. In this case the shell resistance effectively divides the total current and enables the core to respond to the positive feedback created by local Joule heating while maintaining constant total device current. The resulting increase in core conductivity is then analogous to the threshold switching response and produces the sudden reduction in voltage that characterises the snapback response in **Fig. 3.8(e)**. Importantly, this simple two-zone, core-shell model can also explain the diverse range of switching phenomena observed in oxide devices. In that case, it is necessary to consider that both the core and shell regions have temperature dependent conductivities that can be represented by two parallel memristors, one representing the high-conductivity filament, with resistance $R_{m1}(I_c)$, and the other the parallel conduction through the surrounding film, with resistance $R_{m2}(I_s)$, as shown inset of **Fig. 3.8 (f)**. The total device resistance is then expressed as: $R_{dev} = (R_{m1} \cdot R_{m2}) / (R_{m1} + R_{m2})$ where both $R_{m1}(I_c)$ and $R_{m2}(I_s)$ can be

negative within specific current ranges. Note that, as the core and shell regions represent different areas of the same oxide film, their electrical conductivity can be expected (but not necessarily) to be governed by the same physical mechanism. If this is the case where the core and shell exhibit a temperature-dependent conductivity change, then the resulting NDR characteristics will depend on the relative magnitudes and temperature dependencies of the two regions and can exhibit a wide range of compound characteristics, an example of which is illustrated in **Fig. 3.8(f)**. A detailed description of the model parameters and experimental demonstration of the model predictions are presented in the subsequent chapters.

Electroforming in Niobium Oxides: Filament detection and analysis

Memristive switching in two-terminal MOM structures are often observed after an initial electroforming step which creates a filamentary path through the oxide film and the switching response is dominated by the electroformed filament. The existence of filamentary conduction is often inferred from area-independent switching characteristics [82], but has also been verified directly by conductive atomic force microscopy (C-AFM)[238] and infrared (thermal) microscopy (IR-M)[190]. Compositional analysis of filaments has been undertaken by transmission electron microscopy (TEM) [65] but this requires pre-knowledge of the filament location and is not suitable for large-scale statistical analysis. Each of these techniques have advantages and disadvantages but only IR-M is well suited to large-scale statistical analysis of filament distributions and to the detection of transient filaments. As a consequence, there is great interest in the development of new methods for detecting and characterising conductive filaments.

In this chapter, a simple alternative technique for locating volatile or non-volatile filaments in MOM cross-point devices is introduced which is based on thermal discolouration of a thin photoresist layer deposited on the top electrode of the cross-point device. The technique relies on the increase in temperature at the top-electrode/photoresist interface produced by local Joule heating in an underlying conductive filament. The efficacy of this approach is demonstrated by applying it to understand the electroforming processes in MOM cross-point devices comprised of Pt/Nb(or Cr)/NbO_x/Pt heterostructures. Specifically, two distinct modes of electroforming in NbO_x are reported, and it is shown that the dominant mode depends on the electrical conductivity of the oxide film. This is achieved by correlating results from the developed filament detection technique, thermorefectance imaging, quasi-

static current-voltage measurements and finite element modelling.

4.1 Experiments

Pt/Nb(Cr)/NbO_x/Pt cross-point test structures, as shown schematically in **Fig. 4.1(a)**, were fabricated using standard photolithographic processing as described in **Chapter 3**. Both bottom and top electrodes were defined by a photolithographic lift-off process using negative photoresist (MaN 1420). The bottom electrode consisted of a 5 nm thick Nb (or 5 nm Ti or 10 nm Cr) wetting-layer and a 25 nm (or 40 nm) thick Pt layer deposited sequentially by e-beam evaporation on a Si (100) wafer with a 300 nm thick thermal oxide layer. Functional layers of NbO_x films with varying compositions were then deposited over the entire wafer, including the lithographically defined bottom electrode. Specifically, a 45 nm stoichiometric NbO_x (2.60 ± 0.5) layer was deposited using rf sputtering from an Nb₂O₅ target and sub-stoichiometric NbO_x films ($x=1.92 \pm 0.03$ to 2.22 ± 0.03) were deposited using dc sputtering at different pressure in Ar/O₂ ambient. Top electrodes, consisting of a 10 (or 5) nm-thick Nb (or Cr) layer and a 25 nm Pt protective layer were then deposited by e-beam evaporation. The NbO_x layer covering the bottom contact pads was then removed by reactive ion etching to provide direct electrical contact to the pad. The test-devices had electrode dimensions ranging from $2 \mu\text{m} \times 2 \mu\text{m}$ to $20 \mu\text{m} \times 20 \mu\text{m}$. As-deposited NbO_x films were analysed by grazing incident-angle X-ray diffraction (GIAXRD) and Rutherford backscattering spectroscopy (RBS) to determine their structure and composition [239]. To simplify the RBS analysis, NbO_x films were simultaneously deposited on vitreous carbon substrates. Electrical measurements were performed using an Agilent B1500A semiconductor parameter analyser attached to a Signatone probe station (S-1160). All the measurements were executed at room temperature in atmospheric conditions by applying bias on the top electrode, while the bottom electrode was grounded. Thermal imaging of devices during electroforming was performed using a TMX T^oImager®[®], a camera-based thermorefectance imaging system as described in **Chapter 3**.

4.2 Electroforming and filament detection

As fabricated devices with stoichiometric NbO_x ($x = 2.6$) were in a highly resistive state (device resistance $> 10^6 \Omega$) and required a one-step electroforming process to initiate memristive switching characteristics. This was achieved by applying a positive bias voltage swept from 0 V to + 6 V to the top electrode while limiting the maximum current through the device (compliance current, I_{CC}) to ~ 2 mA to avoid permanent damage. **Fig. 4.1(b)** shows

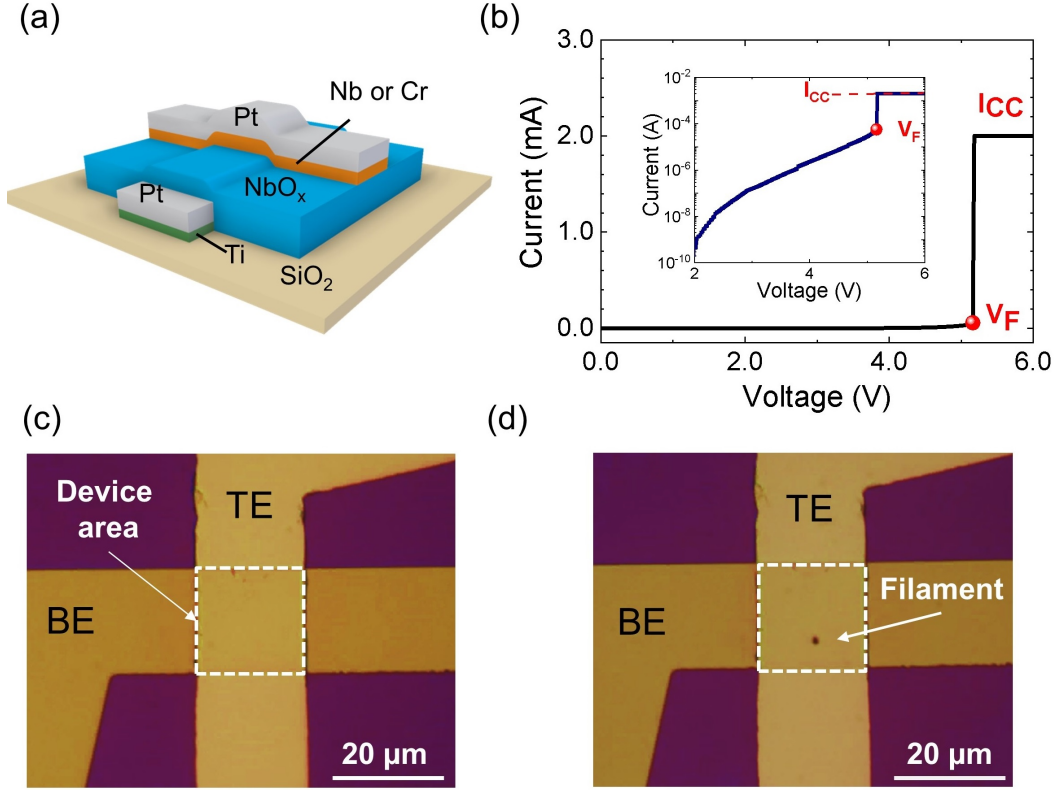


Figure 4.1: (a) A schematic of the device structure, (b) a typical current-voltage (I-V) characteristic of the electroforming process for a $20\ \mu\text{m} \times 20\ \mu\text{m}$ Pt/Cr/ NbO_x/Pt device under voltage-controlled testing. Inset is a semi-log plot of the I-V characteristic. (c-d) Optical microscope images of the same device before (c) and after (d) the electroforming process. The dark spot on the device after forming indicates the location of a conducting filament.

typical electroforming characteristics for a $20\ \mu\text{m} \times 20\ \mu\text{m}$ Pt/Cr/NbO_x/Pt device. The electroforming voltage, V_F , is defined as the point at which the current reaches the compliance limit and corresponds to an electric field of $\sim 2\ \text{MV/cm}$ for these devices, which is consistent with previous studies [82]. Following the electroforming step, the device resistance is $\sim 10\ \text{k}\Omega$, consistent with the formation of a permanent conductive filament.

The high current density associated with filamentary conduction is known to cause a rapid increase in temperature due to local Joule heating. Indeed, in-situ thermal mapping has shown that the surface temperature of the filament can increase by several hundred degrees [190]. Here this temperature increase is exploited to thermally denature a thin photoresist layer and record the location of the filament. To achieve this, the cross-point devices were coated with a thin positive photoresist (AZ 1512HS) layer and a photolithographic step used to reopen access to the device contact pads. The photoresist was then baked for 2 minutes in air using a hot plate kept at a temperature of 358 K (85 °C). **Fig. 4.1(c)** shows an image of

a $20\text{ }\mu\text{m} \times 20\text{ }\mu\text{m}$ cross-point device before electroforming and **Fig. 4.1(d)** shows an image of the same device after electroforming (forming). It is immediately evident that forming creates a dark spot in the photoresist, clearly identifying the filament location. Analysis of more than 150 devices showed that forming produced a single filament in most cases; with only a few showing multiple filaments. This is in agreement with previous results indicating the dominance of single filament switching [78, 240, 241].

4.3 Sensitivity of the filament detection technique: Finite Element Modelling

To determine the relationship between the temperature of the filament and that at the top-electrode/photoresist interface during electroforming, a finite element model of the device structure and filamentary Joule heating was constructed. This was undertaken with the COMSOL simulation environment, using the electric-current and heat-transfer modules to calculate the steady-state temperature distribution as a function of applied current. The device was represented by a 2D axisymmetric model with a device radius of $2\text{ }\mu\text{m}$ and comprised of the following material layers (bottom-to-top): SiO_2 (300 nm)/Ti (10 nm)/Pt(25 nm)/ Nb_2O_5 (45 nm)/Cr (10 nm)/Pt (25 nm)/PMMA (2000 nm). The Nb_2O_5 layer was assumed to contain a conductive filament of radius 250 nm. Conduction in the filament and the surrounding Nb_2O_5 layer was assumed to be due to Poole-Frenkel conduction, as described by equation 4.1 , with an activation energy of $E_{\text{ac}} = 0.215\text{ eV}$ [242].

$$\sigma = \sigma_0 \cdot \exp \left(- \left(E_{\text{ac}} - q \sqrt{\frac{qE}{\pi \epsilon_0 \epsilon_r}} \right) / k_B T \right) \quad (4.1)$$

The absolute conductivities of the two regions was assumed to be different, as determined by the choice of σ_0 . Here $\sigma_0 = 2 \times 10^4\text{ S/m}$ for the filament and $\sigma_0 = 1\text{ S/m}$ for the surrounding oxide layer were used, so at 293 K the conductivity of the filamentary region is $\sim 4.0\text{ S/m}$ while that of the surrounding Nb_2O_5 is $2 \times 10^{-4}\text{ S/m}$. The thermal conductivity of the filament and the surrounding Nb_2O_5 layer was assumed to be given by $k_{\text{th}} = 1.0 + L\sigma T$, where the first term is the lattice contribution and the second the electron contribution. (NB: For the temperatures considered in this study $k_{\text{th}} \sim 1.0\text{ W/(m.K)}$) [61, 168].

The physical properties of the other materials were taken from the COMSOL material library where available. Exceptions were the thermal and electrical conductivities of SiO_2 which were set to 1.3 W/(m.K) and $1 \times 10^{-10}\text{ S/m}$, respectively, and the specific heat and electrical conductivity of PMMA which were set to 1.66 J/(kg.K) and $1 \times 10^{-10}\text{ S/m}$, re-

spectively. The temperature at the top of the PMMA layer and the bottom of the SiO₂ layer were set to $T_0=293$ K, and the lateral edge of the sample was assumed to be thermally insulating. Since Si has a very high thermal conductivity compared to SiO₂ its contribution was modelled by setting the temperature at the bottom of the SiO₂ layer to $T_0 = 293$ K as a boundary condition. However, the temperature distribution at the electrode/PMMA interface was found to depend on PMMA thickness. This dependence diminished with increasing layer thickness and was negligible for layers of 1-2 μm thicknesses, which are typical of the actual layer thicknesses in experimental devices. Simulations were performed for a PMMA thickness of 2 μm .

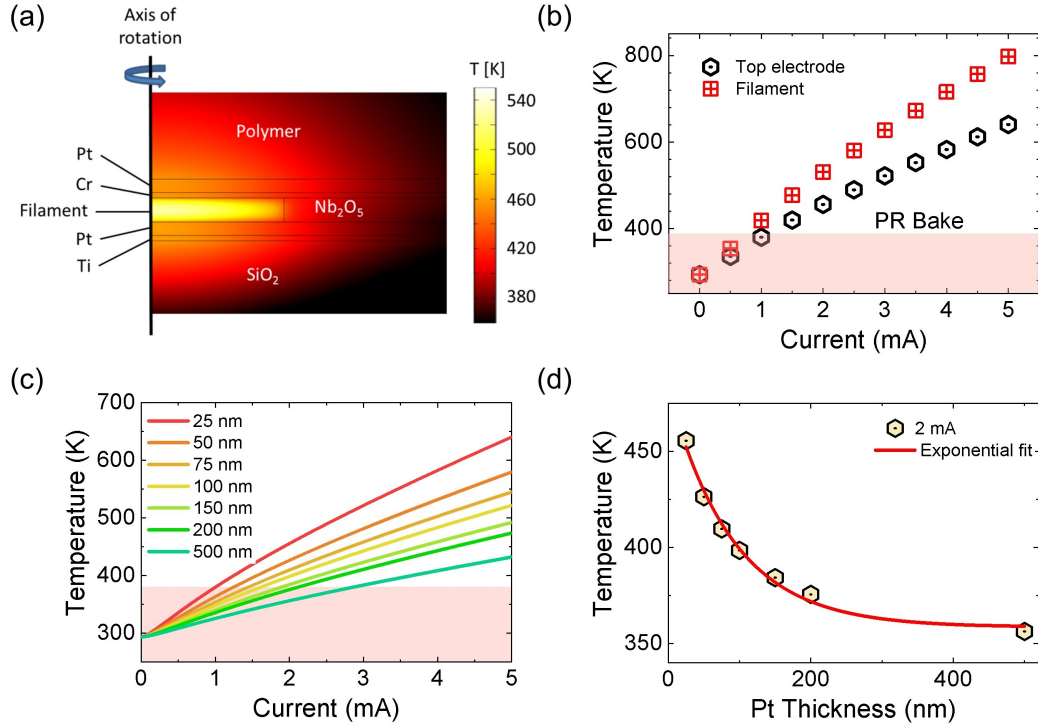


Figure 4.2: (a) Temperature distribution in the active volume of the device for a current of 2.0 mA. The depicted structure represents a cross section of an axisymmetric model with the axis of rotation shown, (b) maximum temperature in Nb₂O₅ filament compared to the maximum temperature at top-electrode/PMMA interface, (c) maximum temperature at the top-electrode/photoresist interface as a function of device current and top electrode (Pt) thickness, and (d) maximum temperature at the top-electrode/photoresist interface as a function of top electrode (Pt) thickness.

Fig. 4.2(a) shows the calculated temperature distribution in the active volume of the device for a current of 2.0 mA and clearly shows the temperature increase at the top electrode due to Joule heating of the filament in the underlying NbO_x layer. This is shown quantitatively in **Fig. 4.2(b-c)** which plot the maximum temperature at the top-

electrode/photoresist interface as a function of device current and top (Pt) electrode thickness. This shows that the temperature is a strong function of both parameters and reaches a value of 456 K for a current of 2.0 mA and electrode thickness of 25 nm, more than sufficient to modify the photoresist. However, as shown in **Fig. 4.2(d)**, the maximum temperature decreases rapidly with increasing top electrode thickness, decreasing from 456 K to 398 K as the electrode thickness increases from 25 nm to 100 nm for a device current of 2 mA. Hence, these simulations confirm that the top-electrode/photoresist interface can reach temperatures sufficient to degrade the photoresist but highlight the importance of using thin top electrodes to maximise the sensitivity of the technique. That is, filament detection would not be possible in the present case if the electrode thickness was increased significantly.

4.4 Utility of the filament detection technique

4.4.1 Influence of device geometry on the stochastic nature of forming

The utility of the proposed filament detection method is demonstrated through its use to study the influence of device structure on the stochastic nature of electroforming. To this end, the spatial distribution of the filament was recorded for 50 individual $20\ \mu\text{m} \times 20\ \mu\text{m}$ ($400\ \mu\text{m}^2$) devices using images such as those shown in **Fig. 4.1(d)**. The results are plotted in **Fig. 4.3(a)** and show that a significant fraction of the filaments form at the electrode edges. Moreover, an apparent preference for filament formation along the top-electrode edge rather than the bottom electrode edge was observed. To further investigate this point, the same analysis was performed on devices of different area (see **Fig. 4.3(b)**) and is summarised in **Fig. 4.3(c)**. This figure clearly shows that the fraction of filaments formed at the device edges is a strong function of device area, and that for smaller devices there is a trend for filament nucleation at the top-electrode edge. For the $20\ \mu\text{m} \times 20\ \mu\text{m}$ ($400\ \mu\text{m}^2$) devices 40% of filaments formed at electrode edges, with $\sim 30\%$ forming at the top electrode (TE) edges and $\sim 10\%$ at the bottom electrode (BE) edges, while for $5\ \mu\text{m} \times 5\ \mu\text{m}$ devices the edge fraction increases to 75%, with 50% at the top edge and 25% at the bottom edge. These results suggest that for small devices, the location of the conductive filament is affected by defects or inhomogeneities at the electrode edge that were introduced during device fabrication. Such effects need to be understood for a full interpretation of area-dependent scaling effects.

For example, the forming voltage, V_F , for randomly distributed filaments is expected to

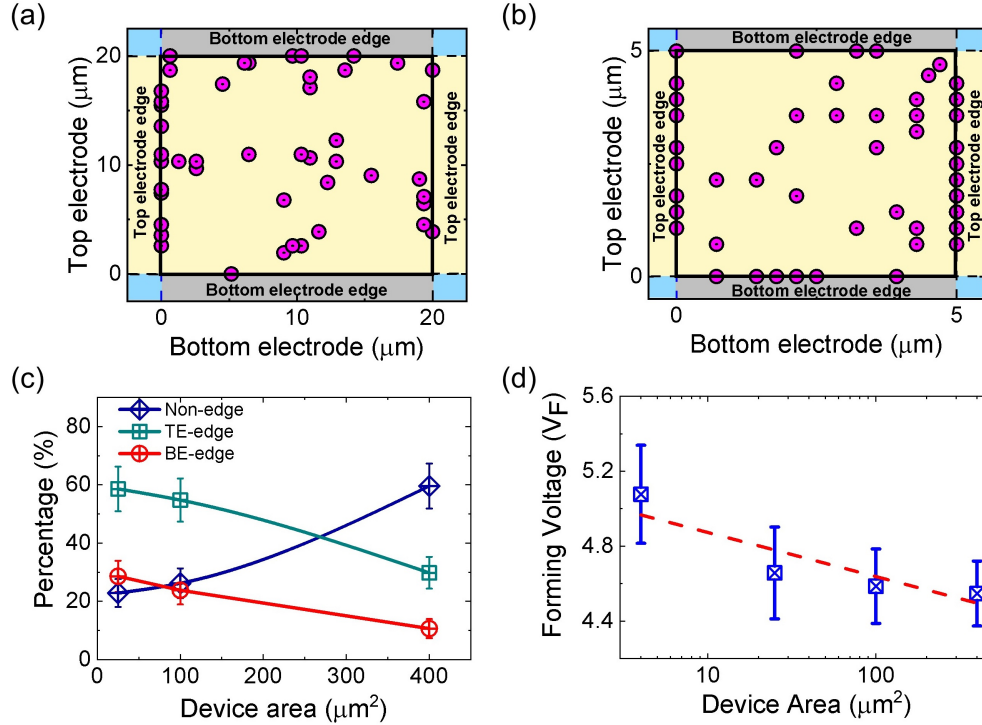


Figure 4.3: (a-b) Location of the filaments of $20\ \mu\text{m} \times 20\ \mu\text{m}$ and $5\ \mu\text{m} \times 5\ \mu\text{m}$ cross-point devices respectively (each red dot represents a filament in a single device and each map collates data for 50 different devices). The overlaid lines show the position of the electrode edges in the cross-point structure. (c) Percentage of devices formed at the edge of the cross-point as a function of device area. (d) Variation of forming voltage as a function of device area (The error bars in **Fig. 4.3 (c-d)** represent standard deviation from the mean value of the data taken from more than 20 devices in each case. The dashed line in **Fig. 4.3(d)** shows a conventional fit to the experimental data).

decrease with increasing device area and to have a dependence of the form [243, 244]:

$$V_F = C_1 - C_2 \ln \left(\frac{A}{a^3} \right) \quad (4.2)$$

where $C_{1,2}$ are constants associated with statistics of the forming process, a^3 is the characteristic material volume, and A is the device area. **Fig. 4.3(d)** shows the area dependence of forming voltage for the devices in this study, where the forming voltage and variance of the forming voltage both increase with decreasing area. For example, $4\ \mu\text{m}^2$ devices have a forming voltage of $5.1 \pm 0.3\ \text{V}$ compared with $4.6 \pm 0.2\ \text{V}$ for $400\ \mu\text{m}^2$ devices. This is most likely due to the enhanced nucleation of filaments at the electrode edges in the smaller devices.

Given that defect formation depends exponentially on the local electric field, the proba-

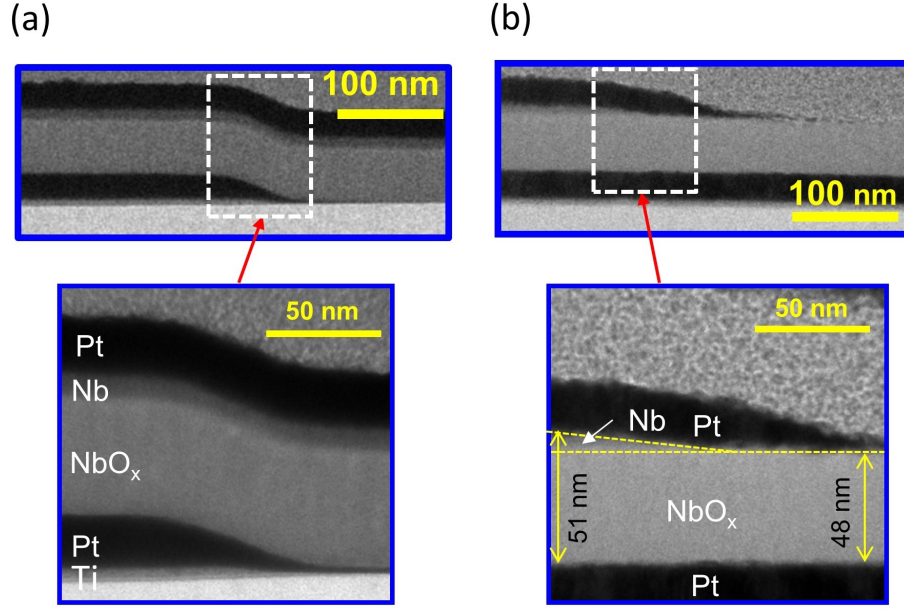


Figure 4.4: Cross-sectional TEM of a cross-point device at (a) the bottom edge, and (b) top edge.

bility of a filament forming is strongly influenced by variations in the oxide thickness, such as those that might be expected for deposition onto the non-planar bottom electrode structure [245]. In this context, preferential forming at the top electrode edge seems counter-intuitive. To better understand how this might arise, cross-sectional TEM images were taken at the top and bottom edges as shown in **Fig. 4.4**. These images show that the metal electrode layers extend beyond the nominal photolithographic mask edges and into the region where the photoresist is undercut to facilitate the lift-off process, an effect that is clearly evident in **Fig. 4.4(a)**. The extent of residual metal penetration increases with increasing metal thickness, so it is greater for the Pt layer than for either the Ti at the bottom electrode or Nb(or Cr) at the top electrode. As such, a region is observed at the edge of the electrodes where Pt is in direct contact with the NbO_x layer, as shown in **Fig. 4.4(b)**. This is significant because the top Nb (or Cr) layer is expected to react with the NbO_x to extend the effective oxide thickness. The oxide layer is therefore thinner at the top-electrode edge where it is in direct contact with Pt, possibly explaining why the majority of filaments form in this region.

4.4.2 Distinct modes of electroforming depending on oxide stoichiometry

To highlight a significant use of the filament detection technique, current-controlled electroforming characteristics of 5 μm devices fabricated with low ($x = 2.60$) and high ($x =$

1.92) conductivity NbO_x films were compared. The relationship between stoichiometry and resistivity is shown in **Fig. 4.5**.

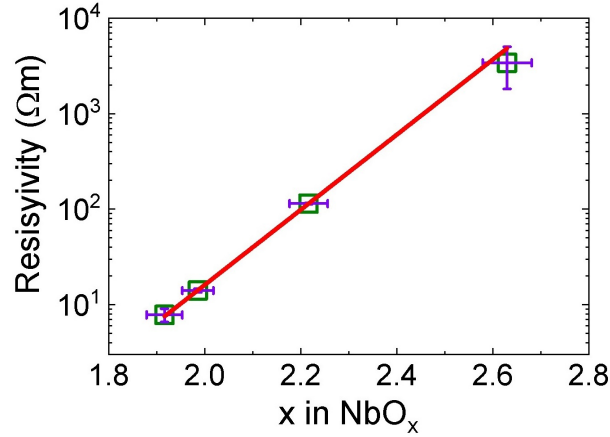


Figure 4.5: Resistivity of the NbO_x film as a function of stoichiometry (x). These data were extracted from the resistance of the as-fabricated devices measured at a low bias voltage.

Figs. 4.6(a-b) show examples of I-V characteristics of electroforming, where devices fabricated from both high and low resistivity films exhibit abrupt voltage changes during the forward current sweep. After electroforming all devices show local discolouration of the photoresist layer, clearly demonstrating filamentary conduction. However, the reverse current sweeps (the blue lines in **Figs. 4.6(a)** and **4.6(b)**) reveal distinctly different behaviour, with the low-conductivity film exhibiting S-type negative differential resistance (NDR) and a permanent change in low-field resistance from several $\text{M}\Omega$ to $\sim 10 \text{ k}\Omega$. In contrast, the high-conductivity film exhibits an abrupt ‘snapback’ characteristic with no significant change in resistance. Subsequent current sweeps reproduced the S-type NDR characteristics of the low-conductivity films and the snapback response of the high-conductivity films in both forward and reverse sweeps. The post-forming characteristics will be discussed in the subsequent chapters.

The corresponding filament distributions for these films are shown in **Figs. 4.6(c)** and **4.6(d)**, where each point represents the location of a single filament measured in a separate device. Comparing these figures reveals a dramatic difference in the filament distributions. For the low conductivity films, a significant fraction ($\sim 80\%$) of filaments form at the electrode edges and those within the film are randomly distributed. These observations are consistent with a field-induced, weakest-link model of electroforming based on the drift and diffusion of oxygen vacancies, as illustrated schematically in **Fig. 4.6(e)** [198]. Within this framework, the concentration of filaments at the electrode edges reflects variations in the film thickness and local electric field in this region as discussed earlier. In contrast, the filament distribution

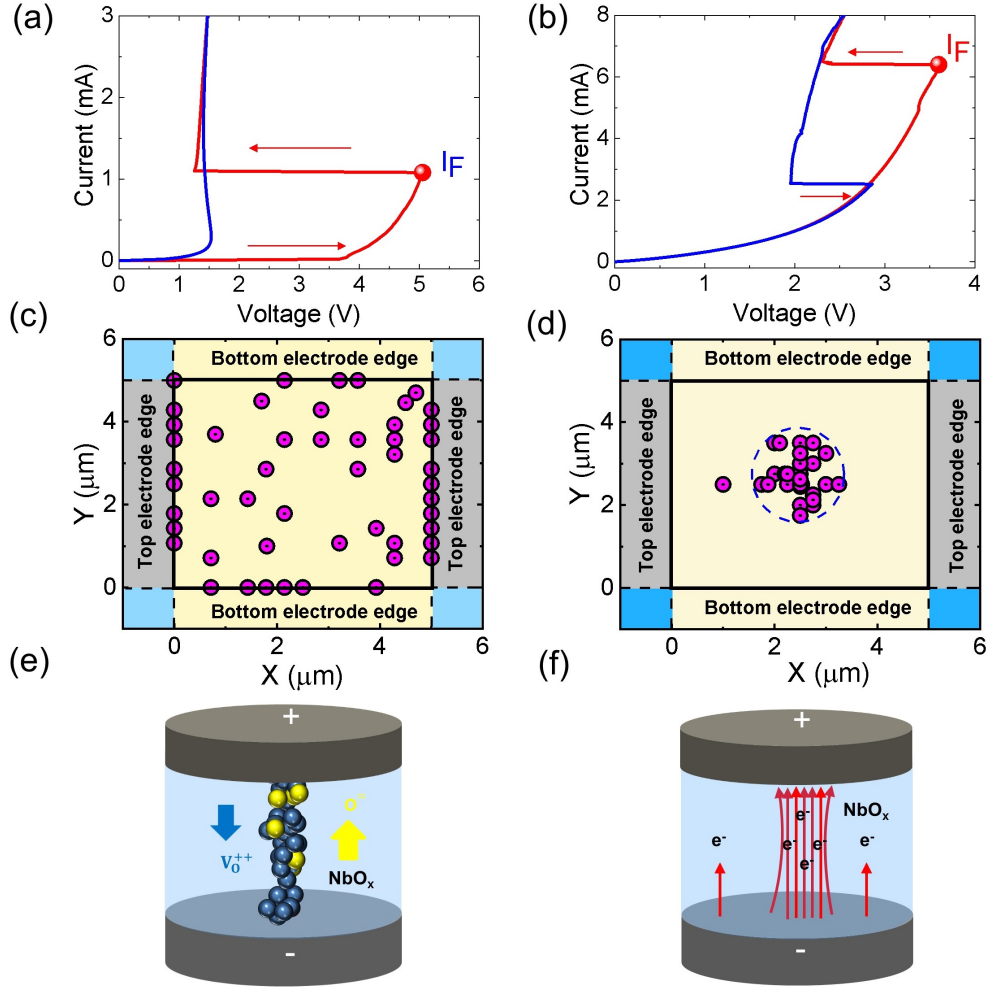


Figure 4.6: Electroforming and filament distributions in $5 \mu\text{m} \times 5 \mu\text{m}$, Pt/Nb/NbO_x/Pt cross-point devices: (a) Electroforming characteristic of a NbO_x ($x = 2.6$) device, (b) electroforming characteristic of a NbO_x ($x = 1.92$) device, (c) filament distribution in low-conductivity, NbO_x ($x = 2.6$) devices, (d) filament distribution in high-conductivity, NbO_x ($x = 1.92$) devices, (e) schematic of oxygen vacancy filament formed by field-induced generation, drift and diffusion of oxygen vacancies, and (f) schematic of a transient current filament due to current bifurcation. Note that each point in (c-d) represents a single device and the filament distributions represent 75 separate measurements for each film.

in the high-conductivity films is localised around the centre of the film and no filaments are detected at the electrode edges, even though the electrode geometry is similar to that for the low-conductivity films. However, it is noted that the filament distribution in these high-conductivity films is very sensitive to the uniformity of the oxide film and the roughness of the bottom electrode. As shown below, this type of filament distribution is consistent with the formation of a transient conductive filament, such as that illustrated in **Fig. 4.6(f)**.

4.5 Electroforming in sub-stoichiometric NbO_x and in-situ temperature mapping

To further investigate the electroforming process in high-conductivity sub-stoichiometric NbO_x films, an in-situ temperature map was obtained during the initial electroforming step using a current sweep. The in-situ thermorefectance measurements in **Fig. 4.7** compare I-V characteristics and temperature distributions of a 10 $\mu\text{m} \times 10 \mu\text{m}$ device with a high-conductivity NbO_x ($x = 1.99$) film during electroforming. The in-situ I-V characteristics show a snapback response at a threshold current of $\sim 5.9 \text{ mA}$, consistent with the results reported in **Fig. 4.6(b)** for NbO_x ($x = 1.92$). For currents below this forming threshold the temperature increases monotonically with current and has a broad distribution that reflects the boundary conditions imposed by the device geometry. However, at the onset of forming the distribution narrows abruptly and the maximum temperature increases by $\sim 200 \text{ K}$. This produces a local hot spot with a FWHM of $\sim 1.5 \mu\text{m}$ and is accompanied by a $\sim 50 \text{ K}$ temperature reduction in the region surrounding the filament, consistent with the redistribution of current from regions of low to high current density. This is exemplified by **Fig. 4.7 (c)** at a position of 2 μm and 9 μm where temperature decreases as device current increases. These results clearly demonstrate the correlation between the abrupt voltage change and current bifurcation in high conductivity films.

Significantly, the electroforming processes led to permanent filamentary paths through the oxide films irrespective of their composition. An example of a filamentary core of approximately 300 nm diameter is shown inset of **Fig. 4.7(c)**, which illustrates a back-scattered electron image of the oxide (high conductivity film) surface after removing the top electrode by chemical etching. Interestingly, this image also reveal that the core is immediately surrounded by a region of lower average atomic number, consistent with the formation of an oxygen rich halo around a central conductive core as reported by others [197, 246].

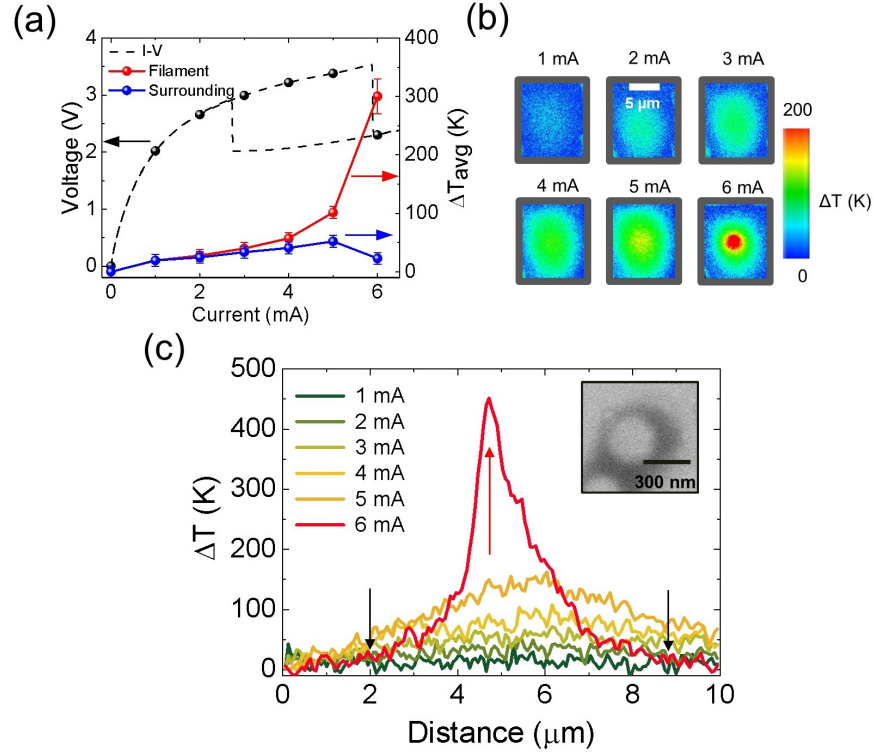


Figure 4.7: In-situ thermoreflectance measurements: (a) in-situ (points) and ex-situ (line) current-voltage characteristics of a $10\ \mu\text{m} \times 10\ \mu\text{m}$ cross-point device with a high-conductivity NbO_x ($x = 1.99$) film, and the temperature of the film in the filamentary (red) and surrounding regions (blue), (b) 2D temperature maps of the top electrode surface for different device currents, and (c) temperature profile through the filamentary region for different device currents. Inset of Fig. 4.7 (c) shows a back-scattered electron image of the filamentary region in the oxide film after removing the top electrode.

4.6 Finite Element Modelling

A finite-element model of the bifurcation process was used to provide a comparison with the experimental data in **Figs. 4.6** and **4.7** and support the above interpretation of the electroforming process in sub-stoichiometric NbO_x . Finite element modelling was performed with the COMSOL package. The model was based on a two-dimensional axisymmetric model of a $\text{Pt}/\text{NbO}_x/\text{Pt}/\text{SiO}_2$ device, as shown in **Fig. 4.8**. The current-voltage characteristics and associated current and temperature distributions were then calculated by self-consistently solving the heat transfer and current continuity equations, including the effect of Joule heating. The boundary conditions allowed radiative energy loss from the top surface of the device with an emissivity of 0.02, and fixed the temperature of the device perimeter and the bottom of the SiO_2 layer at 293 K, as indicated in **Fig. 4.8**. Simulations were performed as a function of device current with current applied to the top Pt electrode and the bottom Pt

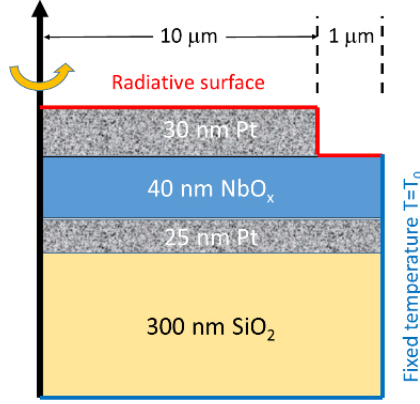


Figure 4.8: Schematic of the axisymmetric device structure employed for finite element simulations including boundary conditions.

electrode serving as the electrical ground. Material properties of Pt and SiO_2 were taken from COMSOL material library. The electrical conductivity of the NbO_x layer was assumed to be governed by Poole-Frenkel conduction, as defined by Equation 4.1. Relevant NbO_x parameters are given in **Table 4.1**.

Table 4.1: Properties of NbO_x layer used in the simulation.

NbO_x Properties	Values	Unit	Ref.
Thermal conductivity	1.0	$\text{W}/(\text{m.K})$	[247]
Activation energy (E_{ac})	0.45	eV	[228, 229]
σ_0	100000	S/m	
ϵ_r	45		[229]

Selected results from the simulations are summarised in **Fig. 4.9**, which gives important insight into the nature of filamentary conduction. Specifically, the simulation reproduces the snapback characteristics observed in **Fig. 4.7(a)** without imposing material specific properties or inhomogeneity. Furthermore, the simulation predicts the formation of high current density ‘filaments’ at the centre of the device structure, consistent with the filament distribution reported in **Fig. 4.6(d)**. This is the result of current redistribution from regions of low to high current density and produces a corresponding change in the temperature of the filament and surrounding film as observed experimentally in **Fig. 4.7**. This observation of current bifurcation under current-controlled testing is consistent with experimental observations in TaO_x and the simulation results of Goodwill et al. [79] who also reported a current constriction process.

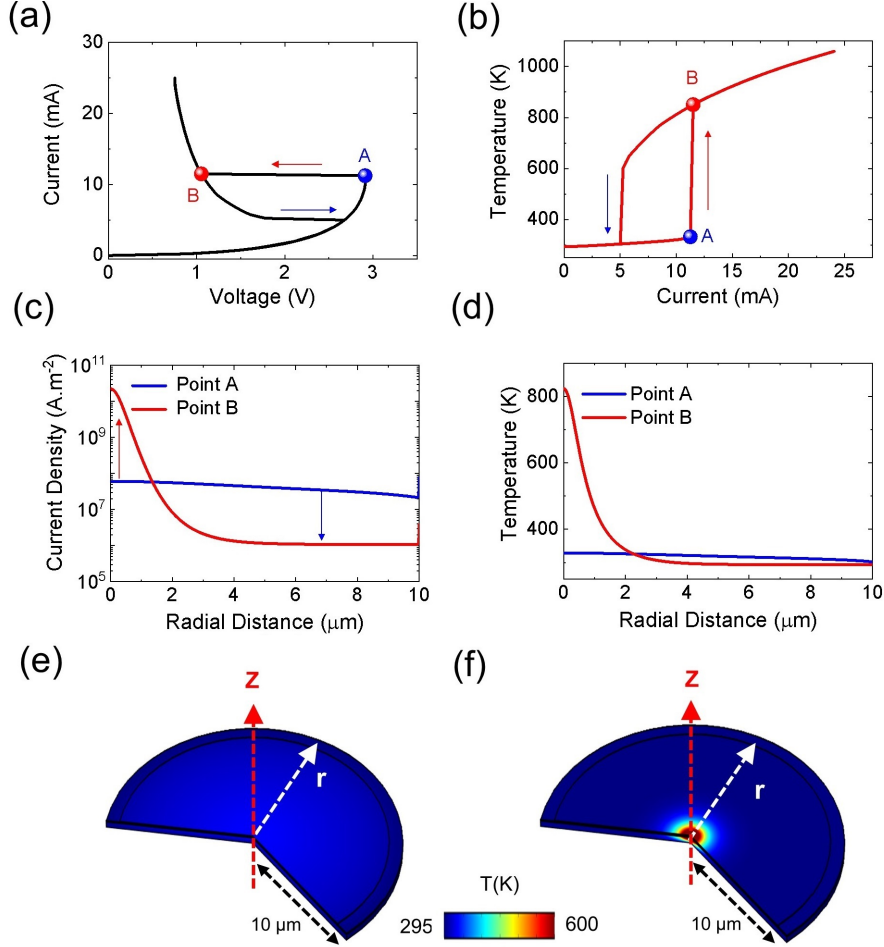


Figure 4.9: Finite element simulation: (a) current-voltage characteristics during bidirectional current sweep, (b) maximum temperature in oxide film as a function of device current, (c) current density distribution before and after bifurcation, (d) temperature distribution before and after bifurcation, and (e-f) 3D temperature distribution: (e) before (point A) and (f) after current bifurcation (point B).

4.7 Summary

In summary, the electroforming process in MOM cross-point devices using niobium oxide thin films with varied compositions have been studied. At first, a simple technique to detect and spatially map volatile and non-volatile conductive filaments in micron-scale MOM cross-point devices was introduced, which is based on a thermal discolouration of a thin photoresist layer. Finite element modelling showed that the temperature of the top-electrode/photoresist interface can easily exceed that required to discolour photoresist but that the maximum temperature is a strong function of top electrode thickness. The application of this technique to metal-oxide-metal cross-point devices confirmed that electroforming generally created one

dominant filament and showed that for stoichiometric NbO_x films filament formation was heterogeneous, with filaments preferentially forming along the edge of the top electrode. TEM analysis of the top and bottom electrode edges suggested that this was due to a reduction of the effective oxide thickness in this region.

Importantly, by further applying this technique for devices with NbO_x thin films with variable composition, two distinct electroforming modes were identified and classified as field-induced or thermally induced based on their characteristics and dependencies. This was achieved by using quasi-static I-V characteristics, filament mapping, thermorefectance imaging and finite element modelling. In particular, field induced electroforming was observed in low-conductivity films and was characterised by a random distribution of filaments within the oxide film and heterogeneity due to material and device inhomogeneity. In contrast, thermally induced electroforming was observed in high-conductivity films and was characterised by a highly localised filament distribution at the centre of the film, corresponding to the region of peak temperature. This was mediated by a current bifurcation process in which the current distribution separated into regions of low and high current density and produced a highly localised temperature distribution in the film. Significantly, current bifurcation produced a sudden drop in voltage under current-controlled testing due to the increase in film conductivity caused by local Joule heating which further led to a permanent filamentary path through the oxide film as evident from back-scattered electron imaging of the oxide surface after removing the top electrode by chemical etching.

Threshold Switching Reliability: Role of metal/oxide interface reactions

Different types of memristive switching, including volatile and non-volatile behaviour, as well as combinations of these responses are observed in two terminal MOM devices based on niobium oxide thin films. Recent studies have shown that threshold switching reliability in Nb_2O_5 -based devices can be improved by introducing a reactive metal (e.g. Nb) as one of the electrodes. The devices were found to exhibit reliable threshold switching after an initial electroforming step, and had threshold and hold voltages that were independent of film thickness and device area [48, 82]. On this basis it was concluded that the active switching volume was localised, likely in the vicinity of the reactive-electrode/oxide interface [48, 82]. As such the switching characteristics are expected to be sensitive to interface reactions and field induced oxygen exchange between the electrode and oxide.

In this chapter the influence of different top electrode metals on the threshold switching response of amorphous Nb_2O_5 films is examined, and it is shown that the choice of metal does indeed play an important role in determining the switching characteristics.

5.1 Experiments

Cross-point test structures were fabricated using a step-by-step lithography process as described in **Chapter 3**. The bottom electrode consisted of a 5 nm Ti adhesion layer and a 25 nm Pt layer deposited by electron-beam evaporation onto a thermally oxidised Si substrate (oxide thickness ~ 200 nm) without breaking vacuum. A functional layer of amorphous NbO_x with ~ 45 nm thickness was subsequently deposited by rf-sputtering from a Nb_2O_5 target in an Ar ambient at a working pressure of 4 mTorr at ~ 180 W. To complete the MOM

structure a 10 nm top electrode comprising one of five different metals (Nb, Ti, Cr, Ta and Hf) was deposited on the NbO_x film followed by the deposition of a 25 nm Pt capping layer. In order to compare the role of the reactive electrodes, a set of devices with a 25 nm Pt top electrode (i.e. without the reactive metal layer) was also fabricated. The stoichiometry of the as-deposited NbO_x film was found to be near Nb_2O_5 ($x = 2.6 \pm 0.05$, i.e. slightly over-stoichiometric) as determined by RBS, and to be amorphous as confirmed by GIAXRD and TEM. Layer thicknesses and compositions were confirmed by TEM and Energy Dispersive X-ray (EDX) maps using a JEOL 2100, as shown in **Fig. 5.1** for devices with Nb and Cr TEs. Electrical measurements were performed in atmospheric conditions using an Agilent B1500A semiconductor parameter analyser attached to a Signatone probe station.

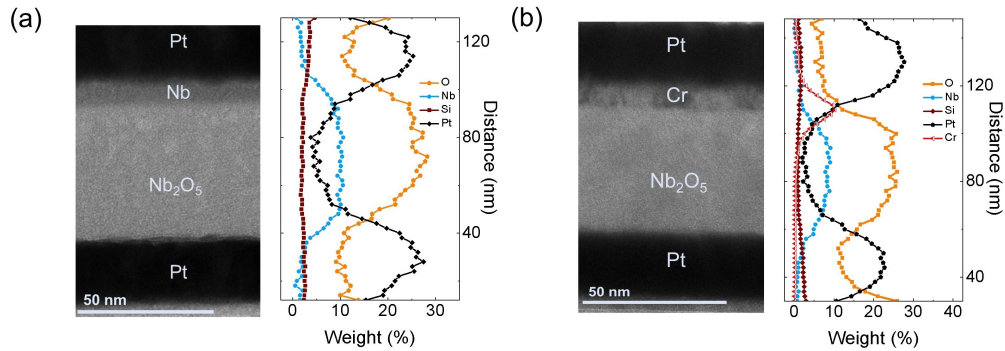


Figure 5.1: Cross-sectional transmission electron micrographs of the device structures: (a) Pt/Nb/ NbO_x /Pt, and (b) Pt/Cr/ NbO_x /Pt. Corresponding EDX maps are shown on the right of each image and were obtained from the line scan through the thickness of the device.

5.2 Current-controlled NDR characteristics

As-fabricated devices were highly insulating (device resistance $\sim \text{G}\Omega$) and were subjected to an electroforming process to initiate memristive switching (**Fig. 5.2 (a)**). The switching characteristics were initially investigated using current sweeps from 0 to -2.5 mA and a region of negative differential resistance (NDR) was evident in the immediate post-forming current-voltage (I-V) sweep for all devices (i.e. for all five top electrode metals). They also exhibited a volatile threshold switching response when subjected to voltage-controlled operation, with typical examples of NDR (solid black line) and threshold switching (red dashed line) shown in **Fig. 5.2 (b)**. Threshold and hold voltages were extracted from the current-controlled NDR characteristics and were found to have mean values of -2.2 ± 0.25 V and -1.6 ± 0.3 V, respectively, and were almost independent of the top electrode metals as shown in **Fig. 5.2(c)**.

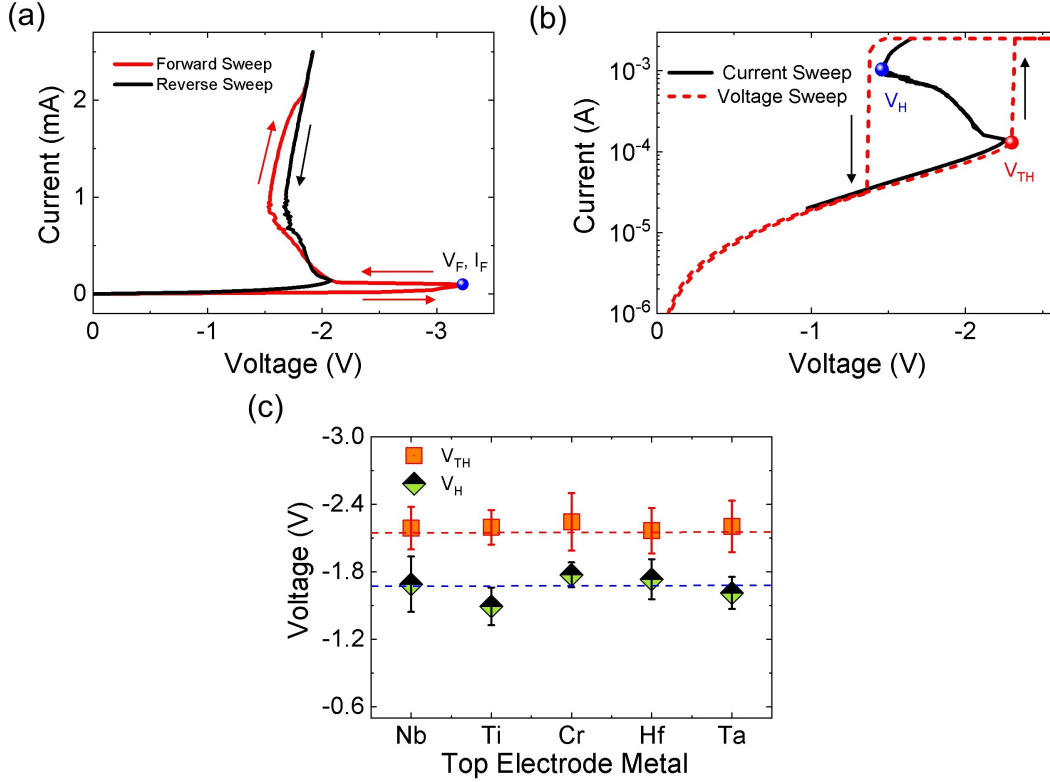


Figure 5.2: (a) A typical electroforming step under current-controlled testing, (b) negative differential resistance (NDR) characteristic observed under current-controlled mode (black solid line) and volatile threshold switching (red dashed line) under voltage-controlled operation in a typical device with Nb top electrode, and (c) threshold- and hold-voltages as a function of electrode material extracted from the corresponding NDR response (data were taken for 8 devices for each electrode metal).

These results are consistent with earlier studies [82, 248] that highlight that independent of top electrode material, the electroforming process introduced a conductive filament in the Nb_2O_5 film and a localised threshold switching volume was self-assembled at one of the electrode/oxide interfaces [61, 82, 83].

5.3 Voltage-controlled switching characteristics

The switching response was further studied using bidirectional voltage-controlled I-V sweeps from 0 V to -3 V and then from 0 V to +3 V. Stable threshold switching was observed only for devices with Nb, Ti and Cr top electrodes as shown in **Fig. 5.3**. The trap level energy, E_{ac} , was determined from temperature dependent I-V measurements using an Arrhenius plot of the low field resistance (measured at 0.5 V), as shown in **Fig. 5.4**. The calculated trap

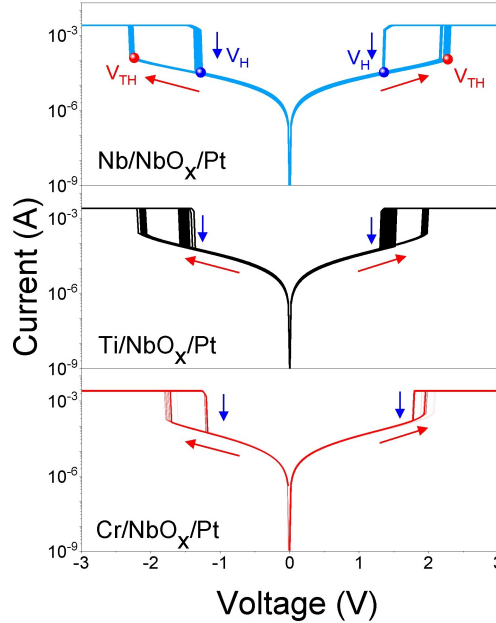


Figure 5.3: Voltage-controlled threshold switching in typical devices with Nb, Ti and Cr top electrodes respectively (from top to bottom) (20 consecutive switching cycles are shown for each case). Note that Nb and Ti top electrode devices exhibited symmetric threshold switching, while the Cr-top electrode devices exhibited asymmetric threshold switching.

level energy (i.e., $\sim 0.2 \pm 0.02$ eV) is consistent with previous reports [82, 249].

On the other hand, devices with Ta and Hf top electrodes exhibited an integrated selector-memory (1S1M) response after a few initial threshold switching cycles as shown in **Fig. 5.5**. In this case, the switching response is derived from the contributions of the memory filament and the filamentary threshold switching volume which is self-assembled at the reactive-electrode/oxide interface [82, 83].

5.4 Role of Metal/Oxide reactions on the switching response

Recent studies have shown that metal electrodes can react with an underlying oxide layer to form a metal-oxide interlayer [202, 214]. The extent of the reaction depends on the relative thicknesses of the layers, as well as the choice of electrode metal [214]. Such interaction can alter the switching behaviour, as demonstrated in **Figs. 5.3** and **5.5**. In order to understand such behaviour, possible reactions at the top electrode/oxide interface were calculated by using thermodynamic data for the stable crystalline oxide phases [84, 250, 251]. Specifically, the change of Gibbs potential, ΔG was considered, and calculated using the relation [250]:

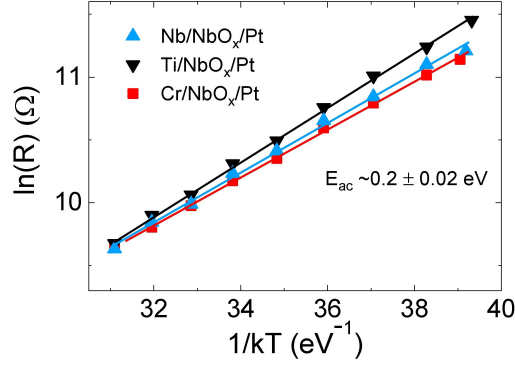


Figure 5.4: Temperature dependent change of resistance calculated at -0.5 V for electroformed devices with Nb, Ti and Cr top electrodes.

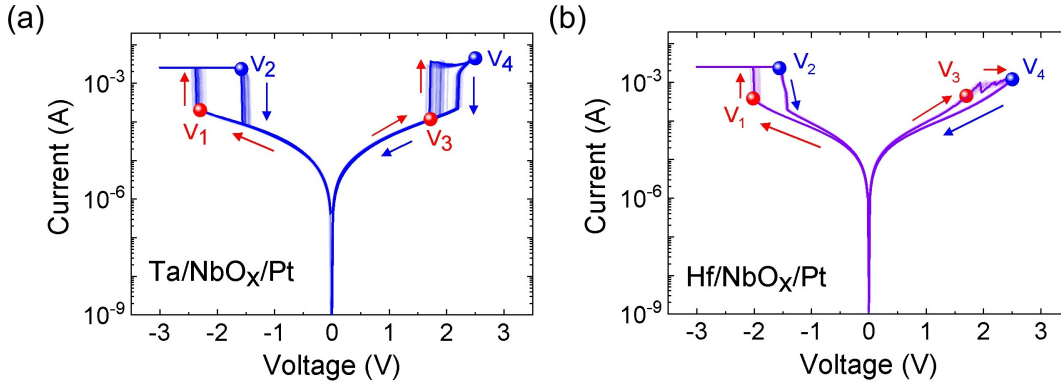


Figure 5.5: 1S1M behaviour observed under voltage-controlled mode in typical devices with (a) Pt/Ta/NbO_x/Pt and (b) Pt/Hf/NbO_x/Pt structures respectively (20 consecutive switching cycles are shown for each case).

$$\Delta G = x_2 \cdot \Delta G_2 - x_1 \cdot \Delta G_1 \quad (5.1)$$

Where, ΔG_1 and ΔG_2 are the standard isobaric potentials of formation of the oxides, and x_1 and x_2 are the number of moles of the oxides which take part in the reaction. From a thermodynamic standpoint, a negative value of ΔG is associated with a spontaneous reaction and suggests that the metal electrode will react to form an oxide layer and reduce the oxygen content of the Nb₂O₅ layer. The calculations summarised in **Table 5.1** confirm that this is indeed the case for all five reactive metals used in this study.

This analysis suggests that an oxide interlayer is likely formed by the reactive metal electrode at the top electrode/NbO_x interface. Moreover, this process is expected to be enhanced during the electroforming step due to local Joule heating [83]. For example, the

Table 5.1: Summary of the MOM stacks with different top electrodes, their thermodynamic stability and switching characteristics. Thermochemical data for different oxides were extracted from Ref. [252].

MOM Combination	Thermodynamic stability of the top electrode metal/ Nb_2O_5 interface	Stable I-V response
Pt- Nb_2O_5 -Pt	$5\text{Pt} + 2\text{Nb}_2\text{O}_5 = 5\text{PtO}_2 + 4\text{Nb}$; $\Delta G = +873.253 \text{ kJ/mol}$	Non-polar Memory/ unstable 1S1M
Nb- Nb_2O_5 -Pt	$\text{Nb} + 2\text{Nb}_2\text{O}_5 = 5\text{NbO}_2 + 4\text{Nb}$; $\Delta G = -164.265 \text{ kJ/mol}$	Symmetric TS
Ti- Nb_2O_5 -Pt	$5\text{Ti} + 2\text{Nb}_2\text{O}_5 = 5\text{TiO}_2 + 4\text{Nb}$; $\Delta G = -183.062 \text{ kJ/mol}$	Symmetric TS
Cr- Nb_2O_5 -Pt	$2\text{Cr} + \text{Nb}_2\text{O}_5 = \text{Cr}_2\text{O}_3 + 2\text{NbO}$; $\Delta G = -38.0455 \text{ kJ/mol}$	Asymmetric TS
Ta- Nb_2O_5 -Pt	$2\text{Ta} + \text{Nb}_2\text{O}_5 = \text{Ta}_2\text{O}_5 + 2\text{Nb}$; $\Delta G = -72.5655 \text{ kJ/mol}$	1S1M
Hf- Nb_2O_5 -Pt	$5\text{Hf} + 2\text{Nb}_2\text{O}_5 = 5\text{HfO}_2 + 4\text{Nb}$; $\Delta G = -381.936 \text{ kJ/mol}$	1S1M

Gibbs free energy of formation of HfO_2 is -381 kJ/mole at room temperature (see **Table-5.1**). As such the formation an interlayer is expected at the Hf/ NbO_x interface. Since HfO_2 is an insulating oxide with a high dielectric constant [253, 254], formation of such an interlayer can significantly influence the device characteristics. The resistivity of this interlayer will depend on its thickness and stoichiometry [255, 256]. Therefore, any change in these parameters due to local ion migration will also significantly influence both the device resistance and its response to the applied electric field.

Based on these arguments, the observation of two distinct resistive switching modes (shown in **Figs. 5.3** and **5.5**) can be understood in terms of reactions occurring at the top electrode/ NbO_x interface. Since a memory filament is present in both cases, the different threshold switching behaviours can be explained by assuming a stable memory filament, while the 1S1M response can be attributed to reconstruction and rupture of the conductive filament by electric field driven oxygen exchange at the top electrode/ NbO_x interface.

5.5 Modelling of the observed switching phenomena

A schematic of the proposed switching elements in a device with Hf top electrode is illustrated in **Fig. 5.6**. Here it is assumed that a thin interlayer is formed by a spontaneous reaction between the Hf top electrode and Nb_2O_5 layer, and that this is further enhanced in the vicinity of the filament due to local Joule heating during electroforming. The HfO_x layer then acts

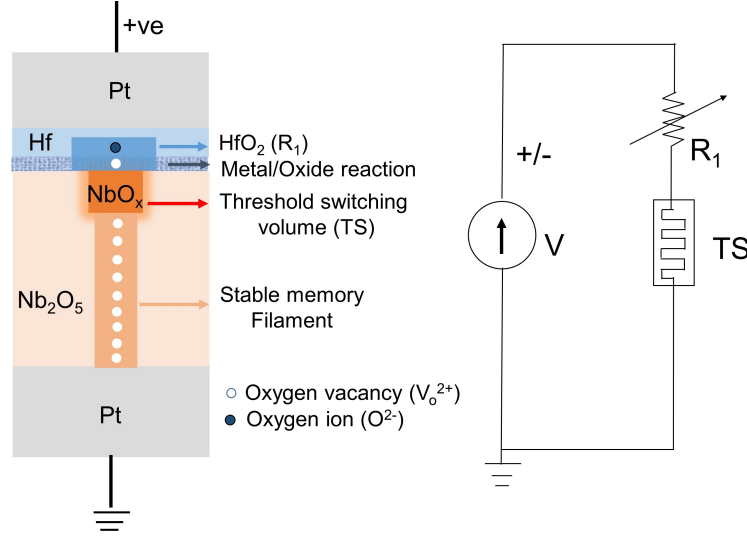


Figure 5.6: Schematic of the switching elements in a Pt/Hf/Nb₂O₅/Pt device after electroforming (left) and a corresponding circuit representation (right). The value of R_1 varies under positive and negative bias conditions due to field driven oxygen transport at the top electrode/oxide interface resulting in the rupture or reconstruction of the memory filament.

as a resistive switching layer between the electroformed filament and the top electrode. That is, when a negative bias is applied to the top electrode oxygen ions drift from the HfO_x layer into the NbO_x layer to ‘set’ the HfO_x layer into a conductive state. Under positive bias the oxygen-ions are attracted back into the HfO_x layer to ‘reset’ the device into a more resistive state. This phenomenon combined with the threshold switching response then accounts for the observed 1S1M switching behaviour. Note that it has been assumed that the threshold switching response is dominated by Joule heating of a local volume of material, as previously demonstrated [82].

While this model suggests that 1S1M behaviour might be expected for all reactive electrodes, the resistive switching response will depend on the conductivity of the interlayer, with more resistive, higher stoichiometry films expected to exhibit the most significant memory switching. The data in **Figs. 5.3** and **5.5** can then be understood from the fact that Hf and Ta electrodes are likely to lead to highly insulating oxides (e.g. HfO₂ and Ta₂O₅) [255, 256], while Cr, Nb and Ti are more likely to form semiconducting films (e.g. Cr₂O₃ [257], NbO₂ [258] and TiO₂ [259]). Note that the resistance of the interlayer will also depend on its thickness in addition to its conductivity.

Further evidence supporting this explanation may be taken from the threshold switching behaviour of the Cr-TE devices which have different hysteresis windows (V_{TH} - V_H) for forward and reverse bias, as shown in **Fig. 5.3**. This polarity dependent response indicates that the interlayer resistance is modified by biasing, but the change is not enough to initiate resistive

switching.

This particular behaviour was quantitatively investigated using a simple model of the threshold switching volume [152]. An archetype threshold switch (memristor) was considered in which the electrical conductivity was assumed to be of Poole-Frenkel type, such that the device resistance is given by [229]:

$$R_m = R_0 \cdot \exp \left(\left(E_{ac} - q \sqrt{\frac{qE}{\pi \epsilon_0 \epsilon_r}} \right) / k_B T \right) \quad (5.2)$$

where k_B is the Boltzmann constant, E_{ac} is the activation energy, ϵ_0 is the vacuum permittivity, and ϵ_r is the relative permittivity of the threshold switching volume. R_0 is the resistance pre-factor of the active region at $T = T_{amb}$.

The dynamic behaviour of the memristor is defined by Newton's law of cooling:

$$\frac{dT_m}{dt} = \frac{(I_m)^2 R_m}{C_{th}} - \frac{\Delta T}{R_{th} C_{th}} \quad (5.3)$$

where R_{th} and C_{th} are the thermal resistance and the thermal capacitance of the device, and ΔT is the temperature difference between the T_m and T_{amb} . Here, T_m and T_{amb} denote the temperature of the electrically active region and the ambient environment, respectively

Details of the model parameters are given in the **Table 5.2**.

Table 5.2: Memristor parameters used in the simulation for the Poole-Frenkel model.

Model Parameters	Symbol	Values	Unit
Thermal capacitance	C_{th}	1×10^{-15}	JK ⁻¹
Resistance pre-factor	R_0	105	Ω
Thermal resistance	R_{th}	1×10^5	KW ⁻¹
Ambient temperature	T_{amb}	298	K
Series resistance	R_1	50-500	Ω
Activation Energy	E_{ac}	0.23	eV
Relative permittivity	ϵ_r	45	
Film thickness	t	45	nm

In the application of this model, it was observed that the threshold switching window (hysteresis) is highly sensitive to any additional series resistance (R_1), where a small increase in R_1 reduces the window (**Fig. 5.7(a)**). This is similar to that observed for Cr-TE devices under positive bias in **Fig. 5.3**. Consequently, the corresponding NDR window will also narrow as shown in **Fig. 5.7(b)**.

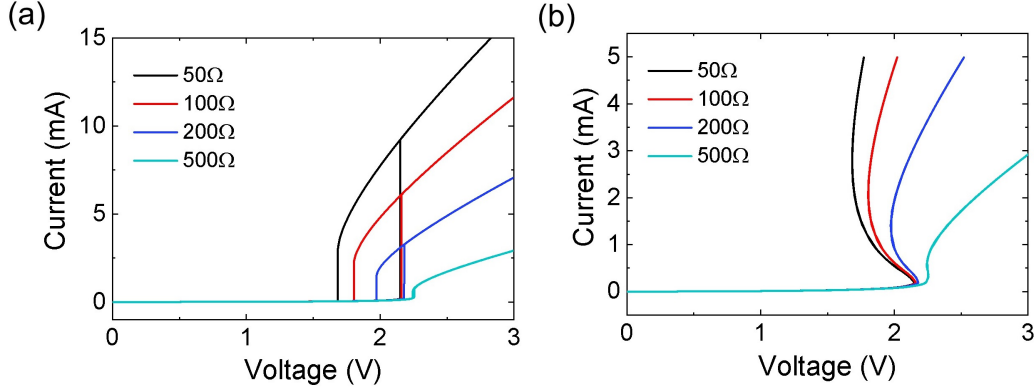


Figure 5.7: Effect of series resistance on the (a) threshold switching hysteresis and, (b) negative differential resistance window.

5.6 Switching in Pt/Nb₂O₅/Pt structures

The switching response of a Pt/Nb₂O₅/Pt structure was also measured for comparison (**Fig. 5.8**). In this case the devices underwent a few unstable threshold switching or 1S1M cy-

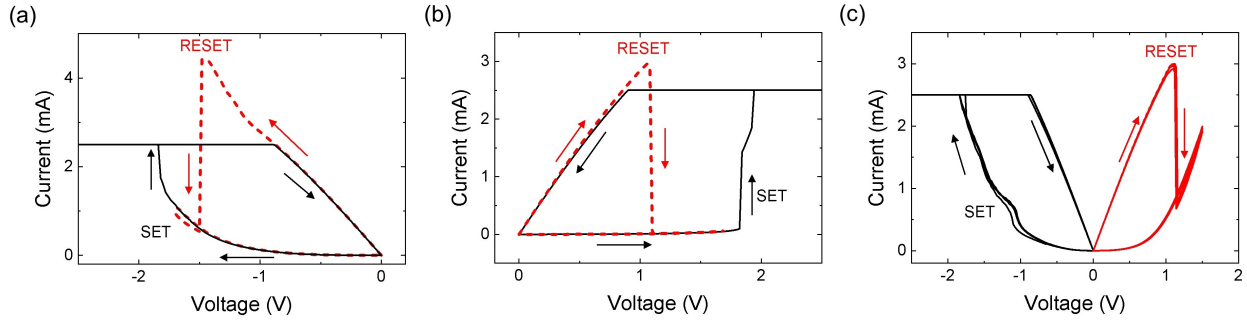


Figure 5.8: Unipolar/non-polar switching in a representative 5 μm × 5 μm cross point device with Pt/Nb₂O₅/Pt structure : (a) SET-RESET observed under negative bias, (b) SET-RESET observed under positive bias, and (c) SET-RESET observed under opposite bias polarity (negative polarity SET and positive polarity RESET).

cles before exhibiting unipolar/non-polar switching. The Gibbs free energy of formation of platinum oxide is positive, with a value $\Delta G = +873$ kJ/mol. Therefore no spontaneous reaction is expected at the Pt/Nb₂O₅ interface. However, this does not rule out some oxygen exchange during the electroforming process, which may account for the initial transient switching response. In this context it is also interesting to note that threshold switching has been observed in Pt/NbO_x/Pt ($x < 2.5$) and Pt/NbO₂/Pt structures [174, 219]. Regardless, the difference between the response of devices with Pt and reactive-metal electrodes clearly demonstrates the significance of interface reactions in controlling the threshold switching

response of Nb₂O₅-based devices.

5.7 Summary

In this chapter, the role of metal/oxide interface reactions on the threshold switching response of metal/Nb₂O₅/Pt structures has been examined. In particular, reactive metals were found to improve the threshold switching reliability but exhibited characteristic behaviour that was dependent on the nature of the interlayer formed by reaction with the functional Nb₂O₅ layer. Specifically, devices with Nb and Ti electrodes exhibited symmetrical threshold switching under positive and negative bias, as expected for low resistance contacts. Devices with Cr electrodes exhibited asymmetric switching with a smaller hysteresis window under positive bias than under negative bias, consistent with changes in the interlayer resistance induced by field-induced oxygen exchange. In contrast, devices with Hf and Ta electrodes exhibited 1S1M switching, where the 1M response was attributed to resistive switching in a high-resistance HfO_x or TaO_x interlayer, respectively. Significantly, Pt/Nb₂O₅/Pt devices exhibited unipolar switching rather than threshold switching, clearly demonstrating the role of the reactive electrodes in mediating the threshold switching response. It is further noted that the extent of metal/oxide reaction depends on the relative thicknesses of the corresponding material layers, and remains a subject of further study.

Dopant-controlled threshold switching and S-type NDR

Volatile threshold switching has been observed in a range of materials and device structures, and two terminal MOM devices based on niobium oxides [59, 171, 260] and vanadium oxides [71, 261–264] have attracted particular attention due to their simple structure and reliability. However, even these simple structures also exhibit a diverse range of electrical characteristics depending on the film stoichiometry, crystallinity, electrode metals, device geometry and operating conditions (e.g. maximum currents, bias polarity, etc.) [57, 78, 163, 164, 218, 265]. As a consequence, understanding the physical origin of the threshold switching response and its dependencies is particularly challenging and remains as active area of research.

In this chapter, the influence of Ti doping on the threshold switching and S-type NDR response of amorphous Nb_2O_5 -based devices is studied. It is shown that doping can improve the device reliability and provide a means of tuning the threshold and hold voltages, and the magnitude of the negative differential resistance. Temperature dependent electrical measurements and lumped-element modelling show that these effects derive from changes in the oxide conductivity and its temperature dependence.

6.1 Experiments

MOM cross-point test structures with dimensions ranging from 5 μm to 20 μm were fabricated on thermally oxidised Si substrates (oxide thickness ~ 200 nm). Bottom electrodes were defined by a photolithographic lift-off process and consisted of a 15 nm Cr adhesion layer and 40 nm Pt layer deposited by successive electron-beam evaporation without breaking vacuum. The functional oxide layer was deposited uniformly over the patterned bottom electrodes and

consisted of Nb_2O_5 , Ti-doped Nb_2O_5 ($\text{Ti:Nb}_2\text{O}_5$) and TiO_2 films. The Nb_2O_5 and TiO_2 layers were deposited by rf sputtering of Nb_2O_5 and TiO_2 targets respectively, while the $\text{Ti:Nb}_2\text{O}_5$ films were deposited by rf co-sputtering of Nb_2O_5 and Ti targets. In this case the Ti/Nb fraction was controlled by varying the rf power of the Ti target (from 30 W to 120 W) while rf power of the Nb_2O_5 target was kept constant (180 W). Further details of the oxide deposition conditions are given in **Table-6.1**. Top electrodes consisted of a 5 nm Ti adhesion layer and 25 nm Pt layer were then deposited by electron-beam evaporation without breaking vacuum and their pattern was defined by a photolithographic step. Following fabrication, the devices were coated with a 40 nm SiO_2 encapsulation layer deposited by Plasma Enhanced Chemical Vapour Deposition (PECVD) at a substrate temperature ~ 300 °C. A final lithographically defined etching step was then used to open access to the top and bottom contact pads.

Table 6.1: Deposition parameters for Nb_2O_5 , Ti-doped Nb_2O_5 ($\text{Ti:Nb}_2\text{O}_5$) and TiO_2 films.

Thin Films	Sputter target/rf Power (W)	Sputter target/rf Power (W)	Pressure (mTorr)	Gas Flow (Ar/O ₂) (sccm/sccm)	Ti/Nb Fraction	Thickness (nm)
Nb_2O_5	$\text{Nb}_2\text{O}_5/180$		4		20/0	48
TiO_2	$\text{TiO}_2/300$		4		20/0	65
Ti : Nb_2O_5	$\text{Nb}_2\text{O}_5/180$	Ti/30	4	20/0	0.007 ± 0.002	54
Ti : Nb_2O_5	$\text{Nb}_2\text{O}_5/180$	Ti/60	4	20/0	0.10 ± 0.01	49
Ti : Nb_2O_5	$\text{Nb}_2\text{O}_5/180$	Ti/90	4	20/0	0.31 ± 0.04	38
Ti : Nb_2O_5	$\text{Nb}_2\text{O}_5/180$	Ti/120	4	20/0	0.72 ± 0.04	60

The composition, crystallinity and chemical state of the oxide films were characterised using RBS, GIAXRD and XPS, respectively. Layer thicknesses, crystallinity and compositions were also investigated by transmission electron microscopy (TEM) and Energy Dispersive X-ray (EDX) analysis. Electrical characterisation consisted of quasi-static current and voltage sweeps and was performed in air using an Agilent B1500A semiconductor parameter analyser attached to a Signatone probe station. In all cases, the electrical bias was applied to the top electrode while grounding the bottom electrode.

6.2 Thin Films Analysis

Selected devices were analysed by TEM and EDX to confirm the structure of the device, including layer thicknesses and elemental distributions within the oxide film, as shown in **Fig. 6.1**. Such analysis clearly showed that the co-deposited Ti is uniformly distributed

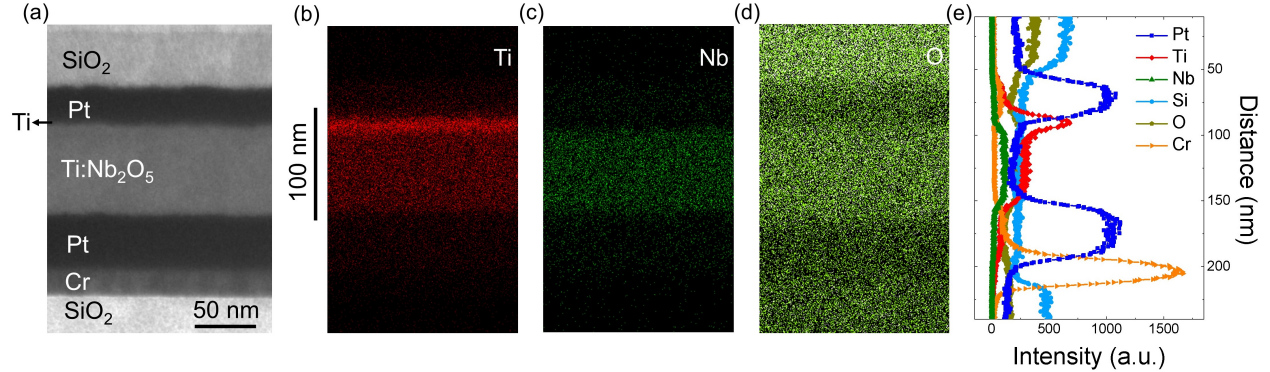


Figure 6.1: (a) Cross-sectional transmission electron micrograph of a Ti:Nb₂O₅ device with a Ti/Nb fraction of 0.72, (b-d): 2D elemental maps for Ti, Nb, and O respectively and, (e) corresponding EDX line-scan.

through the niobium oxide film. Further quantitative analysis was performed using RBS of films simultaneously deposited on silicon or carbon substrates. A typical RBS spectrum from a Ti:Nb₂O₅ layer deposited on silicon is shown in **Fig. 6.2(a)** and highlights the clear separation of the Nb, Ti and O. Analysis of such spectra was used to determine the

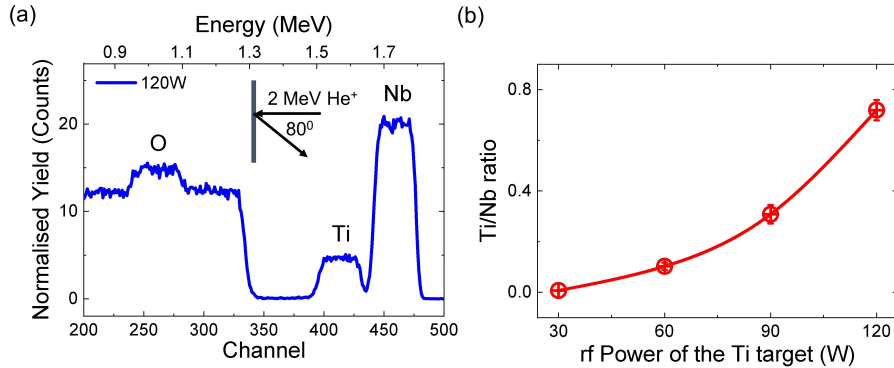


Figure 6.2: (a) Representative RBS spectra from Ti:Nb₂O₅ film (rf power \sim 120 W) deposited on a Si substrate; clear Ti, Nb and O peaks are observed, and (b) Ti/Nb ratio as a function of rf power of the Ti target.

stoichiometry, thickness and uniformity of the films and to determine the relationship between the Ti/Nb ratio and the rf power used for Ti deposition, as shown in **Fig. 6.2(b)**. Analysis

of the Nb_2O_5 and TiO_2 films showed that they were stoichiometric. Both XRD and TEM analysis showed that the as-deposited films were amorphous.

The chemical state of the oxide films was determined from XPS analysis. Representative core-level spectra and valence band spectra are shown in **Fig. 6.3**.

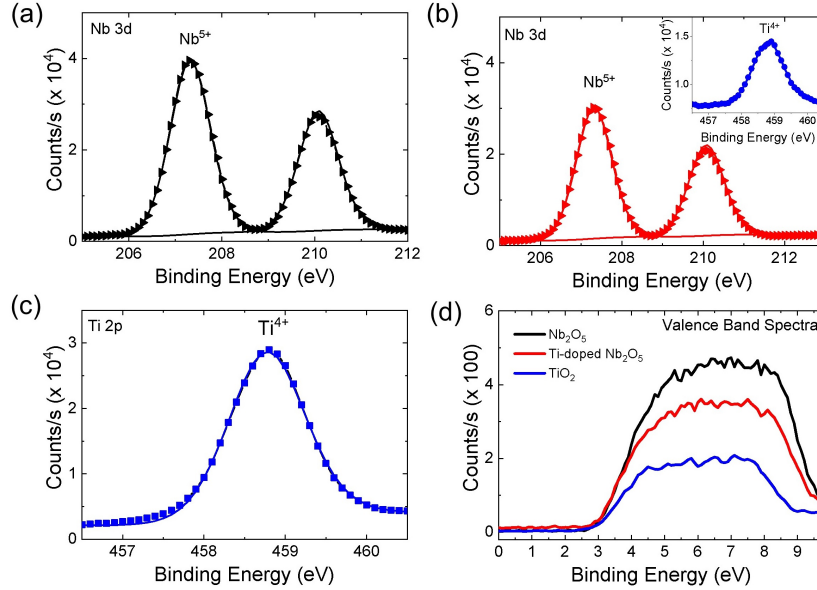


Figure 6.3: X-ray photoelectron spectra: (a) Nb-3d core level spectrum from Nb_2O_5 , (b) Nb-3d and Ti-2p_{3/2} (inset) spectra from $\text{Ti:Nb}_2\text{O}_5$ ($\text{Ti/Nb} \sim 0.31$), (c) Ti-2p_{3/2} core level spectrum from TiO_2 , and (d) valence band spectra for the Nb_2O_5 , $\text{Ti:Nb}_2\text{O}_5$ and TiO_2 films. The symbols in Fig. 6.3(a-c) represent experimental data and the solid lines show conventional fits to the data.

The Nb-3d core-level spectra from the Nb_2O_5 and $\text{Ti:Nb}_2\text{O}_5$ films are characterised by the Nb-3d_{5/2} and Nb-3d_{3/2} doublet with peaks at 207.3 eV and 210.1 eV. The position of these peaks, their symmetry and the fact that they have similar widths demonstrates that Nb^{5+} is the dominant oxidation state [234, 266]. Similarly, the Ti-2p_{3/2} peaks from the $\text{Ti:Nb}_2\text{O}_5$ and TiO_2 films have peak positions (458.7 eV) that are attributed to the Ti^{4+} oxidation state [267, 268]. These assignments are consistent with the measured stoichiometry of the Nb_2O_5 and TiO_2 films and further suggest that $\text{Ti:Nb}_2\text{O}_5$ films are solid solutions of Nb_2O_5 and TiO_2 . In drawing these conclusions it is noted that XPS analysis is limited to a depth of $\sim 3 - 10$ nm and may therefore be influenced by additional surface oxidation of the films. However, as shown in **Chapter 3 (Fig. 3.5)**, spectra from sub-stoichiometric NbO_x films show clear contributions from the Nb^{2+} and Nb^{4+} oxidation states [234, 235], thereby confirming that the measurements are sensitive to the subsurface composition of the films.

The XPS valence band spectra from Nb_2O_5 , $\text{Ti:Nb}_2\text{O}_5$ and TiO_2 films are shown in **Fig.**

6.3(d) and are all characterised by a single broad band that variously derives from Nb-4d/O-2p and Ti-3d/O-2p valence states [236, 269]. The different band heights and widths reflect the different density-of-states distributions in the films, but the valence band edges are similar in all cases, having a value of ~ 3.0 eV. This confirms the near identical bandgaps of amorphous Nb₂O₅ and TiO₂ and Ti:Nb₂O₅. It is noted that valence band spectra from sub-stoichiometric NbO_x (see **Chapter 3 (Fig. 3.5)**) exhibited an additional low energy band at binding energies (< 3 eV) due to unbonded Nb [236], and a similar band was observed for all films subjected to ion beam etching due to the radiation damage and preferential sputtering caused by Ar⁺ ion irradiation.

6.3 Electroforming and the switching response

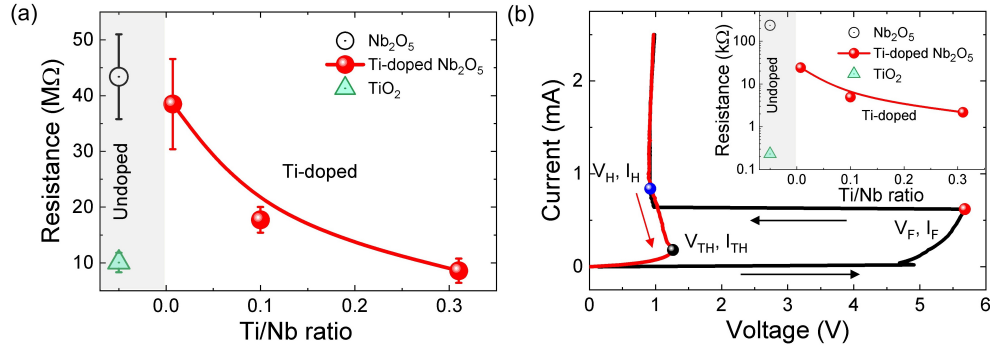


Figure 6.4: (a) Preformed resistances of $20\text{ }\mu\text{m} \times 20\text{ }\mu\text{m}$ cross point MOM devices (data were averaged for 20 devices in each case, error bars represent standard deviation from the mean value), and (b) a representative electroforming step of a Ti:Nb₂O₅ device; inset shows representative low-field (measured at 0.1V) device resistances after electroforming.

As-fabricated devices were highly insulating and required an initial electroforming step to initiate memristive switching, as summarised in **Fig. 6.4**. The highest resistance devices were those based on Nb₂O₅, with resistances of around 40 MΩ. Those based on TiO₂ had a resistance of around 10 MΩ, and those based on Ti:Nb₂O₅ had resistances that decreased from around 40 MΩ to around 10 MΩ as the Ti/Nb ratio increased from 0 to 0.31 (**Fig. 6.4(a)**). Electroforming was achieved by subjecting the devices to a bidirectional current sweep, such as that illustrated in **Fig. 6.4(b)** for a Ti:Nb₂O₅ device. This produced a permanent reduction in resistance by several orders of magnitude, consistent with the creation of a filamentary conduction path in the oxide film [82]. The resistance of the post-formed devices continued to show the same trend as the un-formed devices, with the Nb₂O₅ devices having the highest resistance, TiO₂-based devices having the lowest resistance and Ti:Nb₂O₅

devices having a resistance that decreased with increasing Ti concentration (see inset in **Fig. 6.4(b)**). This is significant because it clearly shows that filamentary conduction continues to be influenced by Ti doping.

After electroforming the devices exhibited two distinct behaviours depending on the Ti/Nb fraction, as shown in **Fig. 6.5**. Specifically, the TiO_2 and $\text{Ti:Nb}_2\text{O}_5$ devices with $\text{Ti/Nb} = 0.71$ had low resistance and exhibited continuous and reversible current-voltage characteristics (without any NDR region) over the current range investigated, while Nb_2O_5 devices and Ti-doped Nb_2O_5 devices with $\text{Ti/Nb} \leq 0.31$ exhibited continuous S-type NDR. In the latter case, increasing the Ti/Nb fraction reduced the threshold and hold voltages, as well as the associated NDR hysteresis windows of the devices. Specifically, the threshold voltage decreased from 1.7 V to 0.84 V and the hold voltage from 1.3 V to 0.81 V as the Ti/Nb fraction is increased from 0 to 0.31. This is also evident from the voltage-controlled threshold switching characteristics (**Fig. 6.5(b)**) which more clearly show the trend with increasing Ti concentration. The ability to control the switching parameters is particularly significant because it provides a means of engineering the response of devices. The effect of

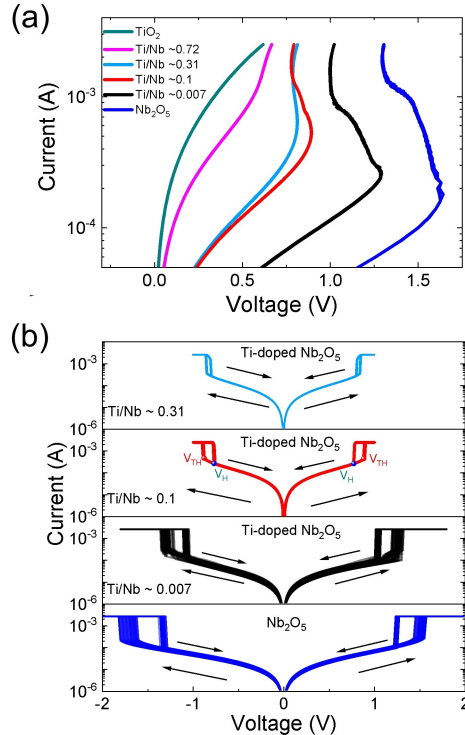


Figure 6.5: (a) Current-controlled I-V characteristics of $20 \mu\text{m} \times 20 \mu\text{m}$ cross-point devices with Nb_2O_5 , $\text{Ti:Nb}_2\text{O}_5$ and TiO_2 thin films, (b) voltage-controlled threshold switching of $20 \mu\text{m} \times 20 \mu\text{m}$ cross-point devices with Nb_2O_5 and $\text{Ti:Nb}_2\text{O}_5$ thin films (50 consecutive switching cycles are shown for each case).

Ti-doping on device uniformity and reliability was determined by comparing the characteristics of 12 separate devices for each doping condition and the cycle-to-cycle variability for devices subjected to > 6000 voltage-controlled switching cycles, respectively. Significantly, all tested devices exhibited current-controlled NDR and stable threshold switching following an initial electroforming step and representative results are shown in **Fig. 6.6**.

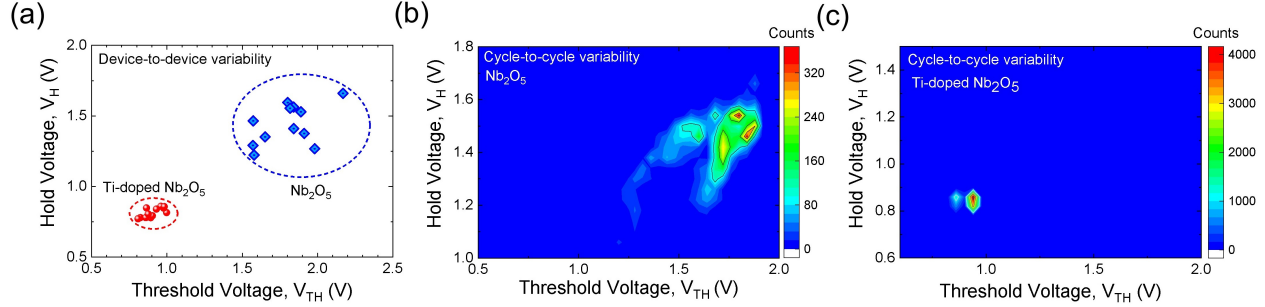


Figure 6.6: (a): Device-to-device variability of threshold and hold voltages for different devices with Nb_2O_5 and $Ti:Nb_2O_5$ ($Ti/Nb \sim 0.1$) thin films (data were extracted from stable NDR response obtained using current sweeps from 0 to 2.5 mA and compared for 12 devices in each case), and (b-c): cycle-to-cycle variability of threshold and hold voltages for representative Nb_2O_5 and $Ti:Nb_2O_5$ ($Ti/Nb \sim 0.1$) devices, respectively (data were obtained from 6000 consecutive threshold switching cycles (quasi-static I-V) for both cases).

Comparison of the threshold and hold voltage distributions clearly demonstrate that Ti-doping improves both the device uniformity and device reliability. In this context, it is interesting to note that the threshold switching response of metal/ Nb_2O_5 /Pt devices is sensitive to the nature of the interlayer formed between the reactive metal electrode and the functional Nb_2O_5 layer. The device reliability therefore also depends on the choice of metal and its relative thickness to the oxide layer, as discussed earlier in **Chapter 5**.

6.4 Temperature dependence

To better understand the effect of Ti-doping on the electrical properties of devices, the resistance of post-formed devices was measured as a function of temperature over the range from 293 K to 373 K. The results are presented as an Arrhenius plot in **Fig. 6.7** which shows that doping affects both the magnitude and temperature dependence of the filament resistance, and that the temperature dependence is well characterised by a single activation energy over the temperature range investigated. For Nb_2O_5 devices the extracted activation energy was 0.2 ± 0.02 eV and for TiO_2 devices it was 0.045 ± 0.02 eV, consistent with earlier reports [82, 270].

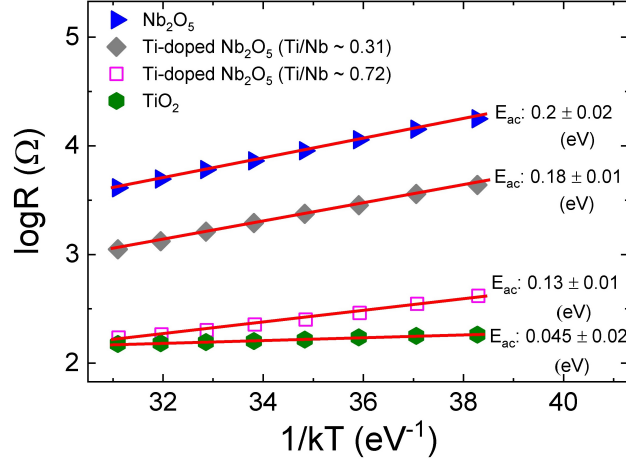


Figure 6.7: Representative temperature dependent resistance values for different devices obtained at 500mV (the data for the extracted E_{ac} were averaged for minimum three devices in each case)

Note that TiO_2 devices exhibited bipolar resistive switching after repeated positive and negative voltage sweeps (see **Appendix**) and the calculated activation energy corresponds to the low-resistance, as-formed state. The activation energy for $\text{Ti:Nb}_2\text{O}_5$ devices was generally lower than that of the Nb_2O_5 devices but showed little variation for Ti/Nb fractions between 0.007 and 0.31 ($E_{ac} \sim 0.18 \pm 0.02$ eV) while decreasing to 0.13 ± 0.01 eV for Ti/Nb fraction of ~ 0.72 .

6.5 Lumped Element Modelling

In principal, current-controlled NDR can arise from any electrical conduction mechanism that depends super-linearly on temperature [77]. However, for thermally activated processes, such as Poole-Frenkel conduction, it requires a minimum activation energy. For activation energies below this value the change in conductivity with temperature is too small to produce NDR and the voltage increases monotonically with increasing current. For activation energies above the critical value, devices exhibit current-controlled NDR and the characteristics are sensitive to the magnitude of the activation energy which can significantly impact V_{TH} and V_H . For example, changes in activation energy in the order of 20% can change V_{TH} and V_H in the order of 60%. These dependencies were investigated more thoroughly using a lumped-element circuit model of the devices.

After electroforming the NDR characteristics in MOM devices are mainly dominated by filamentary conduction and the device response can be simulated using Poole-Frenkel conduction and positive feedback from local Joule heating [229]. The resistance of the filamentary

conduction path is then given by:

$$R_m = R_0 \cdot \exp \left(\left(E_{ac} - q \sqrt{\frac{qE}{\pi \epsilon_0 \epsilon_r}} \right) / k_B T \right) \quad (6.1)$$

where R_0 is a pre-factor, E_{ac} is the activation energy (energy of the trap level) and E is the electric field. The model further assumes that the thermal response of the filament can be characterised by a thermal resistance, R_{th} , and thermal capacitance, C_{th} , where the temperature is determined by local Joule heating such that $T = R_{th}IV$. Details of the model parameters are given in the **Table-6.2**. This lumped-element model was implemented as an equivalent circuit model in LT-Spice [229].

Table 6.2: Memristor parameters used in the simulation for the Poole-Frenkel model.

Model Parameters	Symbol	Values	Unit
Thermal capacitance	C_{th}	1×10^{-15}	JK^{-1}
Resistance pre-factor	R_0	10-100	Ω
Thermal resistance	R_{th}	2×10^5	KW^{-1}
Ambient temperature	T_{amb}	298	K
Series resistance	R_1	0-100	Ω
Activation Energy	E_{ac}	0.25-0.1	eV
Relative permittivity	ϵ_r	45	
Film thickness	t	45	nm

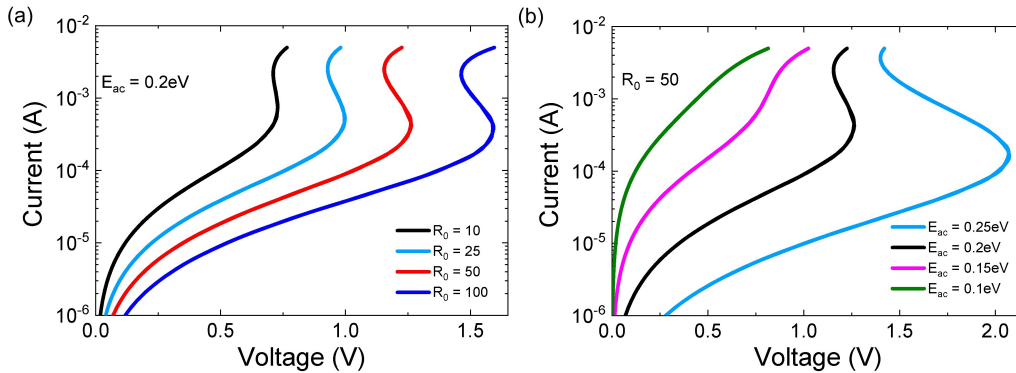


Figure 6.8: Simulated device characteristics: (a) effect of film conductivity represented by resistance pre-factor R_0 , and (b) effect of activation energy on current-controlled NDR response.

Results from the simulations are summarised in **Fig. 6.8(a-b)**, which shows the calculated I-V characteristics as a function of the resistance pre-factor (R_0) and activation energy (E_{ac}). Values and ranges of these parameters have been chosen to broadly match those of

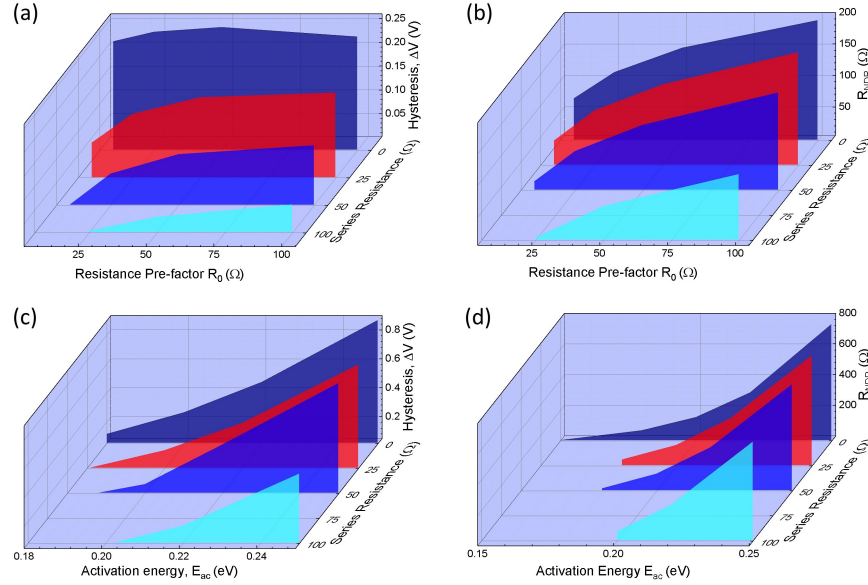


Figure 6.9: Lumped element modelling: (a-b) effect of resistance pre-factor (R_0) on the threshold voltage hysteresis and R_{NDR} , respectively, and (c-d) role of activation energy E_{ac} on the same.

the measured devices. Variation of R_0 is seen to have a direct effect on the threshold and hold voltages and the maximum magnitude of the NDR (R_{NDR}). For the example shown in **Fig. 6.8(a)**, a 10-fold reduction in R_0 from 100 Ω to 10 Ω reduces the threshold voltage from 1.59 V to 0.72 V and the hold voltage from 1.46 V to 0.71 V, and reduces R_{NDR} from 159.5 Ω to 18 Ω . Variation of E_{ac} has a similar effect, as shown in **Fig. 6.8(b)**. In this case, reducing the activation energy from 0.25 eV to 0.2 eV shifts the threshold voltage from 2.07 V to 1.26 V and the hold voltage from 1.4 V to 1.15 V, producing a corresponding reduction in the hysteresis window from 0.81 V to 0.11 V and a decrease in R_{NDR} from 692 Ω to 108 Ω . The data in **Fig. 6.8(b)** also show that there is a critical activation energy (~ 0.15 eV) below which the device no longer exhibits NDR. Note that the addition of a series resistance (R_1) in the model affects the details of the simulations [271], but does not affect the general conclusions. Further information about these dependencies is given in **Fig. 6.9**.

By comparing the simulation results with the data in **Fig. 6.5** it is possible to draw some general conclusions about the effect of doping. In particular, the observed reductions in V_{TH} , V_H and R_{NDR} with increasing Ti/Nb fraction can be attributed to reductions in R_0 and E_{ac} . Since the width of the hysteresis window reflects the relative shifts in V_{TH} and V_H it too can be attributed to reductions in these parameters. However, V_{TH} is more sensitive to changes in E_{ac} than R_0 , and as a consequence so are the changes in the width of the hysteresis window. For example, a change in activation energy of ± 0.02 eV (approximately

the experimental error in the current measurements) is more than adequate to account for the observed change in the hysteresis window and associated R_{NDR} . The dominant role of E_{ac} is further supported by the fact that a reduction in E_{ac} can also account for the transition to monotonic I-V characteristics observed for the TiO_2 and $\text{Ti:Nb}_2\text{O}_5$ ($\text{Ti/Nb} = 0.72$) devices.

6.6 Summary

In summary, the effect of Ti-doping on the threshold switching response of Nb_2O_5 -based cross-point devices have been studied and shown that it provides a convenient means of improving device reliability and tailoring switching characteristics. Systematic changes in the device characteristics were demonstrated for Ti/Nb fractions up to 0.31, including reductions in the threshold and hold voltages, the hysteresis window and R_{NDR} . At higher Ti/Nb fractions (i.e., 0.72) the devices no longer exhibited NDR and the current-voltage characteristics were monotonic. Lumped-element modelling showed that these effects resulted from a reduction in the device resistance and its rate of change with temperature, where the latter was characterised by an effective thermal activation energy. Significantly, these studies also demonstrated that a critical activation energy is required to observe negative differential resistance.

Physical origin of the discontinuous ‘snapback’ NDR

Two terminal MOM devices with a threshold switching characteristic typically exhibit a continuous S-shaped current-voltage response under current-controlled testing which is produced by materials with a strong temperature dependent electrical conductivity [77]. However, recent studies have also highlighted the existence of a second, discontinuous snapback NDR characteristic, the underlying physical mechanism of which has been a subject of active debate as discussed in **Chapter 2**. In an attempt to resolve the ensuing debate about the origin of the snapback response and also to explain a diverse range of NDR modes observed in MOM devices, the two-zone parallel memristor model of NDR was developed [152] as discussed in **Chapter 3**. According to this model, the threshold switching response after electroforming is highly localised and the specific shape of the current-controlled NDR depends on the relative magnitudes of the maximum negative differential resistance (R_{NDR}) of the core and the shell resistances (R_{S}). Since the magnitude of shell resistance (R_{S}) depends on the conductivity (σ_{oxide}), area (A), thickness (t) and temperature (T) of the oxide film, the model predicts that the transition from S-type to snapback characteristics can be directly controlled by these parameters.

In this chapter, in-situ thermo-reflectance imaging and quasi-static current-voltage characteristics of NbO_x -based cross-point devices are used to determine the origin of the snapback mode of NDR and validate the assumptions and predictions of the two-zone parallel memristor model of NDR. This is achieved by correlating NDR characteristics with device current distributions and by demonstrating that NDR characteristics transition between S-type to snapback modes at critical values of film conductivity, area, thickness and temperature as predicted by the model.

7.1 Experimental Methods

The devices employed in this study were Nb/NbO_x/Pt cross-point structures fabricated using standard photolithographic processes as described in **Chapter 3**. The bottom electrode, comprising 5 nm Nb (or 10 nm Cr) and 25 nm Pt (or 40 nm Pt) layers, was deposited by e-beam evaporation on a 300 nm thermal oxide layer on a Si (100) wafer. NbO_x dielectric layers of varied composition were subsequently deposited using either rf sputtering of a Nb₂O₅ target in an Ar ambient or dc sputtering of a Nb target in a variable O₂/Ar ambient. Details of the deposition conditions are given in **Chapter 3 (Table 3.1)**. GIAXRD analysis of oxide films deposited onto Si substrates confirmed that they were amorphous, while Rutherford backscattering spectrometry (RBS) of films deposited onto vitreous carbon or Si substrates showed compositions from $x = 2.60 (\pm 0.05)$ to $1.92 (\pm 0.03)$ (i.e., oxygen rich Nb₂O₅ to sub-stoichiometric NbO₂). To complete the device structure, 25 nm Pt (or 25 nm Au) was deposited with a 5 nm Nb adhesion layer. Electrical measurements were performed using an Agilent B1500A semiconductor parameter analyser attached to a Signatone probe station (S-1160). All measurements were executed under atmospheric conditions by applying voltage on the top electrode, while the bottom electrode was grounded. Note that switching characteristics were measured with negative bias applied to the top electrode unless otherwise stated. In-situ temperature measurements were performed with a TMX T°Imager® transient thermorefectance (TR) imaging system using a 100x objective lens and a 490 nm illumination wavelength. For these measurements dc and pulsed electrical signals were supplied by a Keithley 2410 parameter analyser.

7.2 Effect of film conductivity on NDR modes

The effect of oxide conductivity on electroforming and NDR characteristics was assessed using $10\text{ }\mu\text{m} \times 10\text{ }\mu\text{m}$ cross-point devices with low ($x = 2.6$) and high ($x = 1.92$) conductivity NbO_x films. (The relationship between composition and conductivity is depicted in **Chapter 4**). Electroforming was conducted in current-controlled mode using bi-directional current sweeps, with typical results for the low conductivity film shown in **Fig. 7.1(a)**. This produces a sudden reduction in voltage as the current is increased beyond a critical threshold value and produces a permanent change in resistance from a few M Ω before electroforming to around 10 - 20 k Ω after electroforming. This is consistent with the creation of a permanent conductive filament. After electroforming, the devices exhibited stable S-type NDR characteristics as shown in **Fig. 7.1(b)**. In contrast, devices with high conductivity films exhibited a snapback-characteristic during electroforming, as shown in **Fig. 7.1(c)**. In this case electroforming had

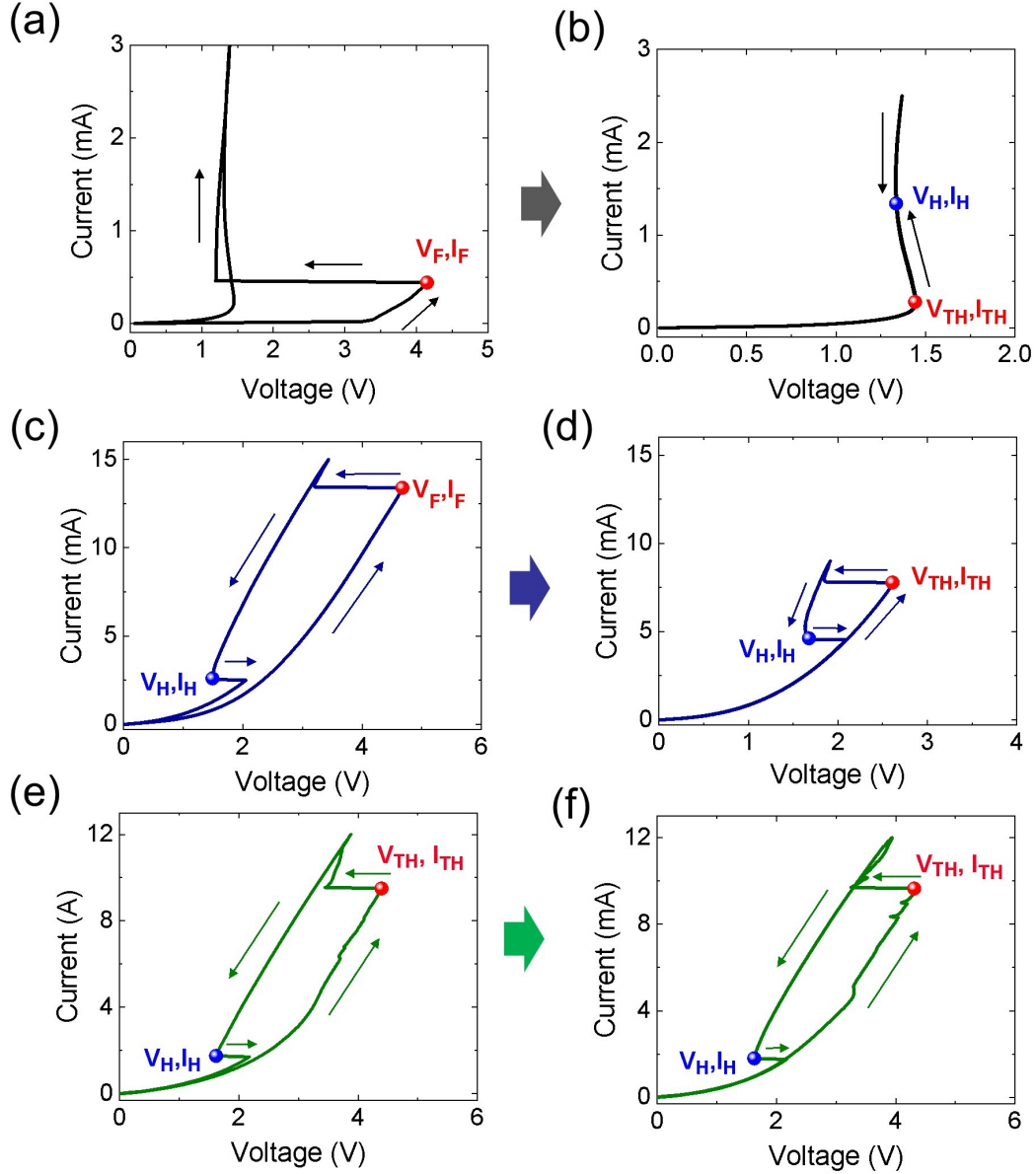


Figure 7.1: Electroforming and NDR characteristics as a function of stoichiometry. (a) Electroforming, and (b) subsequent S-type NDR characteristics of a 10 $\mu\text{m} \times 10 \mu\text{m}$ cross-point device of 25 nm Pt/5 nm Nb/NbO_{2.6}/25 nm Pt structure. (c) Electroforming at 15 mA, and (d) subsequent snapback NDR characteristics of a 10 $\mu\text{m} \times 10 \mu\text{m}$ cross-point device of 25 nm Pt/5 nm Nb/44 nm NbO_{1.92}/40 nm Pt structure. (e) Electroforming at 12 mA, and (f) subsequent switching snapback characteristics a 10 $\mu\text{m} \times 10 \mu\text{m}$ cross-point device with 25 nm Pt/5 nm Nb/44 nm NbO_{1.92}/40 nm Pt structure indicating switching due to current bifurcation. Note that switching characteristics of all samples were measured with negative bias applied to the top electrode unless otherwise stated.

only a minor impact on the device resistance, reducing it from around 5 k Ω to around 3 k Ω . Subsequent current-scans produced a similar snapback response but with a lower threshold voltage and threshold current, as shown in **Fig. 7.1(d)**.

The electroforming characteristics of the high-conductivity films were also found to depend on the maximum current employed for forming, with devices subjected to lower currents exhibiting snapback characteristics without the creation of a permanent filament. This is illustrated in **Figs. 7.2(e-f)**, which show successive current-sweeps for a high-conductivity film formed with a maximum current of 12 mA, compared to the 15 mA employed for the previous measurement in **Figs. 7.1(c-d)**. No significant change in device resistance was observed after the initial snapback response and identical characteristics were measured during a second sweep, consistent with the current bifurcating into domains of high and low current-density. However, repeated cycling did eventually cause a reduction in resistance and a concomitant reduction in both threshold-voltage and threshold-current, consistent with the creation of a permanent filament [246].

These results are consistent with the predictions of the two-zone model in that the low-conductivity film ($x = 2.6$) (i.e., higher shell resistance), exhibits S-type NDR characteristics, while the high conductivity film ($x = 1.92$) (i.e., low shell resistance), exhibits snapback characteristics, as expected. Significantly, they also demonstrate that the snapback response does not depend on the existence of a permanent conductive filament as shown earlier in **Chapter 4**.

7.3 In-situ temperature mapping

To further understand the significance of current localisation and the role of the shell region as a current divider, in-situ thermo-reflectance measurements were performed on devices exhibiting S-type and snapback NDR characteristics. These measurements were performed on NbO_x films with a conductivity intermediate between those above (i.e., $x = 2.05$) and included devices with and without permanent filaments. The results are summarised in **Fig. 7.2** which shows measured current-voltage characteristics and temperature distributions for three devices: a post-formed 5 μm device with a permanent filament that exhibits S-type NDR (**Figs. 7.2(a-c)**); a post-formed 10 μm device with a permanent filament that exhibits snapback NDR (**Figs. 7.2(d-f)**); and a device without a permanent filament that exhibits snapback NDR (**Figs. 7.2(g-i)**).

The devices with permanent filaments have highly localised temperature distributions over the full range of operating currents, as expected for filamentary conduction, but the response of the surrounding shell temperature is distinctly different in the two devices. For

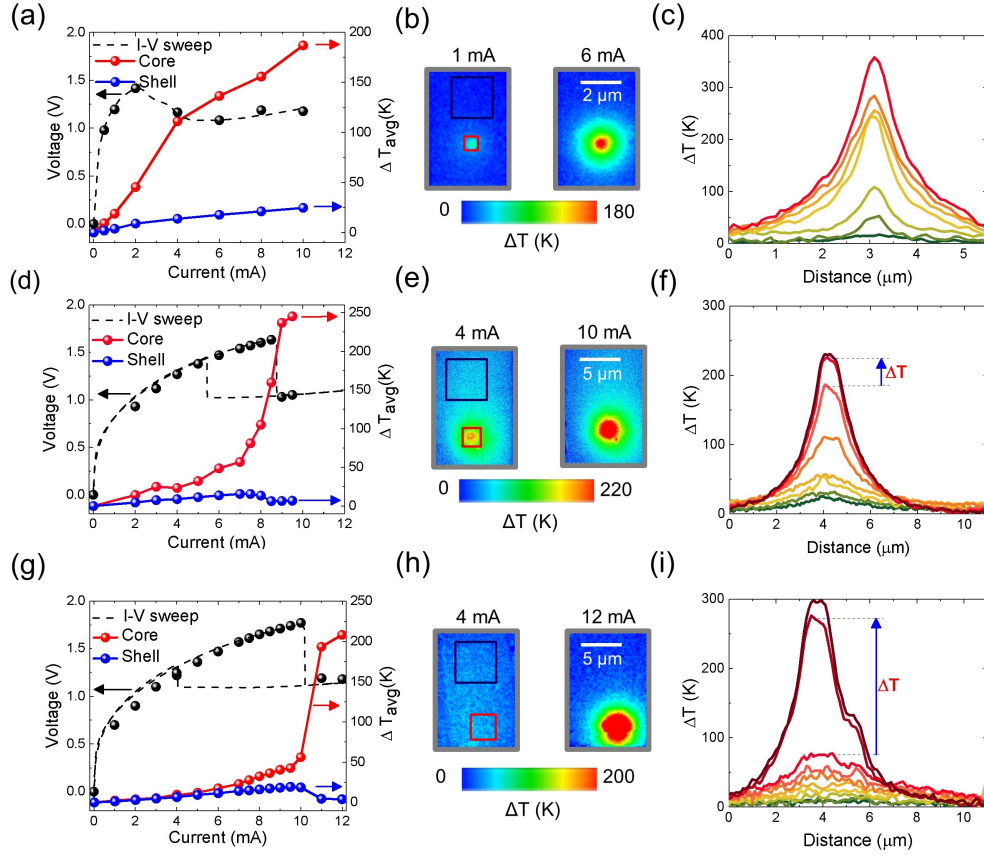


Figure 7.2: In-situ temperature measurements of S-type and snapback NDR. (a) Current-voltage characteristics and average temperature rise of the filament and surrounding area (the area used for averaging is indicated by boxes in (b)) as a function of applied current. (b) 2D maps of the surface temperature rise in a 5 μm device operating at 1 mA and 6 mA. (c) Current localisation of S-type NDR in the post-formed device at different current levels as shown in (a). (d) The average temperature rise of the permanent filament and surrounding area (indicated by boxes in (e)) as a function of applied current, and (e) 2D map of the surface temperature in a 10 μm device at pre-threshold (4mA) and post-threshold (10 mA) regions. (f) Current localisation in post-formed device at different current levels as shown in (d) (the blue arrow indicates snapback transition). (g) The average temperature rise of the current filament and surrounding area (indicated by boxes in (h)) as a function of applied current, and (e) 2D map of the surface temperature in a 10 μm device at pre-threshold (4 mA) and post-threshold (12 mA) regions. (i) Current localisation due to current bifurcation in the device without permanent filament as shown in (g) (the blue arrow indicates snapback transition). The device structure used in thermoreflectance measurements is 25 nm Au/5 nm Nb/35 nm NbO_{2.05}/40 nm Pt. The circles overlaying the I-V curves represent in-situ I-V measurements during thermoreflectance measurements.

the device exhibiting S-type NDR (**Fig. 7.2(a)**) both the core temperature and that of the surroundings shell increase monotonically with current, while for the device exhibiting snapback NDR (**Fig. 7.2(d)**) the temperature of the core increases rapidly during snapback while that of the surrounding shell decreases. As the temperature distribution reflects that of the current, the reduction in shell temperature is consistent with the role of the shell as a current divider, with the shell current decreasing due to the increase in core conductivity. In contrast to the devices with permanent filaments, the third device has a spatially uniform current distribution in the sub-threshold current range but undergoes bifurcation into high and low current density domains at, or near, the threshold current (**Figs. 7.2(g-i)**). As for the filamentary snapback device this is also associated with a concomitant reduction in shell temperature. These results clearly demonstrate that the snapback response is associated with current localisation, either due to a pre-existing permanent filament or current bifurcation, and the redistribution of current between low and high current-density domains.

7.4 Area dependence of NDR modes

Area dependent switching response was studied using devices with 25 nm Pt/5 nm Nb/44 nm NbO_{1.92}/40 nm Pt structures. The obtained current-voltage characteristics are shown in **Fig. 7.3** which highlight the role of device area in controlling the NDR mode, with the smaller area device (higher shell resistance) exhibiting S-type NDR and the larger area devices (lower shell resistance) exhibiting snapback NDR. This dependence was investigated

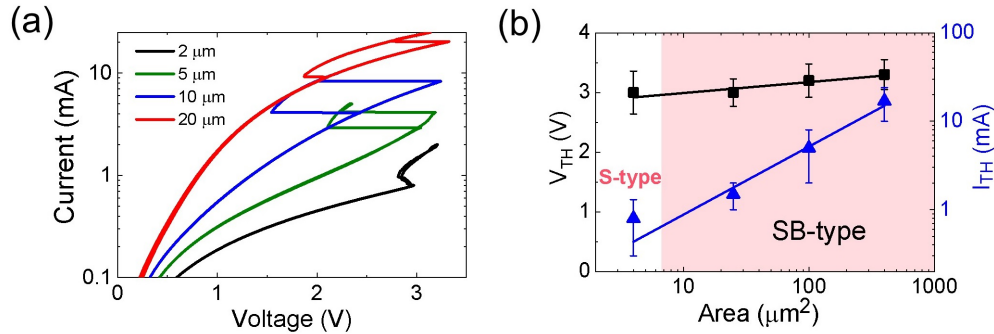


Figure 7.3: Area dependent switching properties of NbO_x with $x = 1.92$. (a) NDR characteristics as function of area showing area dependent S-type NDR and snapback (SB)-type NDR, and (b) threshold voltage and current as a function of area.

more explicitly by comparing the response of devices with different stoichiometry and side lengths of 2 μm, 5 μm, 10 μm and 20 μm. Significantly, low-conductivity films ($x = 2.6$) were found to exhibit S-type NDR characteristics independent of device area, demonstrating that

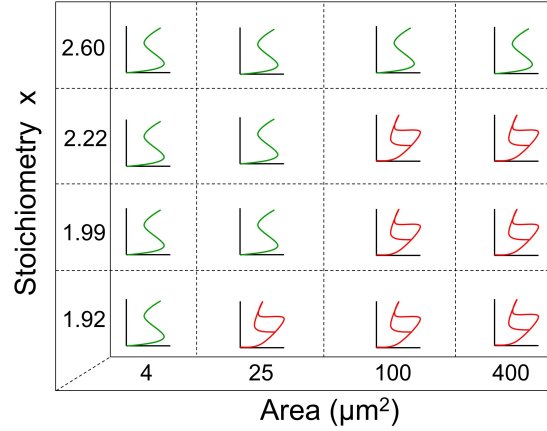


Figure 7.4: Matrix representation (schematic) of dependency of S-type and snapback NDR (red lines) as a function of stoichiometry and area.

the shell resistance satisfied the condition $R_S > R_{\text{NDR}}$ for areas as small as $4 \mu\text{m}^2$. In contrast, high conductivity films ($x = 1.92$) were found to have area-dependent NDR characteristics exhibiting the transition from snapback to S-type NDR as shown in **Fig. 7.3(a)**.

The threshold voltage (V_{TH}) for these devices was $3.0 \pm 0.4 \text{ V}$ and is almost independent of device area, as shown in **Fig. 7.3(b)**. However, the corresponding threshold current (or threshold power, $P_{\text{TH}} = I_{\text{TH}} \times V_{\text{TH}}$) was found to increase monotonically with increasing device area, as expected from the reduced film resistivity. This contrasts with situation for the low conductivity films where the threshold power remains constant with device area [82]. Results for all film compositions are summarised in **Fig. 7.4** and reflect the predicted area dependence, with large area devices having lower shell resistance and exhibiting snapback characteristics, and smaller area devices having higher shell-resistance and exhibiting S-type NDR characteristics.

7.5 Thickness dependence of NDR modes

The effect of film thickness was investigated using $10 \mu\text{m} \times 10 \mu\text{m}$ devices with 25 nm Au/5 nm Nb/NbO_{2.05}/40 nm Pt structures. All devices underwent an initial electroforming step prior to measuring NDR characteristics. For all devices the forming current was found to decrease linearly with increasing film thickness (see **Appendix**), from $33.4 \pm 5.2 \text{ mA}$ for a film of 35 nm thickness to $10 \pm 2.1 \text{ mA}$ for a film of 93 nm thickness, consistent with the expected increase in film resistance. The NDR characteristics were then found to depend on film thickness, with films of thickness $\leq 77 \text{ nm}$ exhibiting snapback characteristics and a film of thickness 93 nm exhibiting S-type NDR characteristics, as shown in **Fig. 7.5(a)**. This is accompanied by an increase in threshold voltage and a decrease in threshold current (see **Fig.**

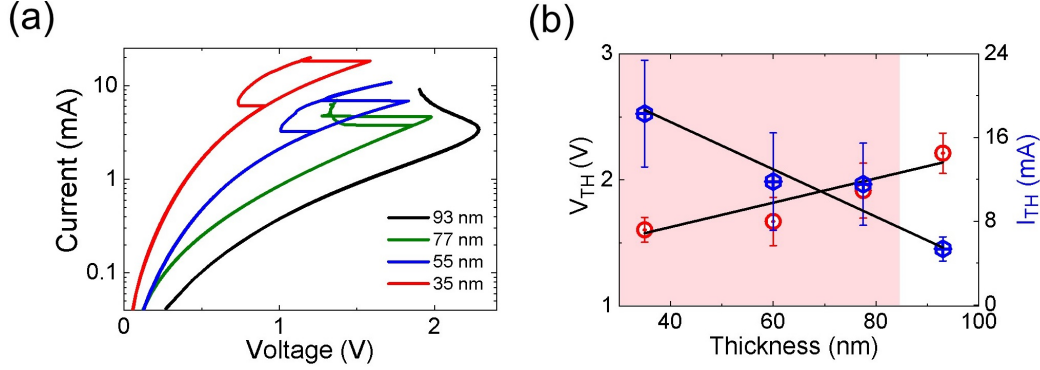


Figure 7.5: Thickness dependence of switching properties of NbO_x with $x = 2.05$. (a) Thickness dependent current-voltage characteristics of $10\ \mu\text{m} \times 10\ \mu\text{m}$ devices showing S-type NDR and snapback (SB-NDR). (b) Threshold voltage and current as a function of thickness with switching mode depicted by shading. Data points represent averages for ten devices of each thickness

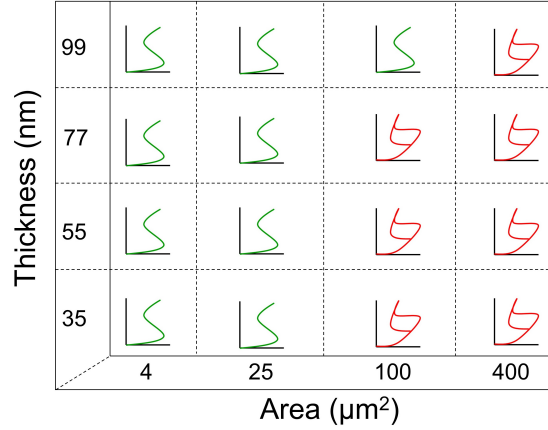


Figure 7.6: Matrix representation (schematic) of dependency of S-type and snapback NDR (red lines) as a function of thickness.

7.5(b)), consistent with the increase in film resistance with increasing thickness. Similar to the conductivity and area dependence as mentioned earlier, these results are also consistent with model predictions based on the assumption that the shell resistance transitions from the condition $R_S > R_{NDR}$ for the 93 nm thick film to $R_S < R_{NDR}$ for films of thickness less than 77 nm. **Fig. 7.6** summarises results for devices of different areas and thicknesses and shows that the transition between S-type and snapback NDR was limited to $10\ \mu\text{m} \times 10\ \mu\text{m}$ devices for the thickness range investigated. .

7.6 Temperature dependence of NDR modes

Finally, the effect of substrate temperature on NDR characteristics was examined. The devices used for these studies had a NbO_x composition of $x = 2.22$. These devices exhibited a snapback response at 293 K after electroforming but transitioned to an S-type response as the temperature was increased to 323 K, as shown in **Fig. 7.7(a)**. Above this point, the device continued to exhibit S-type NDR within the investigated temperature range. This is counterintuitive, as the resistance of the shell is expected to decrease with increasing substrate temperature and to produce a transition from smooth to snapback characteristics as the temperature exceeds the point where $R_S < R_{\text{NDR}}$. The increase in oxide conductivity with temperature is evident from the decrease in threshold voltage (V_{TH}) and the increase in threshold current (I_{TH}) shown in **Fig. 7.7(b)**. Given the transition criterion $R_S < R_{\text{NDR}}$, these results suggest that the core R_{NDR} also varies with temperature and that it decreases more rapidly with temperature than the surrounding oxide shell. However, this remains the subject of further studies.

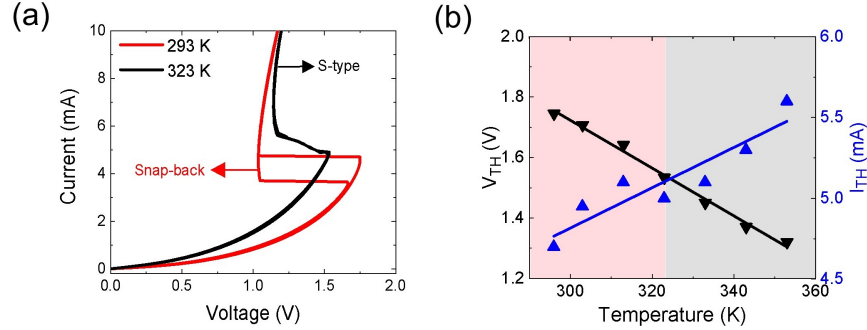


Figure 7.7: Effect of substrate temperature on NDR behaviour. (a) Examples of NDR responses at two distinct substrate temperatures, and (b) extracted threshold -voltages and -currents as a function of substrate temperature. The shaded region in (b) identify devices that exhibit S-type (S-NDR-grey) and snapback (SB-NDR-red) responses.

7.7 Discussion

The above results clearly demonstrate that the NDR response of NbO_x -based cross-point devices can be controlled by the oxide conductivity, area and thickness and that the snapback mode of NDR is associated with redistribution of current from low to high current-density domains in a manner consistent with the proposed core-shell model of current transport. Significantly, the results also explain several interesting results reported in the literature and

resolve a long-standing controversy about the origin of the snapback mode of NDR. Specifically, the area dependence of the NDR response observed in the finite element simulations by Goodwill et al [79] can now be understood in terms of the relative resistances of the core and shell regions and the associated current redistribution. However, this is only one of several dependencies that control the transition from S-type to snapback NDR. Moreover, the snapback behaviour is not predicated on current bifurcation but simply requires current localisation, as is evident from the response of electroformed devices that retain a permanent filament (**Fig. 7.2(d-f)**). In that case, current confinement is preordained and the dominant NDR mode is determined mainly by the resistance of the shell region. Finally, because the snapback NDR derives from the same physical mechanism as the S-type NDR it has a similar onset temperature, estimated to be $\sim 400 - 600$ K (as shown in **Fig. 7.2**) [77]. As this is simply determined by the temperature dependence of the film conductivity [77] it explains why snapback NDR is observed in a diverse range of amorphous metal oxides and obviates the need for a material-specific phase transition [78].

7.8 Summary

In summary, it has been demonstrated that the NDR characteristics of NbO_x cross-point devices can be controlled by materials and device parameters and that these dependencies are consistent with the predictions of a model that can account for a non-uniform current distribution and the redistribution of current from regions of low to high current density. This was achieved by using in-situ thermorefectance imaging to correlate NDR characteristics with changes in current distribution, and by systematically studying how the transition from S-type to snapback NDR depended on the conductivity, area, thickness and temperature of the NbO_x film. These results conclusively demonstrated that the snapback characteristic is a generic response of materials with a strong temperature dependent conductivity and that it has the same physical origin as the S-type characteristic.

Asymmetric NDR and the role of interface barriers

Two-terminal MOM structures can exhibit a diverse range of NDR responses, including S-type, snapback or a combination of both. While the S-type NDR is well-explained by a strong temperature-dependent conductivity change due to local joule heating, the origin of snapback response can be understood by including the effect of parallel device resistance as discussed in **Chapter 7**. The parallel resistance (R_S) is determined by the area, thickness and resistivity of the oxide film and also influenced by the substrate temperature. For devices fabricated with near-stoichiometric oxide films the parallel resistance (R_S) is typically dominated by the film resistivity such that $R_S > R_{\text{NDR}}$ and they exhibit S-type NDR [82]. However, for more conductive sub-stoichiometric films the contact resistance is also expected to make a significant contribution to the parallel resistance and thereby may influence the dominant threshold switching mode as well as the device stability and reproducibility.

In this chapter, it is demonstrated that the interface resistance originating from the Schottky barriers at the metal/oxide interfaces can indeed result in distinct NDR modes depending on the operating bias polarity, area and oxide conductivity. This is achieved by combining in-situ thermo-reflectance imaging and temperature dependent electrical testing of NbO_x cross point devices, and the results explained with reference to the two-zone parallel memristor model of NDR as discussed in the earlier chapters.

8.1 Experiments

Cross-point devices with a metal/oxide/metal structure were fabricated on a thermally oxidised Si (100) wafer with a 300 nm thick oxide layer using a three-mask photolithography

process as described in **Chapter 3**. The bottom electrodes were defined by a lift-off process and consisted of a 5 nm Ti (or 10 nm Cr) adhesion layer and a 25 nm (or 40 nm) Pt electrode layer, deposited by e-beam evaporation. These were coated with sub-stoichiometric NbO_x layers by reactive sputter deposition of an Nb target using an Ar/O ambient. For comparison, a near-stoichiometric Nb_2O_5 film was also deposited by rf-sputtering of an Nb_2O_5 target (Ar ambient). Top electrodes were subsequently defined by a second lift-off process and comprised of 5 nm Nb and 25 nm Pt (or 75 nm Au for the thermo-reflectance measurements). A final lithography step was then used to remove the NbO_x film from the contact-pads of the bottom electrodes. Details of the deposition conditions and film thicknesses are given in **Table-3.1 (Chapter 3)**. The resulting cross-point structures had dimensions ranging from $2\text{ }\mu\text{m} \times 2\text{ }\mu\text{m}$ to $20\text{ }\mu\text{m} \times 20\text{ }\mu\text{m}$. The NbO_x stoichiometry was determined by Rutherford backscattering spectrometry (RBS) of films deposited onto vitreous carbon and Si substrates and was found to be in the range from $x = 1.92 (\pm 0.03)$ to $x = 2.6 (\pm 0.05)$. Further analysis by grazing incident-angle X-ray diffraction (GIAXRD) showed that the as-deposited films were amorphous. The uniformity of the films was obtained by rotating the sample substrate during sputtering and confirmed by measuring the oxide film thicknesses over the entire deposited area. Ex-situ electrical measurements were performed in air using an Agilent B1500A semiconductor parameter analyser attached to a Signatone probe station (S-1160) and generally consisted of bidirectional quasi-static current sweeps. In-situ measurements performed during thermoreflectance imaging were performed with a Keithley 2410 parameter analyser and included both dc and pulsed testing. In all cases the bias was applied through the top electrode while the bottom electrode was grounded. Thermal imaging of the devices was performed using the TMX T°Imager® system as described in **Chapter 3**.

8.2 Electroforming and NDR characteristics

All devices with sub-stoichiometric NbO_x films exhibited negative differential resistance (NDR) following a one-off electroforming step. However, the forming and NDR characteristics were found to depend on the measurement polarity, as illustrated in **Fig. 8.1** for $5\text{ }\mu\text{m NbO}_{1.92}$ devices.

During an initial positive bias sweep from $0 \rightarrow 8\text{ mA}$ (**Fig. 8.1(a)**), the device undergoes an electroforming step characterised by a sudden voltage drop at a current $\sim 6\text{ mA}$ and a permanent change in the low-field device resistance from $\sim 5\text{ k}\Omega$ to $\sim 4.5\text{ k}\Omega$ (measured at 0.25 V). The impact of electroforming is then clearly evident during the reverse current sweep (from $8 \rightarrow 0\text{ mA}$) which shows S-type NDR. Subsequent current sweeps under positive bias continued to show S-type characteristics under both forward and reverse sweeps (similar to

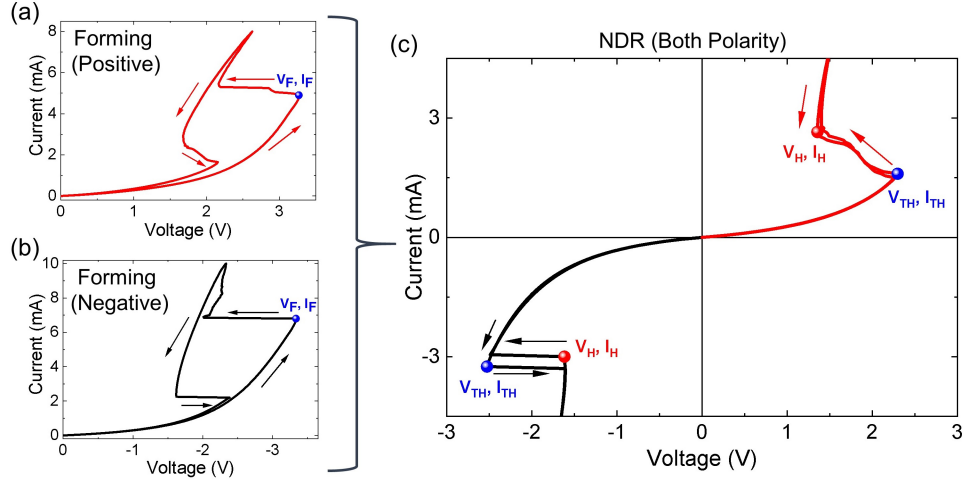


Figure 8.1: Polarity dependent electroforming and NDR characteristics of Pt/Nb/ NbO_{1.92} /Pt devices: (a) electroforming of a $5\ \mu\text{m} \times 5\ \mu\text{m}$ cross-point device under positive bias, (b) electroforming of a different $5\ \mu\text{m} \times 5\ \mu\text{m}$ cross-point device under negative bias; and (c) typical polarity-dependent switching characteristics of electroformed devices showing a transition from S-type to snapback NDR irrespective of electroforming polarity.

that shown by the red line in **Fig. 8.1(c)**).

Similar electroforming characteristics were observed in an identical device under negative bias during the forward sweep from $0 \rightarrow 10\ \text{mA}$ (**Fig. 8.1(b)**), with a sudden voltage drop observed at a current of $\sim 7\ \text{mA}$. However, in this case, the reverse current sweep produced a snapback characteristic, with an abrupt voltage increase as the current was reduced to $\sim 2.2\ \text{mA}$. Subsequent current sweeps under negative bias showed similar snapback characteristics for both forward and reverse sweeps, but at a lower threshold-current and voltage (similar to that shown by the black line in **Fig. 8.1(c)**). Once electroformed, devices exhibited characteristics similar to those depicted in **Fig. 8.1(c)**, regardless of the initial electroforming polarity. That is, under positive bias they exhibited S-type NDR during forward and reverse current sweeps and under negative bias they exhibited a snapback response.

The permanent changes produced by electroforming are typically attributed to the creation of a filamentary conduction path in the oxide film and/or local breakdown of the Schottky barriers at the metal/oxide interfaces. From a circuit perspective this represents a parallel conduction path within the device and the total device current is divided between the filamentary conduction path and the surrounding device area based on their relative resistances as discussed in **Chapter 3**. Indeed, even though the filamentary region may have a higher conductivity, its resistance can exceed that of the surrounding device due to its smaller effective area.

8.3 In-situ temperature mapping

In-situ thermo-reflectance imaging was performed on $10\text{ }\mu\text{m}$ $\text{NbO}_{1.99}$ devices to better understand the current distribution during post-forming current sweeps. The results are summarised in **Fig. 8.2** and include the in-situ current-voltage (I-V) characteristics and the measured temperature distributions for devices subjected to positive and negative bias. Un-

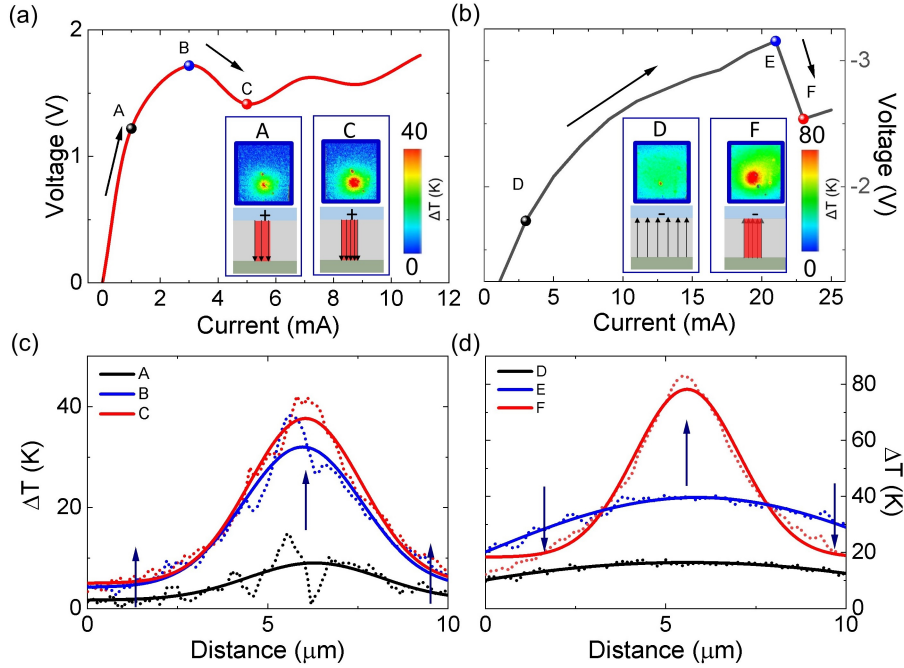


Figure 8.2: (a-b), In-situ I-V characteristics of a $10\text{ }\mu\text{m} \times 10\text{ }\mu\text{m}$ $\text{NbO}_{1.99}$ device showing (a) S-type NDR under positive bias, and (b) snapback under negative bias. Insets show the in-situ thermorefectance maps of the device during I-V testing, (c) Temperature profile through the filamentary region for different current-voltage values during positive bias. (d) Temperature profile of the same device for different current-voltage values during negative bias. The dashed curves in (c) and (d) represent the experimental data and the smooth lines show Gaussian fits of the data. A, B, and C denote subthreshold, threshold, and post-threshold points respectively in the I-V characteristic obtained under positive bias, while D, E, and F denote the same for negative bias polarity.

der positive bias the temperature distribution is highly localised in the filamentary region over the entire range of operating currents and the temperature in this region and the surrounding film increase monotonically with increasing current. The S-type NDR characteristic demonstrates that the resistance of the filamentary path is lower than that of the surrounding device and the NDR is dominated by the temperature-dependent conductivity of the filamentary region. In contrast, under negative bias, the temperature distribution is near-uniform at currents below the threshold for snapback and only becomes localised for currents

near the threshold value (indicated by the point ‘F’ in **Fig. 8.2(b)**). At this point the temperature of the filament increases abruptly while that of the surrounding area decreases, consistent with current redistribution and localisation due to the positive feedback created by local Joule heating. This demonstrates that the resistance of the filamentary region is initially comparable to or greater than that of the surrounding device but becomes relatively less resistive as the current increases to the threshold value. Such a change implies that the conductivity of the filamentary region increases more rapidly with temperature than that of the surrounding device. For filaments near the centre of the device this may also be facilitated by the non-uniform temperature distribution created by the device geometry (see **Fig. 8.2(c)**). It is important to note that the extent of the filamentary region (see **Chapter 4, Fig. 4.7**) is smaller than that of the temperature distribution observed at the top electrode surface due to the high thermal conductivity of the metal electrode.

8.4 Schottky barriers and polarity dependent conduction

The temperature-dependent I-V characteristics of an as-fabricated Nb/NbO_{2.22}/Pt device are shown in **Fig. 8.3(a)** for both positive and negative bias. Comparison of the device current at equivalent positive and negative voltages clearly highlights the asymmetry in contact resistance created by the Schottky barriers at the metal/oxide interfaces. Similar asymmetry was observed for all NbO_x films used in this study and was found to increase with increasing device area. From the electron affinity of Nb₂O₅ (3.9 eV) and the work functions of Nb (4.3 eV) and Pt (5.65 eV) the theoretical barrier heights at the Nb/oxide and Pt/oxide interfaces are calculated to be 0.4 eV and 1.75 eV, respectively [84]. As a consequence, the contact resistance is expected to be dominated by Schottky barrier at the Pt/oxide interface, which is under forward bias when negative voltage is applied to the top electrode.

Experimentally, the current-voltage characteristics were analysed in terms of field-enhanced thermionic emission over a Schottky barrier, as described by [85]:

$$I = AA^*T^2.exp\left(-\left(\phi_{B0} - \alpha\sqrt{V}\right)/k_B T\right) \quad (8.1)$$

where k_B is the Boltzmann constant, T is the absolute temperature, ϕ_{B0} is the zero bias potential barrier height at metal/oxide interface, α is the barrier lowering factor, A^* is the Richardson constant and A is the device area. For both bias polarities the experimental data for a given electric field (V) exhibits a linear trend on a $\ln(I/T^2)$ vs $1000/T$ plot as shown in **Figs. 8.3(b-c)**. The slope of these curves yields an activation energy corresponding to the

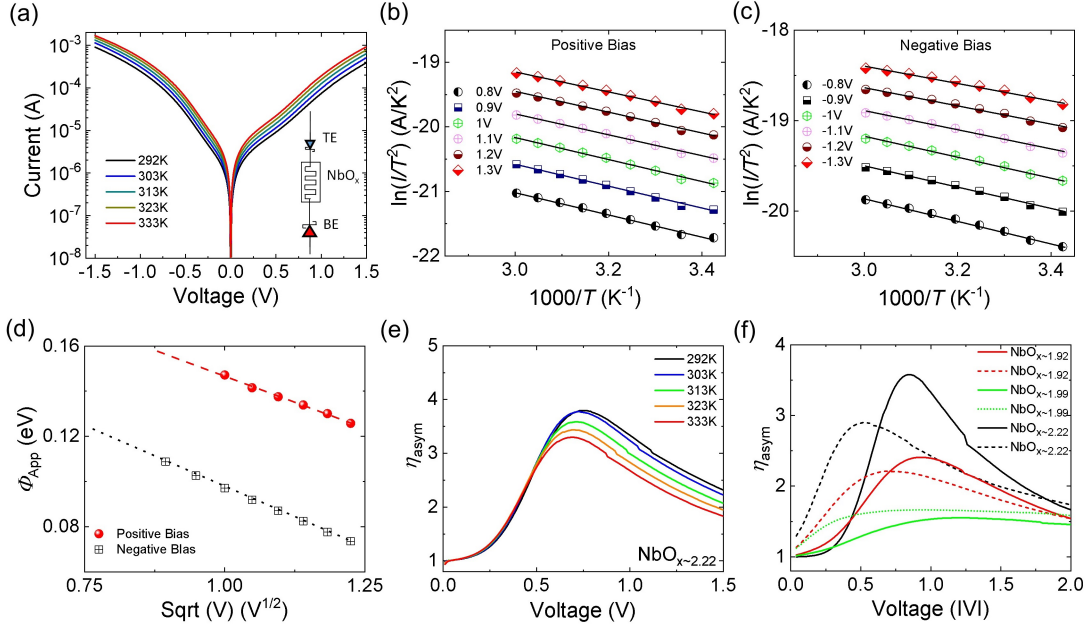


Figure 8.3: (a) Temperature dependent I-V characteristics of a typical sub-stoichiometric NbO_x device ($x = 2.22$), equivalent circuit element is shown inset, (b-c) signature plots confirming thermionic emission as the major mechanism for Nb top and Pt bottom electrodes ($x = 2.22$), (d) extraction of zero bias potential barrier at top and bottom interfaces for a typical sub-stoichiometric NbO_x ($x = 2.22$) device, (e) asymmetry plot of the data presented in Fig. 8.3(a), current asymmetry η_{asym} is defined as the ratio of device current under negative bias to that under positive bias ($I_{negative}/I_{positive}$), and (f) current asymmetry before and after electroforming for devices with different oxide stoichiometry. The dashed lines in Fig.8.3 (f) represent the experimental data after electroforming and the smooth lines are the experimental data of the corresponding devices before electroforming.

apparent potential barrier at the particular applied field (corresponding to V),

$$E = \phi_{App} = \phi_{B0} - \alpha\sqrt{V} \quad (8.2)$$

The obtained values were found to decrease with increasing applied bias, as expected from equation (8.2) and the zero-bias barrier heights were determined to be 0.19 eV and 0.24 eV for negative and positive bias, respectively (**Fig. 8.3(d)**). These include contributions from the electrodes and the oxide film and consequently, they serve as a measure of the resistance asymmetry, rather than actual metal/oxide barrier heights.

The resistance asymmetry is represented more clearly by plotting the ratio of currents measured under negative and positive bias as a function of absolute voltage, as shown for the Nb/NbO_{2.22}/Pt device in **Fig. 8.3(e)**. This shows that the current ratio (asymmetry) initially increases with increasing voltage before reaching a maximum at ~ 0.75 V. Asym-

metry then decreases as voltage increases further before saturating at a value between 1 and 2. This behaviour is attributed to the dominance of Schottky emission at low fields and an increasing contribution from Poole-Frenkel conduction at higher fields as previously reported for Nb_2O_5 -based Schottky diodes [272]. Significantly, the high-field asymmetry is maintained for all sub-stoichiometric NbO_x films even after electroforming (**Fig. 8.3(f)**). This reflects the fact that the Schottky barriers in the shell area surrounding the filamentary region remain unaffected and continue to influence the current distribution in the devices.

8.5 Effect of oxide stoichiometry and device scaling

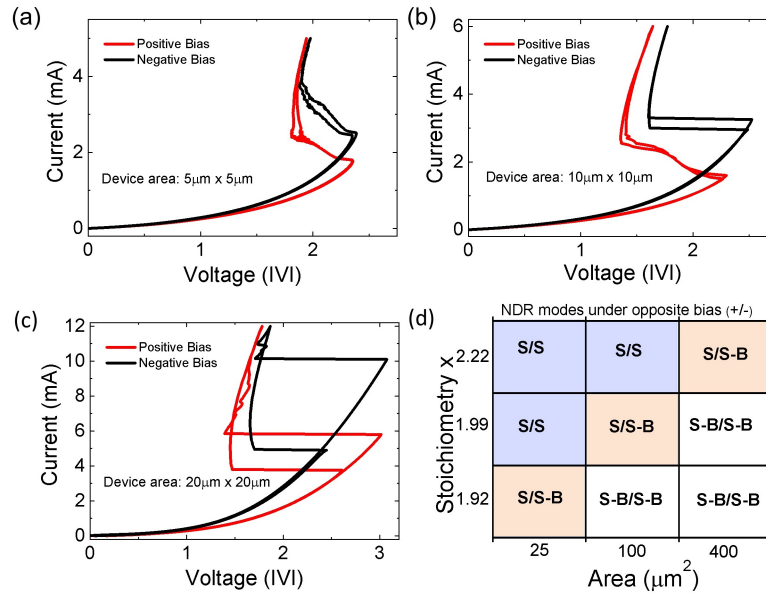


Figure 8.4: (a-c), Polarity dependent NDRs observed in $\text{Nb}/\text{NbO}_x \sim 1.99/\text{Pt}$ MOM cross-point devices with $5\mu\text{m} \times 5\mu\text{m}$, $10\mu\text{m} \times 10\mu\text{m}$ and $20\mu\text{m} \times 20\mu\text{m}$ active area, and (d) matrix representation of dependency of S-type and snapback NDR as a function film stoichiometry, device area and bias polarity. The notations S/S and SB/SB are used for S-type NDR and snapback NDR respectively under subsequent opposite polarity biasing conditions, while S/S-B is used to indicate S-type NDR under positive bias and snapback NDR under negative bias.

The film stoichiometry and device area have a direct impact on the resistance of the shell region surrounding the electroformed filament and therefore affect the NDR characteristics. As a consequence, the behaviour reported in **Fig. 8.1** is not universal but is specific to devices with particular combinations of device area and film stoichiometry. A systematic study of these dependencies showed that the smallest area devices ($2\mu\text{m} \times 2\mu\text{m}$) displayed smooth S-type NDR under both positive and negative biasing regardless of film stoichiometry.

etry. In contrast, larger area devices exhibited one of three behaviours depending on the stoichiometry of the oxide film: dual S-type characteristics (**Fig. 8.4(a)**), combined S-type and snapback characteristics (**Fig. 8.4(b)**) or dual snapback characteristics (**Fig. 8.4(c)**). These dependencies are summarised in **Fig. 8.4(d)** which clearly highlights the three distinct regimes. Note that, higher sub-threshold and threshold currents were always observed for negative bias polarity, consistent with higher contact resistance from the reverse biased Pt/NbO_x interface.

8.6 Modelling of asymmetric NDR characteristics

Fig. 8.4 shows that the NDR characteristics of simple two-terminal MOM devices are sensitive to the relative resistances of the filamentary conduction path and the surrounding device area, including the effects of polarity dependent contact resistance at the metal/oxide contacts. While the dependencies appear complex, they can be understood with reference to the recently developed parallel-memristor or core-shell model of NDR [152] that includes both filamentary conduction and conduction in the surrounding oxide film (**Fig. 8.6**) (details of this model is discussed in **Chapter 3**).

For the case where the parallel resistance R_S is independent of bias polarity, the above model predicts either smooth S-type or abrupt snapback characteristics under both positive and negative bias, depending on whether $R_S > |R_{NDR}|$ or $R_S < |R_{NDR}|$. However, when R_S is polarity dependent it is necessary to consider three distinct scenarios. Assuming that $R_S = R_p$ under positive bias and $R_S = R_n$ under negative bias and that $R_p > R_n$ one needs to specifically consider the three following cases: i) for $R_p > R_n > R_{NDR}$, S-type characteristics are expected under both positive and negative bias, as shown in **Fig. 8.4(a)**; ii) for $R_{NDR} > R_p > R_n$, snapback characteristics are expected under both positive and negative bias, as shown in **Fig. 8.4(c)**; and iii) for $R_p > R_{NDR} > R_n$, snapback NDR are expected under negative bias and a smooth S-type NDR under positive bias, as observed in **Fig. 8.4(b)**. The simple criterion defined by the core-shell model therefore provides the basis for understanding the polarity dependent switching characteristics and its dependence on film stoichiometry and device area. In this context it is interesting to note that the current asymmetry is almost negligible in stoichiometric Nb₂O₅ as the film resistance in the shell region is much higher than the interface resistance ($R_{\text{film}} \gg R_{(\text{int.})}$). As a consequence, these devices showed symmetric S-type NDR (see **Appendix**) as well as symmetric sub-threshold and threshold switching parameters under positive and negative bias (also see **Fig. 8.5**).

Device characteristics were simulated using an LT-SPICE model of the circuit shown in **Fig. 8.6(b)**, where the interface resistance is represented by a Schottky contact [Equation

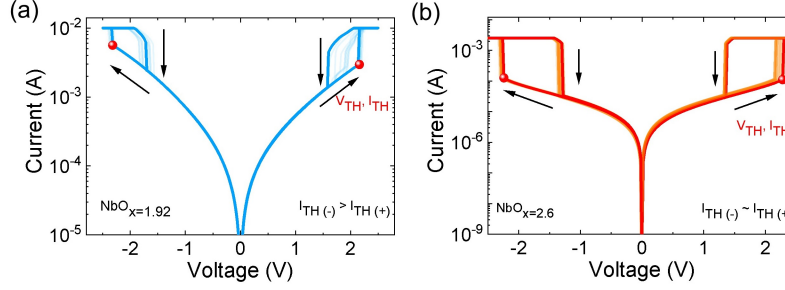


Figure 8.5: (a-b): Asymmetric and symmetric threshold switching depending on oxide stoichiometry.

(8.1)], and the core and shell resistances are attributed to Poole-Frenkel conduction, and represented by equations of the form [229]:

$$R_m = R_0 \cdot \exp \left(\left(E_{ac} - q \sqrt{\frac{qE}{\pi \epsilon_0 \epsilon_r}} \right) / k_B T \right) \quad (8.3)$$

where, k_B denotes the Boltzmann constant, E_{ac} is the activation energy, ϵ_0 is the vacuum permittivity, and ϵ_r is the relative permittivity of the threshold switching volume and surrounding NbO_x film. T_m and T_{amb} denote the temperature of the electrically active region and the ambient environment, R_0 is the resistance pre-factor of the active region at $T=T_{amb}$.

The dynamic behaviour of the memristor is defined by Newton's law of cooling:

$$\frac{dT_m}{dt} = \frac{(I_m)^2 R_m}{C_{th}} - \frac{\Delta T}{R_{th} C_{th}} \quad (8.4)$$

where R_{th} and C_{th} are the thermal resistance and the thermal capacitance of the device, and ΔT is the temperature difference between the T_m and T_{amb} .

Details of the model parameters are given in the **Table-8.1**.

Using this model, the I-V characteristics of devices were calculated as a function of film and interface resistance, as shown in **Figs. 8.6(c) and 8.6(d)**, respectively. The data clearly demonstrate the transition from smooth S-type to abrupt snapback NDR characteristics as the shell resistance is reduced, and more detailed analysis confirms that this occurs at R_{NDR} . Significantly, a difference in Schottky barrier height of as little as ~ 0.03 eV is shown to be sufficient to cause such a transition (**Fig. 8.6(d)**).

Table 8.1: Memristor parameters used in the simulation for core memristor and shell resistance .

Model Parameters	Symbol	Threshold Switch (Core)	Surroundings (Shell)	Schottky parameters
Thermal capacitance (JK^{-1})	C_{th}	1×10^{-15}		
Resistance pre-factor (Ω)	R_0	80	0.01 to 1	
Thermal resistance (KW^{-1})	R_{th}	2×10^5	2×10^5	
Ambient temperature (K)	T_{amb}	298	298	
Activation Energy (eV)	E_{ac}	0.23	0.23	
Relative permittivity	ϵ_r	45	45	
Film thickness (nm)	t	45	45	
Richardson's constant ($\text{AK}^{-2}\text{m}^{-2}$)	A^*			480
Barrier lowering factor (\sqrt{eV})	α			0.24
Zero bias barrier (eV)	ϕ_{B0}			0.3 to 1
Schottky diode area (m^2)	A			2.48×10^{-11}

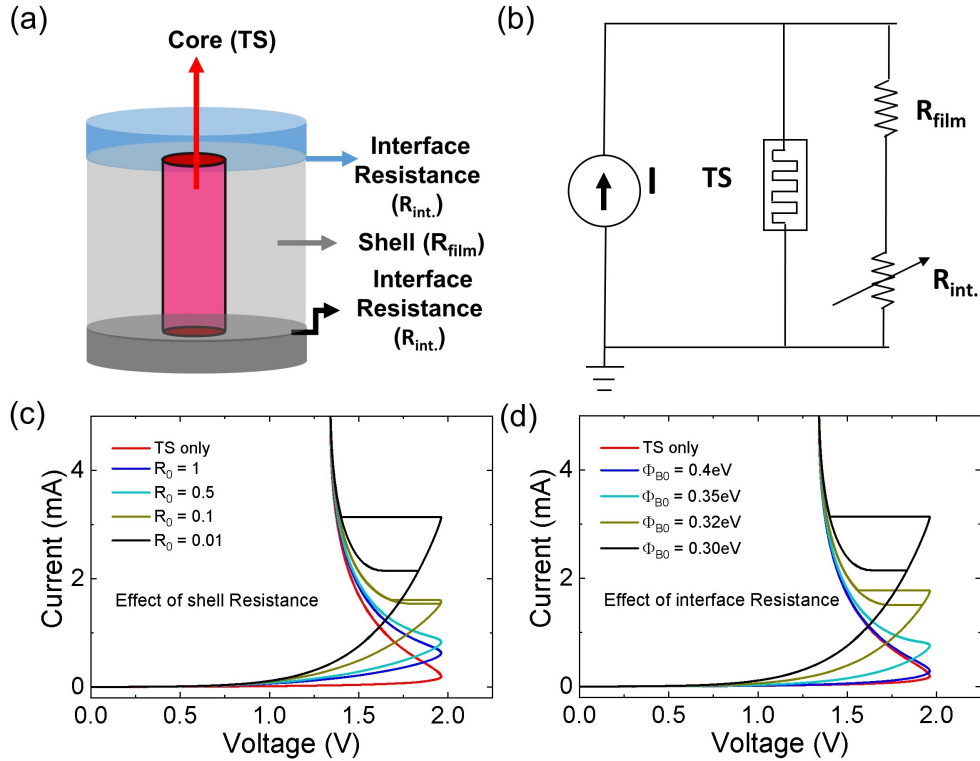


Figure 8.6: (a) Schematic of the core-shell model of memristor, (b) circuit model showing a threshold switch (TS) as the core element, a variable resistor indicating the interface resistances at the metal-oxide interfaces and R_{film} represents the oxide resistance in the shell area, which is modelled by the Poole-Frenkel equation, (c) effect of shell resistance on the NDR response, (d) effect of interface resistance (as a function of increasing barrier heights) on the NDR response when the shell resistance (R_{film}) is fixed for a given device area, thickness and oxide stoichiometry. Note that for opposite polarity biasing one interface becomes forward-biased and the other becomes reverse-biased and vice versa, as a result the interface resistance experiences significant change when the polarity is reversed.

8.7 Summary

The results of **Chapter 8** demonstrate polarity dependent negative differential resistance characteristics in Nb/NbO_x/Pt cross-point devices and show that the observed asymmetry is a direct consequence of the Schottky barriers created by the metal/oxide contacts. Three distinct behaviours were observed under opposite polarity testing depending on the stoichiometry of the oxide film and device area: bipolar S-type NDR, bipolar snapback NDR, and combined S-type and snapback NDR. By combining results from current-controlled electrical measurements and in-situ thermoreflectance imaging, it is shown that these NDR responses are associated with strong current localisation within the device. This was used to justify the use of a previously developed two-zone, core shell thermal model of the device. The ob-

served polarity dependent NDR responses, and their dependence on stoichiometry and area were then explained by extending this model to include the effect of the polarity dependent contact resistance.

Conclusion and outlook

9.1 Summary and Conclusion

This thesis has investigated the filamentary nature of threshold switching in metal/oxide/metal cross-point devices using a range of amorphous niobium oxide thin films (NbO_x with x between 1.92 and 2.6). The electroforming process and the post-forming threshold switching response have been extensively explored with a particular focus on the underlying physical mechanism. A comprehensive understanding of the oxide composition, metal/oxide interfacial phenomena and device geometry in determining different threshold switching modes has been achieved.

In **Chapter 1** and **Chapter 2**, the research motivation and background for investigating memristive switching in MOM devices were presented with a particular emphasis on niobium oxides. The experimental techniques, such as thin films growth, device fabrication, and characterisation were introduced in **Chapter 3**. This chapter also included a simple two-zone parallel memristor model that can account for the diverse NDR responses observed in MOM structures.

In **Chapter 4**, the electroforming process in two-terminal MOM cross-point devices was investigated using amorphous NbO_x thin films. At first, a simple means of detection of conductive filaments was demonstrated which is based on thermal discolouration of a thin photoresist layer. Using this technique, spatial mapping of conductive filaments in micron-scale metal/oxide/metal cross-point devices was performed. A finite element model of steady state temperature distribution was developed which showed that adequate temperature to thermally degrade the photoresist can be obtained at the top-electrode/photoresist interface, and that the maximum temperature has a strong dependence on the top electrode thickness. The application of this technique to metal-oxide-metal cross-point devices con-

firmed that electroforming generally created one dominant filament and showed that for low conductivity stoichiometric NbO_x film filament formation was heterogeneous, with filaments preferentially forming along the edge of the top electrode. TEM analysis of the top and bottom electrode edges suggested that this was due to a reduction of the effective oxide thickness in this region. In contrast, spatial mapping of filament distribution in the high-conductivity (sub-stoichiometric) NbO_x film is localised around the centre of the device and no filaments were detected at the electrode edges even though the electrode geometry is similar to that for the low-conductivity films. The former was found to be typical of field-induced dielectric breakdown in stoichiometric oxide films while the latter was found to represent a new mode of electroforming. In the latter case, in-situ temperature mapping and finite element modelling showed that this mode of electroforming was mediated by a current bifurcation process in which the current distribution is separated into regions of low and high current density and produced a highly localised temperature distribution in the film. These results clearly demonstrate two distinct modes of electroforming in the same material system and show that the dominant mode depends on the conductivity of the film, with field-induced electroforming dominant in low-conductivity films and current bifurcation-induced electroforming dominant in high-conductivity films.

In **Chapter 5** the role of metal/oxide interface reactions on the threshold switching response of metal/ Nb_2O_5 /Pt structures was studied. It was found that reactive electrodes improved the threshold switching reliability and the device characteristics were influenced by the choice of electrode metal. Specifically, devices with Nb and Ti electrodes exhibited symmetric threshold switching under positive and negative bias, devices with Cr electrodes exhibited asymmetric switching with a smaller hysteresis window under positive bias than under negative bias, and devices with Hf and Ta electrodes exhibited a hybrid threshold-memory (1S1M) response. Using thermodynamic analysis and lumped element modelling, these characteristic changes in the device response was attributed to the nature of the interlayer formed by reaction of electrode metals with the underneath functional Nb_2O_5 layer. Specifically, changes in interlayer resistance due to field-induced oxygen exchange was shown to be consistent with the observed device behaviour. Significantly, Pt/ Nb_2O_5 /Pt devices exhibited unipolar switching rather than threshold switching, clearly demonstrating the role of the reactive electrodes in mediating the threshold switching response. These results provide important insight into the physical origin of the switching response including symmetric and asymmetric threshold switching hysteresis and provide pathways for engineering devices with reliable switching characteristics.

A systematic comparison of the threshold switching response in undoped and Ti-doped Nb_2O_5 -based cross-point devices was carried out in **Chapter 6**, which clearly demonstrated

that Ti-doping provides a convenient means to improve device reliability and uniformity. Furthermore, these results demonstrated the ability to tune threshold switching parameters including threshold and hold voltages, threshold switching window (hysteresis) and maximum negative differential resistance. Systematic changes in the threshold switching parameters were demonstrated for Ti/Nb fractions up to 0.31. However, at higher Ti/Nb fractions (i.e., 0.72) the devices no longer exhibited NDR, but the current-voltage characteristics were non-linear within the investigated current range. By correlating the results from temperature dependent electrical measurements with a lumped element modelling, these effects were understood by the reduction in the device resistance and its rate of change with temperature, where the latter was characterised by an effective thermal activation energy. Significantly, this analysis also demonstrated that a critical activation energy is required to produce negative differential resistance. These results provide an improved understanding of the physical mechanisms responsible for S-type NDR characteristics and provide new insight for engineering devices for specific applications.

The physical origin of the discontinuous snapback response is investigated in **Chapter 7**. Specifically, it was demonstrated that the NDR response of NbO_x-based cross-point devices can be controlled by the oxide conductivity, area, thickness and temperature. Additionally, it was shown that the snapback mode of NDR is associated with redistribution of current from low to high current-density domains in a manner consistent with the proposed core-shell model of current transport. In-situ temperature mapping demonstrated that the snapback response is associated with current localisation, either due to a pre-existing permanent filament or current bifurcation, and the redistribution of current between low and high current-density domains. This was further correlated with NDR characteristics which exhibited a systematic transition from S-type to snapback NDR depending on the conductivity, area, thickness and temperature of the NbO_x film. These results conclusively demonstrated that the snapback characteristic is a generic response of materials with a strong temperature dependent conductivity and that it has the same physical origin as the S-type NDR characteristic but arises from a non-uniform current distribution and the redistribution of current from regions of low to high current density.

This understanding was further justified in **Chapter 8** where a polarity dependent negative differential resistance characteristic in Nb/NbO_x/Pt cross-point devices is demonstrated. Three distinct behaviours were observed under opposite polarity testing depending on the stoichiometry of the oxide film and device area: bipolar S-type NDR, bipolar snapback NDR, and combined S-type and snapback NDR. By combining current-controlled electrical measurements and in-situ thermoreflectance imaging it was shown that these NDR responses are associated with strong current localisation within the device and that the observed asym-

metry is a direct consequence of the Schottky barriers created by the metal/oxide contacts existing in the surrounding non-filamentary region. The observed polarity dependent NDR responses, and their dependence on stoichiometry and area were then explained by extending the core-shell model to include the effect of the polarity dependent contact resistance. The observation of a polarity dependent combined S-type and snapback NDR in a single device is significant as this clearly justifies the use of the two-zone, core shell thermal model of the device. The findings in **Chapters 7 and 8** are particularly significant as these results clearly identify the physical origin of the discontinuous snapback response, thereby resolving a long-standing controversy.

Overall, the experimental findings correlated with model predictions included in this thesis advance the current understanding of threshold switching response in amorphous NbO_x films and provide a strong basis for engineering devices with specific NDR characteristics for neuromorphic computing and non-volatile memory applications. Significantly, these results explain the origin of different memristive switching modes including symmetric and asymmetric threshold switching hysteresis, controllability of S-type NDR and its dependence on device resistance and activation energy, and finally demonstrate the physical origin of the discontinuous snapback NDR response.

9.2 Future research

Threshold switching in NbO_x has great potential for application in emerging technologies and therefore, understanding the physical origin of the threshold switching is of great importance for further developments in this field. The studies presented in this thesis focussed on understanding the driving mechanism of threshold switching in NbO_x , which is of fundamental scientific and technological interests. Additionally, several parameters which control threshold switching in NbO_x were investigated. These results improve the understanding of device behaviour and may be used to engineer specific device properties for different applications. However, there are still multiple areas of investigation for future studies, as suggested below.

9.2.1 Detailed understanding of the nature of Nb/ Nb_2O_5 interface reactions and their effect on threshold switching

Thermodynamic analysis predicts a spontaneous reaction between Nb and Nb_2O_5 at the electrode/oxide interface and studies indicate that this has a significant impact on the switching behaviour and device reliability. Recent studies have also shown that the extent of the reaction depends on the relative thicknesses of the metal and oxide layers as well as the oxygen

affinity of the metal electrode [202, 214]. A systematic study including the effect of different metal and oxide thicknesses and the role of oxide composition in controlling the reaction yield can be further investigated by combining in-situ electrical measurement and compositional analysis.

9.2.2 Micro-structural analysis of the threshold switching volume

Metal/Niobium Oxide/Metal devices exhibit a wide range of threshold switching or negative differential resistance (NDR) characteristics including a continuous S-type NDR and a discontinuous snapback response. The threshold switching response is often observed after an initial electroforming step which leads to a local compositional change and/or modification of the Schottky barriers at the metal/oxide interfaces. Additionally, the local joule heating associated with filamentary conduction can initiate a temperature-induced local crystallisation (depending on the operating condition) which may significantly influence the device response [78]. Therefore, further studies are required to investigate current induced compositional changes in the filamentary region and correlate this with in situ current-voltage measurement and temperature mapping. Although direct implementation of these analyses is extremely complex and often inconclusive, these measurements will help to further advance the understanding.

9.2.3 Understanding the composite NDR characteristics observed in NbO_x and investigate their dynamical characteristics

This thesis has mainly investigated the smooth S-type and discontinuous snapback characteristics and advances the understanding of their physical origin. However, more complex NDR responses including combined S-type and snapback, dual S-type and dual snapback responses are also observed in NbO_x -based devices [152]. Thus, the observation of different types of NDRs clearly demonstrates that the switching behaviour in niobium oxide is not straightforward and further systematic study is needed to reveal the full mechanism. In this context, it is interesting to note that these complex/composite NDR modes can be explained within the framework of the proposed two-zone, parallel memristor model by considering that both the core and shell regions have temperature dependent conductivities that can be represented by two parallel threshold-switching memristors [152] as discussed in **Chapter 3**. Importantly, these complex NDRs have the potential to provide new functionalities for emerging neuromorphic computing applications as demonstrated in recent studies [49, 151]. Future systematic study is required to fully understand the complex responses, develop protocols to achieve controllable characteristics and understand their oscillation dynamics.

Finally, the above understanding of the electroforming process and the subsequent threshold switching characteristics can be further explored in two-terminal MOM structures based on other strongly correlated oxides, including VO_x [71, 261–264], TiO_x [74] and TaO_x [73, 195] that also exhibit the volatile threshold switching response.

Appendix

A.1 Parameters used in the simulation of the parallel-memristor model in Chapter 3

Table A.1: Memristor parameters used in the simulation for core memristor and shell resistance where both are represented by similar threshold switches with slightly different parameters.

Model Parameters	Symbol	R_{m1} Value	R_{m2} Value
Thermal capacitance (JK^{-1})	C_{th}	1×10^{-15}	1×10^{-15}
Resistance pre-factor (Ω)	R_0	25 to 75	25
Thermal resistance (KW^{-1})	R_{th}	1.3×10^5 to 1×10^6	2.2×10^5 to 1×10^6
Ambient temperature (K)	T_{amb}	296.15	296.15
Activation Energy (eV)	E_{ac}	0.215	0.215 to 0.255
Relative permittivity	ϵ_r	45	45
Film thickness (nm)	t	20 to 30	50 to 125

A.2 Further example of edge effect in MOM structures

To further clarify the edge effect described in **Chapter 4**, additional cross-sectional TEM images of the bottom electrode of a Pt/HfO₂/Pt/Ti/SiO₂/Si structure is demonstrated in **Fig. A.1**. This clearly shows that the bottom Pt layer extends beyond the Ti adhesion layer in the undercut region.

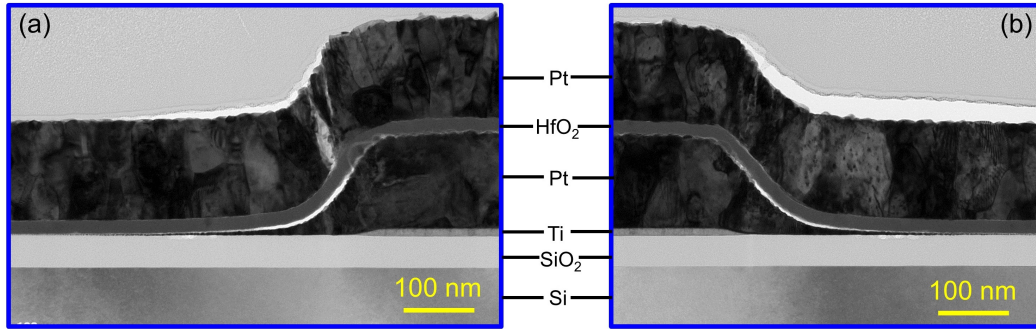


Figure A.1: (a-b): The undercut effect in Pt/HfO₂/Pt/Ti/SiO₂/Si structure is clearly observed in the left and right edges of bottom electrode.

A.3 Forming voltage distribution for low- and high- conductivity NbO_x films

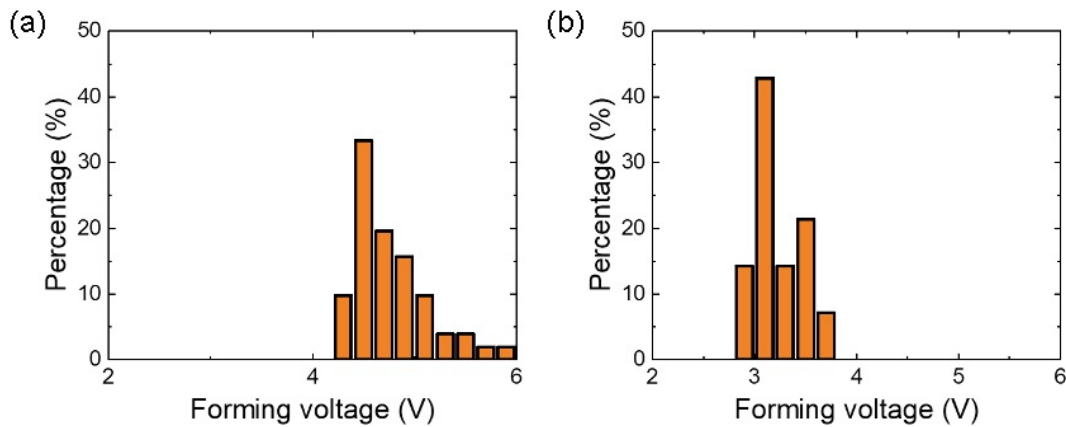


Figure A.2: Histogram of forming voltage of (a) low-conductivity- stoichiometric NbO_x (x = 2.6) and (b) high-conductivity- sub-stoichiometric NbO_x (x = 1.92) films.

A.4 Polarity dependent current-controlled responses in reactive metal/ Nb_2O_5 /Pt

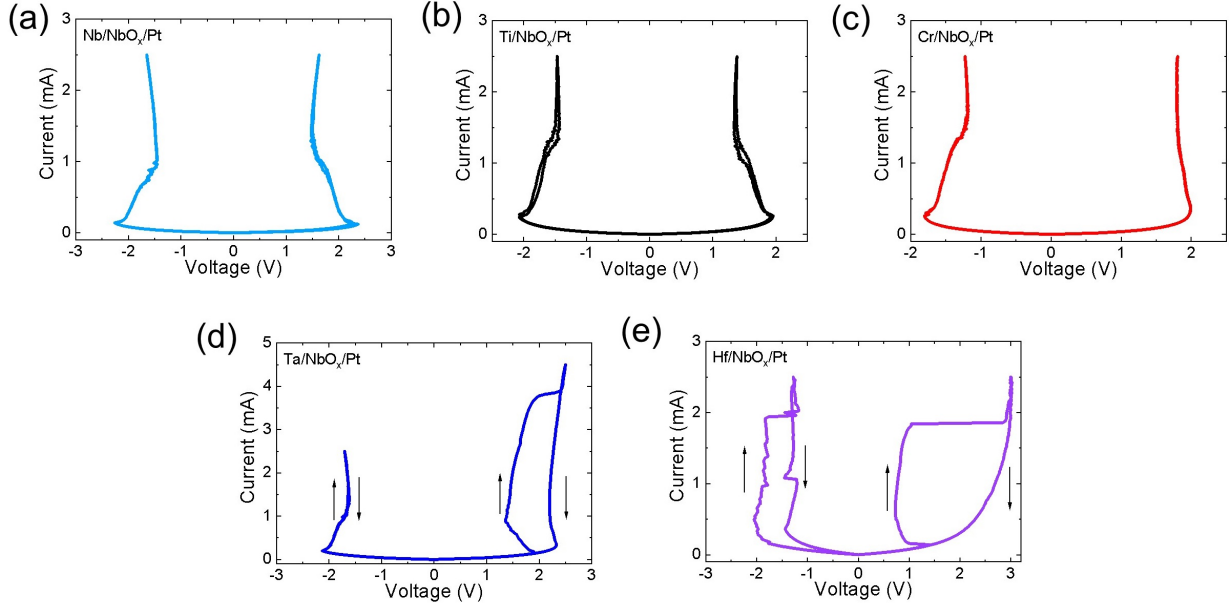


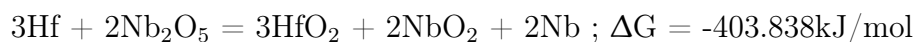
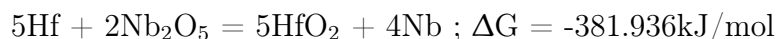
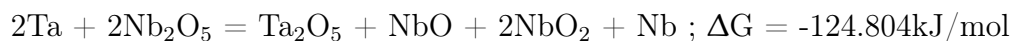
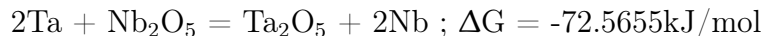
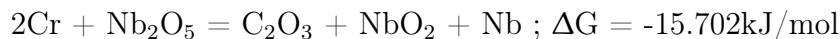
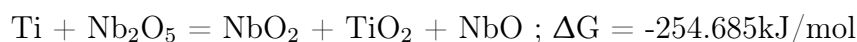
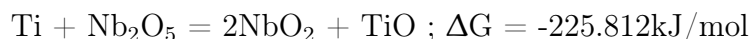
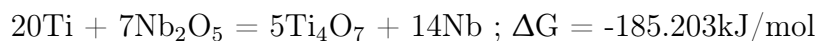
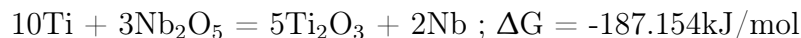
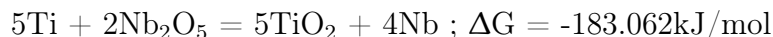
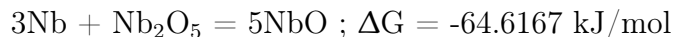
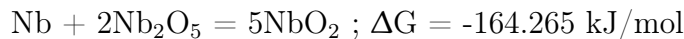
Figure A.3: Effect of polarity reversal on the current-controlled switching in typical devices with (a) Nb, (b) Ti, (c) Cr, (d) Ta and (e) Hf top electrodes respectively.

A.5 List of Possible Reactions at 298.15K using thermodynamic analysis

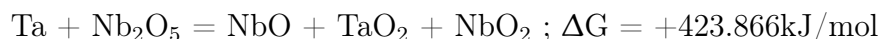
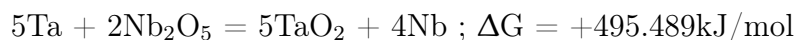
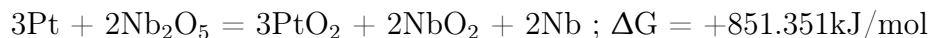
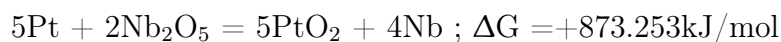
Table A.2: Thermochemical data extracted from Ref. [252].

Oxide	ΔG (kJ/mol)	Oxide	ΔG (kJ/mol)	Oxide	ΔG (kJ/mol)
NbO	-391.942	NbO ₂	-739.197	Nb ₂ O ₅	-1765.86
HfO ₂	-1088.28	PtO ₂	166.909	TaO	163.535
TaO ₂	-210.855	Ta ₂ O ₅	-1910.991	TiO	-513.278
TiO(g)	24.534	TiO ₂	-889.406	TiO ₂ (A)	-883.266
Ti ₂ O ₃	-1433.824	Ti ₃ O ₅	-2317.294	Ti ₄ O ₇	-3213.016
Cr ₂ Nb	-20.92	CrO	154.573	CrO ₂	-544.9
CrO ₂ (g)	-87.369	CrO ₃	-512.562	CrO ₃ (g)	-273.444
Cr ₂ O ₃	-1058.067				

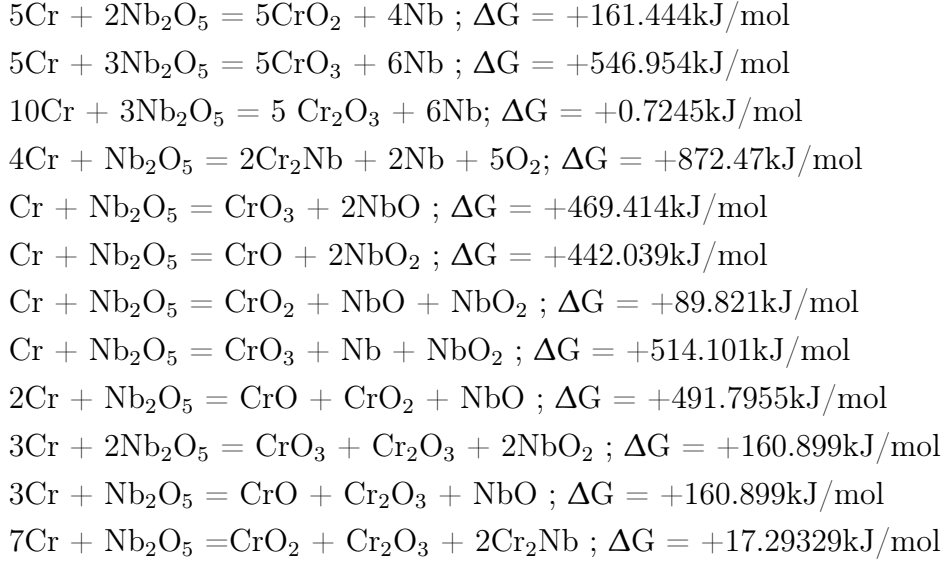
Possible Reactions at 298.15K with negative ΔG



Reactions at 298.15K with positive ΔG



A.6. Device-to-device and cycle-to-cycle variability: threshold switching parameters of undoped and Ti-doped Nb₂O₅ devices



A.6 Device-to-device and cycle-to-cycle variability: threshold switching parameters of undoped and Ti-doped Nb₂O₅ devices

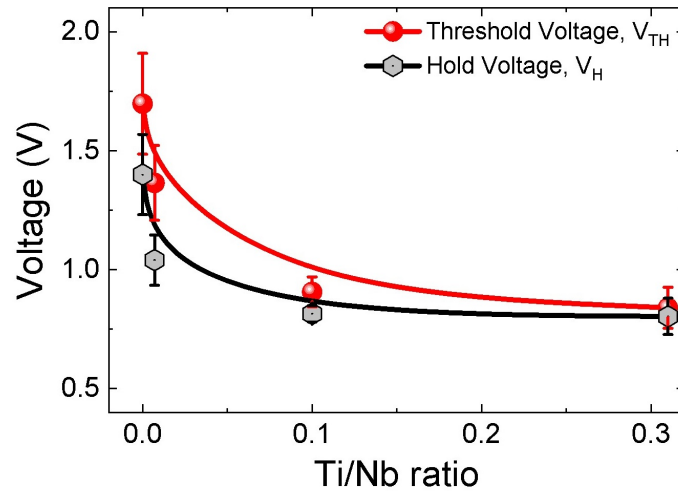


Figure A.4: Device-to-device variability: Variation of threshold and hold voltages for devices with undoped and Ti-doped Nb₂O₅ films (V_{TH} and V_H were extracted from current-controlled NDR for 12 devices in each case). The error bars represent standard deviation from the mean value

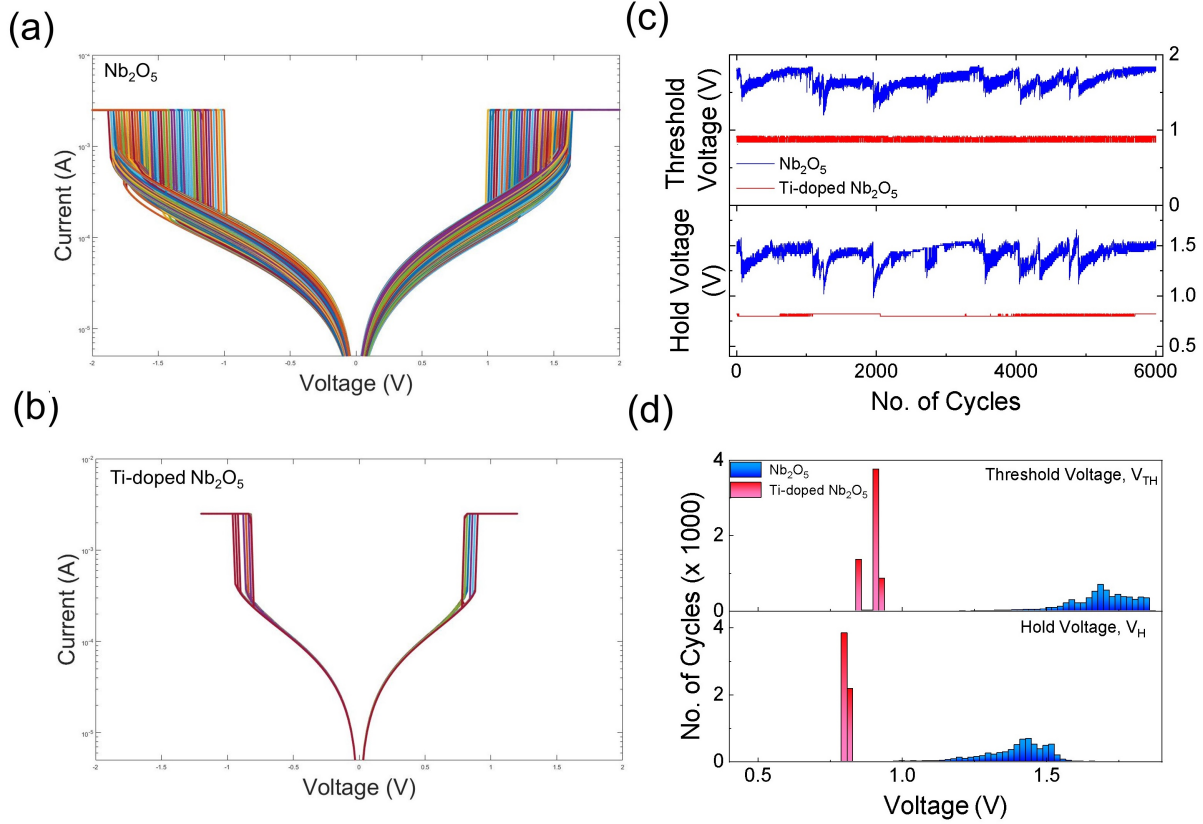


Figure A.5: (a-b) Cycle-to-cycle variability: (a-b) voltage-controlled threshold switching of $20\ \mu\text{m} \times 20\ \mu\text{m}$ cross-point devices with Nb_2O_5 and $\text{Ti:Nb}_2\text{O}_5$ ($\text{Ti/Nb} \sim 0.1$) thin films respectively (6000 consecutive switching cycles are shown for each case). (c) Variation of threshold and hold voltages for two identical devices with Nb_2O_5 and $\text{Ti:Nb}_2\text{O}_5$ films respectively (V_{TH} and V_{H} were extracted from ~ 6000 consecutive threshold switching cycles in each case), and (d) histograms showing the data plotted in (c).

A.7 Bipolar resistive switching observed in $\text{Ti}/\text{TiO}_2/\text{Pt}$ structures

TiO_2 devices exhibited bipolar resistive switching after repeated positive and negative voltage sweeps as shown in **Fig. A.6**.

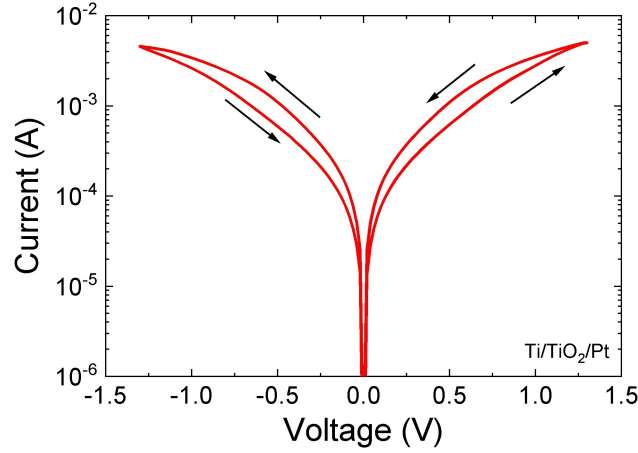


Figure A.6: Bipolar memory switching observed in a $\text{Ti/TiO}_2/\text{Pt}$ device.

A.8 Switching dynamics of undoped Nb_2O_5 and $\text{Ti:Nb}_2\text{O}_5$ ($\text{Ti/Nb} \sim 0.1$) devices

The switching dynamics of selected Nb_2O_5 and $\text{Ti:Nb}_2\text{O}_5$ ($\text{Ti/Nb} = 0.1$) devices were also investigated, as shown in **Figs. A.7** and **A.8**. For switching-time measurements, a square-wave voltage pulse of 10 μs duration was applied to the devices with an amplitude close to the corresponding threshold voltages ($V_{\text{TH}} \sim 1.68$ V for Nb_2O_5 and ~ 1.02 V for $\text{Ti:Nb}_2\text{O}_5$ ($\text{Ti/Nb} = 0.1$) devices, respectively) (**Fig. A.7**). The measured delay time τ_{delay} was found to decrease rapidly with increasing voltage, as shown in **Fig. A.7(f, i)**. This is consistent with a temperature-controlled switching process in which the delay time reflects the time to reach the threshold temperature [273]. The ‘switch on’ (τ_{on}) and ‘switch off’ (τ_{off}) times were found to be less sensitive to the applied voltage, with τ_{on} for an Nb_2O_5 device decreasing from ~ 380 ns for a pulse amplitude of 1.66 V to ~ 180 ns for a pulse amplitude of 1.8 V and decreasing from ~ 150 ns (for a pulse amplitude of 1.009 V) to ~ 100 ns (for a pulse amplitude of 1.05 V) for a $\text{Ti:Nb}_2\text{O}_5$ ($\text{Ti/Nb} = 0.1$) device. The magnitude of τ_{off} was similar for the two devices and varied between 45 ns and 70 ns for the above voltage ranges.

Oscillator dynamics were measured using a simple Anson-Pearson oscillator circuit with a $4\text{k}\Omega$ load resistor (**Fig. A.8**) [48]. The $\text{Ti:Nb}_2\text{O}_5$ ($\text{Ti/Nb} = 0.1$) devices exhibited higher oscillation frequency (30 - 34 MHz) and lower energy/spike (minimum ~ 80 pJ) compared to the frequency (11 - 26 MHz) and energy/spike (minimum ~ 220 pJ) of Nb_2O_5 devices.

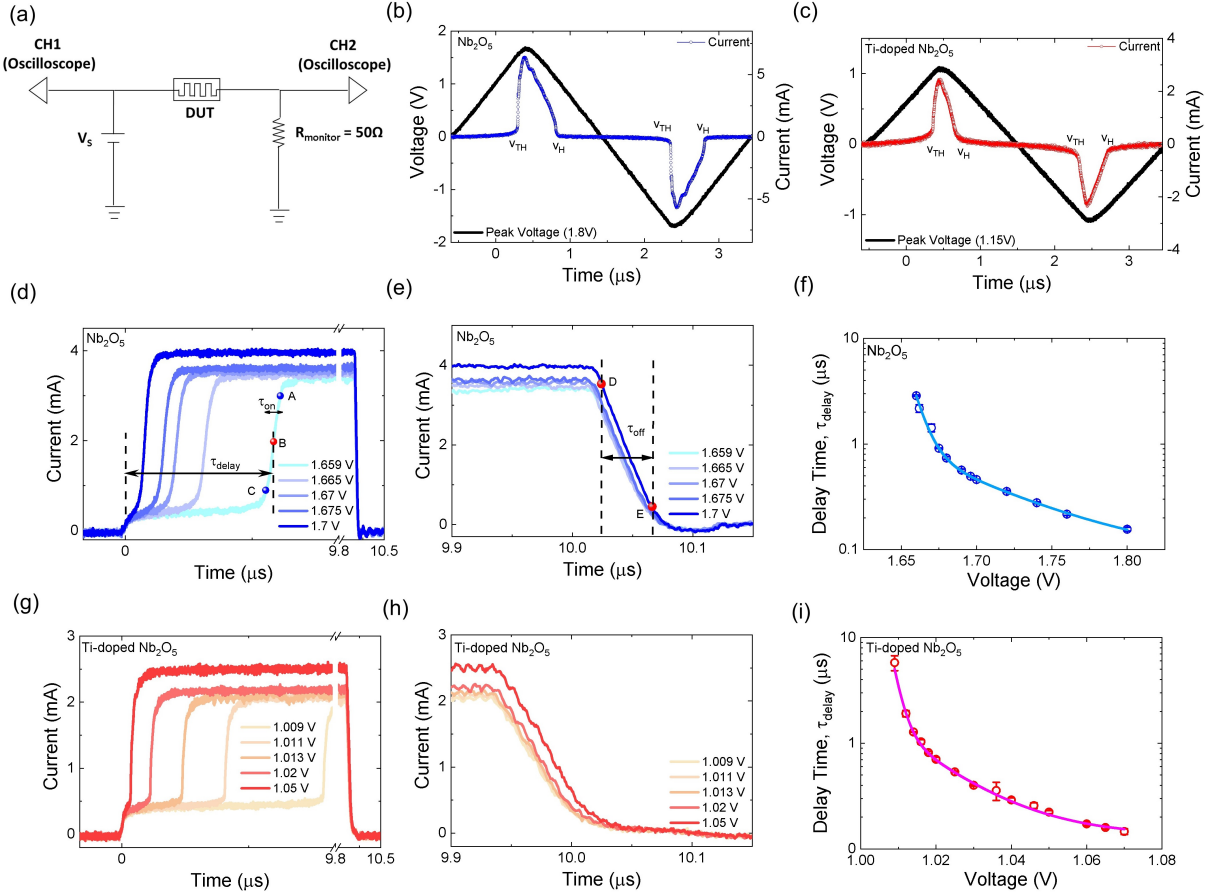


Figure A.7: (a) Schematic of the circuit used to measure dynamical characteristics, (b) switching cycles under triangular voltage pulse for devices with Nb_2O_5 and $\text{Ti:Nb}_2\text{O}_5$ films respectively, (d-f) switching time characteristics of a representative device with Nb_2O_5 , and (g-i) switching time characteristics of a representative device with $\text{Ti:Nb}_2\text{O}_5$ ($\text{Ti/Nb} = 0.1$). The ‘delay time’ (τ_{delay}) was defined as the time to reach 50% value of the low-to-high switching current across the device (indicated by point B in (d)); The ‘switch on’ time (τ_{on}) was defined as the time interval between the 10% and 90% value of the low-to-high switching current across the device (indicated by the time between points A and C in (d)); The ‘switch off’ time (τ_{off}) was defined as the time interval between 10% and 90% value of the high-to-low switching current across the device (indicated by the time between points D and E in (e)).

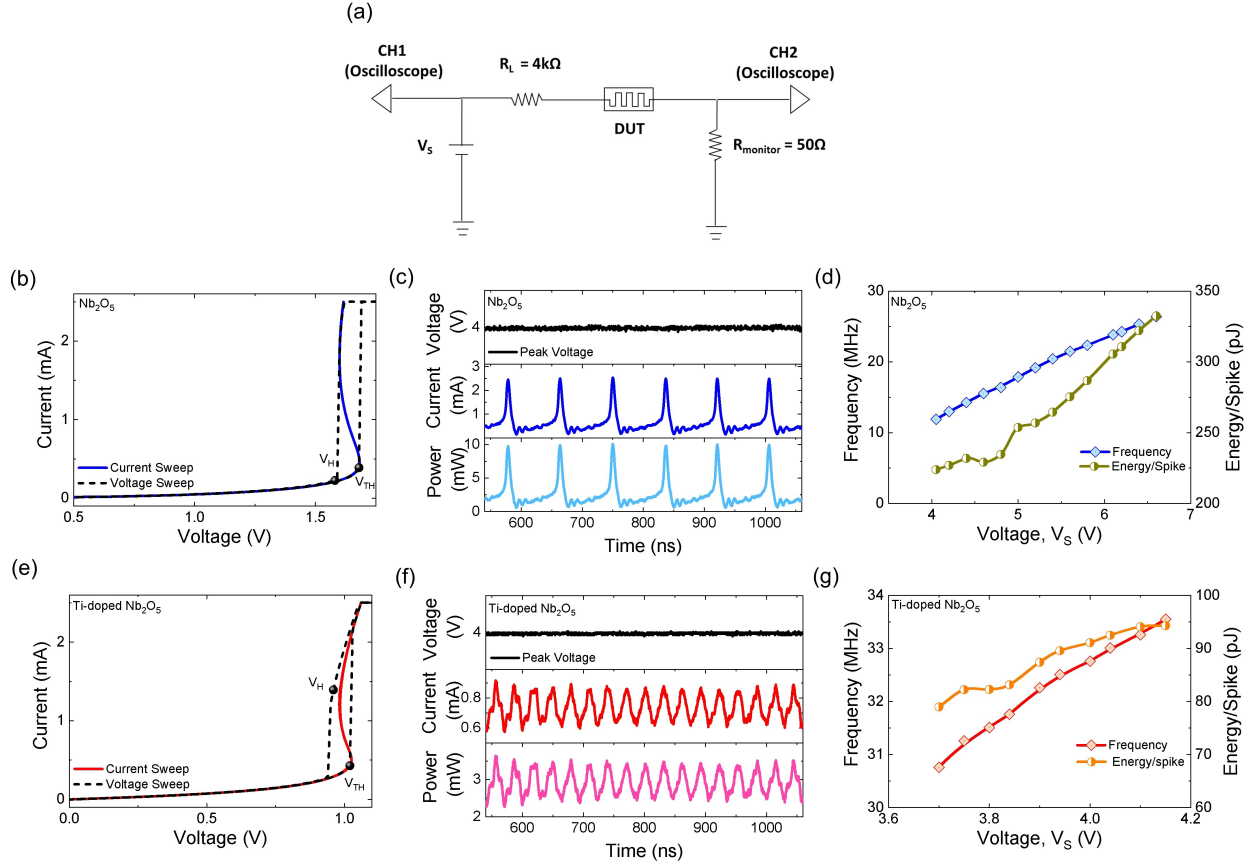


Figure A.8: (a) Schematic of the circuit used to measure oscillation dynamics, (b) measured threshold switching and current controlled NDR under quasi-static current-voltage measurements for a device with Nb_2O_5 film (b) measured oscillation waveform of the device current in the $50\text{ }\Omega$ resistor when a voltage pulse $\sim 4\text{ V}$ was applied for $3\text{ }\mu\text{s}$, (c) extracted oscillation frequency and energy/spike for the device with undoped Nb_2O_5 film, (d) measured threshold switching and current controlled NDR under quasi-static current-voltage measurements for a device with $\text{Ti:Nb}_2\text{O}_5$ film ($\text{Ti/Nb} \sim 0.1$), (e) measured oscillation waveform of the device current in the $50\text{ }\Omega$ resistor when a voltage pulse $\sim 4\text{ V}$ was applied for $3\text{ }\mu\text{s}$, and (f) extracted oscillation frequency and energy/spike for the device with $\text{Ti:Nb}_2\text{O}_5$ film ($\text{Ti/Nb} \sim 0.1$).

It is important to note that, the measured characteristics are largely limited by the device structure and parasitic contributions (e.g., capacitance and inductance from connecting cables, and parallel device resistance and capacitance) rather than the intrinsic properties of the oxide films [52]. Regardless, the higher oscillation frequency and lower energy/spike of the device with $\text{Ti:Nb}_2\text{O}_5$ clearly demonstrates the significance of lower threshold voltage and threshold switching hysteresis in controlling the oscillation dynamics of Nb_2O_5 -based devices [50].

A.9 Area and thickness dependent forming currents in the sub-stoichiometric NbO_x films

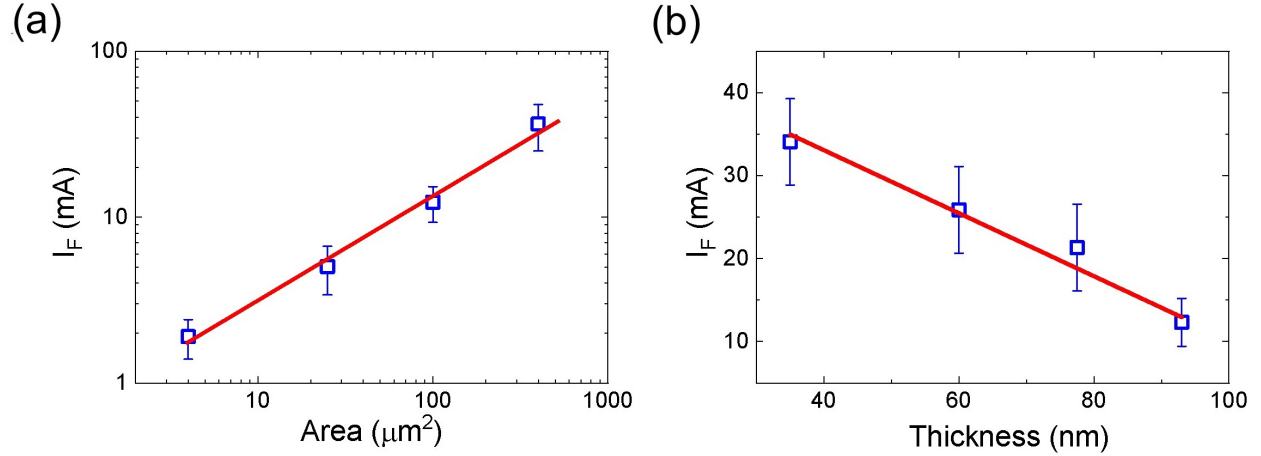


Figure A.9: Electroforming current (I_F) as a function of (a) cross-point device area and (b) oxide thickness for devices with sub-stoichiometric NbO_x films.

Bibliography

- [1] J. Von Neumann, “First draft of a report on the EDVAC,” *IEEE Annals of the History of Computing*, vol. 15, no. 4, pp. 27–75, 1993.
- [2] H. An, M. A. Ehsan, Z. Zhou, F. Shen, and Y. Yi, “Monolithic 3d neuromorphic computing system with hybrid CMOS and memristor-based synapses and neurons,” *Integration*, vol. 65, pp. 273–281, 2019.
- [3] V. Milo, G. Malavena, C. Monzio Compagnoni, and D. Ielmini, “Memristive and CMOS devices for neuromorphic computing,” *Materials*, vol. 13, no. 1, p. 166, 2020.
- [4] P. A. Merolla, J. V. Arthur, R. Alvarez-Icaza, A. S. Cassidy, J. Sawada, F. Akopyan, B. L. Jackson, N. Imam, C. Guo, and Y. Nakamura, “A million spiking-neuron integrated circuit with a scalable communication network and interface,” *Science*, vol. 345, no. 6197, pp. 668–673, 2014.
- [5] H. An, Z. Zhou, and Y. Yi, “Opportunities and challenges on nanoscale 3d neuromorphic computing system,” in *2017 IEEE International Symposium on Electromagnetic Compatibility & Signal/Power Integrity (EMCSI)*, pp. 416–421, IEEE, 2017.
- [6] L. Chang, D. J. Frank, R. K. Montoye, S. J. Koester, B. L. Ji, P. W. Coteus, R. H. Dennard, and W. Haensch, “Practical strategies for power-efficient computing technologies,” *Proceedings of the IEEE*, vol. 98, no. 2, pp. 215–236, 2010.
- [7] N. J. Schork, “Personalized medicine: time for one-person trials,” *Nature*, vol. 520, no. 7549, pp. 609–611, 2015.
- [8] D. Floreano and R. J. Wood, “Science, technology and the future of small autonomous drones,” *Nature*, vol. 521, no. 7553, p. 460, 2015.
- [9] E. R. Kandel, J. H. Schwartz, T. M. Jessell, S. A. Siegelbaum, and A. J. Hudspeth, *Principles of Neural Science*, vol. 4. McGraw-hill New York, 2000.

- [10] C. D. Wright, P. Hosseini, and J. A. V. Diosdado, “Beyond von-Neumann computing with nanoscale phase-change memory devices,” *Advanced Functional Materials*, vol. 23, no. 18, pp. 2248–2254, 2013.
- [11] G. Indiveri, B. Linares-Barranco, R. Legenstein, G. Deligeorgis, and T. Prodromakis, “Integration of nanoscale memristor synapses in neuromorphic computing architectures,” *Nanotechnology*, vol. 24, no. 38, p. 384010, 2013.
- [12] N. Shukla, A. Parihar, E. Freeman, H. Paik, G. Stone, V. Narayanan, H. Wen, Z. Cai, V. Gopalan, R. Engel-Herbert, *et al.*, “Synchronized charge oscillations in correlated electron systems,” *Scientific reports*, vol. 4, p. 4964, 2014.
- [13] S. Li, X. Liu, S. K. Nandi, D. K. Venkatachalam, and R. G. Elliman, “Coupling dynamics of Nb/Nb₂O₅ relaxation oscillators,” *Nanotechnology*, vol. 28, no. 12, p. 125201, 2017.
- [14] L. Luo, *Principles of Neurobiology*. Garland Science, 2015.
- [15] N. K. Upadhyay, H. Jiang, Z. Wang, S. Asapu, Q. Xia, and J. Joshua Yang, “Emerging memory devices for neuromorphic computing,” *Advanced Materials Technologies*, vol. 4, no. 4, p. 1800589, 2019.
- [16] G. Indiveri, B. Linares-Barranco, T. J. Hamilton, A. Van Schaik, R. Etienne-Cummings, T. Delbruck, S.-C. Liu, P. Dudek, P. Häfliger, S. Renaud, *et al.*, “Neuromorphic silicon neuron circuits,” *Frontiers in neuroscience*, vol. 5, p. 73, 2011.
- [17] M. Lee, S. W. Cho, S. J. Kim, J. Y. Kwak, H. Ju, Y. Yi, B.-k. Cheong, and S. Lee, “Simple artificial neuron using an ovonic threshold switch featuring spike-frequency adaptation and chaotic activity,” *Physical Review Applied*, vol. 13, no. 6, p. 064056, 2020.
- [18] H. Kim, S. Hwang, J. Park, S. Yun, J.-H. Lee, and B.-G. Park, “Spiking neural network using synaptic transistors and neuron circuits for pattern recognition with noisy images,” *IEEE Electron Device Letters*, vol. 39, no. 4, pp. 630–633, 2018.
- [19] G. W. Burr, R. M. Shelby, A. Sebastian, S. Kim, S. Kim, S. Sidler, K. Virwani, M. Ishii, P. Narayanan, A. Fumarola, *et al.*, “Neuromorphic computing using non-volatile memory,” *Advances in Physics: X*, vol. 2, no. 1, pp. 89–124, 2017.
- [20] J. Grollier, D. Querlioz, K. Camsari, K. Everschor-Sitte, S. Fukami, and M. D. Stiles, “Neuromorphic spintronics,” *Nature Electronics*, vol. 3, no. 7, pp. 360–370, 2020.

- [21] S. Oh, H. Hwang, and I. Yoo, “Ferroelectric materials for neuromorphic computing,” *APL Materials*, vol. 7, no. 9, p. 091109, 2019.
- [22] Z. Wang, S. Joshi, S. Savel’ev, W. Song, R. Midya, Y. Li, M. Rao, P. Yan, S. Asapu, Y. Zhuo, *et al.*, “Fully memristive neural networks for pattern classification with unsupervised learning,” *Nature Electronics*, vol. 1, no. 2, pp. 137–145, 2018.
- [23] M. Lanza, H.-S. P. Wong, E. Pop, D. Ielmini, D. Strukov, B. C. Regan, L. Larcher, M. A. Villena, J. J. Yang, L. Goux, *et al.*, “Recommended methods to study resistive switching devices,” *Advanced Electronic Materials*, vol. 5, no. 1, p. 1800143, 2019.
- [24] M. Hu, C. E. Graves, C. Li, Y. Li, N. Ge, E. Montgomery, N. Davila, H. Jiang, R. S. Williams, J. J. Yang, *et al.*, “Memristor-based analog computation and neural network classification with a dot product engine,” *Advanced Materials*, vol. 30, no. 9, p. 1705914, 2018.
- [25] Q. Cao, W. Lu, X. R. Wang, X. Guan, L. Wang, S. Yan, T. Wu, and X. Wang, “Non-volatile multistates memories for high-density data storage,” *ACS Applied Materials & Interfaces*, vol. 12, no. 38, pp. 42449–42471, 2020.
- [26] L. O. Chua, “Memristor-the missing circuit element,” 1971.
- [27] L. O. Chua and S. M. Kang, “Memristive devices and systems,” *Proceedings of the IEEE*, vol. 64, no. 2, pp. 209–223, 1976.
- [28] R. Tetzlaff, *Memristors and memristive systems*. Springer, 2013.
- [29] L. Chua, “If it’s pinched it’s a memristor,” *Semiconductor Science and Technology*, vol. 29, no. 10, p. 104001, 2014.
- [30] L. Chua, “Everything you wish to know about memristors but are afraid to ask,” in *Handbook of Memristor Networks*, pp. 89–157, Springer, 2019.
- [31] T. Hickmott, “Low-frequency negative resistance in thin anodic oxide films,” *Journal of Applied Physics*, vol. 33, no. 9, pp. 2669–2682, 1962.
- [32] K. Chopra, “Current-controlled negative resistance in thin niobium oxide films,” *Proceedings of the IEEE*, vol. 51, no. 6, pp. 941–942, 1963.
- [33] F. Argall, “Switching phenomena in titanium oxide thin films,” *Solid-State Electronics*, vol. 11, no. 5, pp. 535–541, 1968.

- [34] D. B. Strukov, G. S. Snider, D. R. Stewart, and R. S. Williams, “The missing memristor found,” *Nature*, vol. 453, no. 7191, pp. 80–83, 2008.
- [35] S. Vaidyanathan and C. Volos, *Advances in memristors, memristive devices and systems*, vol. 701. Springer, 2017.
- [36] A. Adamatzky and L. Chua, *Memristor networks*. Springer Science & Business Media, 2013.
- [37] L. Chua, “Resistance switching memories are memristors,” *Applied Physics A*, vol. 102, no. 4, pp. 765–783, 2011.
- [38] H.-Y. Chen, S. Brivio, C.-C. Chang, J. Frascaroli, T.-H. Hou, B. Hudec, M. Liu, H. Lv, G. Molas, J. Sohn, *et al.*, “Resistive random access memory (rram) technology: From material, device, selector, 3d integration to bottom-up fabrication,” *Journal of Electroceramics*, vol. 39, no. 1-4, pp. 21–38, 2017.
- [39] R. Waser, R. Dittmann, S. Menzel, and T. Noll, “Introduction to new memory paradigms: Memristive phenomena and neuromorphic applications,” *Faraday Discussions*, vol. 213, pp. 11–27, 2019.
- [40] J. Kim, Y. V. Pershin, M. Yin, T. Datta, and M. Di Ventra, “An experimental proof that resistance-switching memory cells are not memristors,” *Advanced Electronic Materials*, vol. 6, no. 7, p. 2000010, 2020.
- [41] Y. V. Pershin and M. Di Ventra, “Comment on ‘if it’s pinched it’s a memristor’,” *Semiconductor Science and Technology*, vol. 34, no. 9, p. 098001, 2019.
- [42] Y. Zhang, Z. Wang, J. Zhu, Y. Yang, M. Rao, W. Song, Y. Zhuo, X. Zhang, M. Cui, L. Shen, *et al.*, “Brain-inspired computing with memristors: Challenges in devices, circuits, and systems,” *Applied Physics Reviews*, vol. 7, no. 1, p. 011308, 2020.
- [43] I. Abraham, “The case for rejecting the memristor as a fundamental circuit element,” *Scientific reports*, vol. 8, no. 1, pp. 1–9, 2018.
- [44] M. D. Pickett, G. Medeiros-Ribeiro, and R. S. Williams, “A scalable neuristor built with Mott memristors,” *Nature Materials*, vol. 12, no. 2, pp. 114–117, 2013.
- [45] I. Messaris, R. Tetzlaff, A. Ascoli, R. Williams, S. Kumar, and L. Chua, “A simplified model for a NbO₂ Mott memristor physical realization,” in *IEEE International Symposium on Circuits and Systems (ISCAS)*, pp. 1–5, IEEE, 2020.

- [46] W. Yi, K. K. Tsang, S. K. Lam, X. Bai, J. A. Crowell, and E. A. Flores, “Biological plausibility and stochasticity in scalable VO₂ active memristor neurons,” *Nature Communications*, vol. 9, no. 1, p. 4661, 2018.
- [47] S. H. Jo, T. Chang, I. Ebong, B. B. Bhadviya, P. Mazumder, and W. Lu, “Nanoscale memristor device as synapse in neuromorphic systems,” *Nano Letters*, vol. 10, no. 4, pp. 1297–1301, 2010.
- [48] S. Li, X. Liu, S. K. Nandi, D. K. Venkatachalam, and R. G. Elliman, “High-endurance megahertz electrical self-oscillation in Ti/NbO_x bilayer structures,” *Applied Physics Letters*, vol. 106, no. 21, p. 212902, 2015.
- [49] S. Kumar, R. S. Williams, and Z. Wang, “Third-order nanocircuit elements for neuromorphic engineering,” *Nature*, vol. 585, no. 7826, pp. 518–523, 2020.
- [50] X. Zhang, Y. Zhuo, Q. Luo, Z. Wu, R. Midya, Z. Wang, W. Song, R. Wang, N. K. Upadhyay, and Y. Fang, “An artificial spiking afferent nerve based on Mott memristors for neurorobotics,” *Nature Communications*, vol. 11, no. 1, pp. 1–9, 2020.
- [51] J. H. Yoon, Z. Wang, K. M. Kim, H. Wu, V. Ravichandran, Q. Xia, C. S. Hwang, and J. J. Yang, “An artificial nociceptor based on a diffusive memristor,” *Nature Communications*, vol. 9, no. 1, pp. 1–9, 2018.
- [52] M. A. Rahman, S. Walia, S. Naznee, M. Taha, S. Nirantar, F. Rahman, M. Bhaskaran, and S. Sriram, “Artificial somatosensors: Feedback receptors for electronic skins,” *Advanced Intelligent Systems*, p. 2000094, 2020.
- [53] Q. Wu, B. Dang, C. Lu, G. Xu, G. Yang, J. Wang, X. Chuai, N. Lu, D. Geng, and H. Wang, “Spike encoding with optic sensory neurons enable a pulse coupled neural network for ultraviolet image segmentation,” *Nano Letters*, 2020.
- [54] C. S. Dash and S. Prabakaran, “Nano resistive memory (re-ram) devices and their applications,” *Reviews on Advanced Materials Science*, vol. 58, no. 1, pp. 248–270, 2019.
- [55] F. Zahoor, T. Z. Azni Zulkifli, and F. A. Khanday, “Resistive random access memory (RRAM): an overview of materials, switching mechanism, performance, multilevel cell (MLC) storage, modeling, and applications,” *Nanoscale Research Letters*, vol. 15, pp. 1–26, 2020.

- [56] H. Wang and X. Yan, “Overview of resistive random access memory (RRAM): Materials, filament mechanisms, performance optimization, and prospects,” *Physica Status Solidi (RRL)-Rapid Research Letters*, vol. 13, no. 9, p. 1900073, 2019.
- [57] T. Mikolajick, H. Wylezich, H. Maehne, and S. Slesazek, “Versatile resistive switching in niobium oxide,” in *IEEE International Symposium on Circuits and Systems (ISCAS)*, pp. 381–384, IEEE, 2016.
- [58] D. Geppert, “A new negative-resistance device,” *Proceedings of the IEEE*, vol. 51, no. 1, pp. 223–223, 1963.
- [59] M. D. Pickett and R. S. Williams, “Sub-100 fJ and sub-nanosecond thermally driven threshold switching in niobium oxide crosspoint nanodevices,” *Nanotechnology*, vol. 23, no. 21, p. 215202, 2012.
- [60] X. Liu, S. M. Sadaf, M. Son, J. Park, J. Shin, W. Lee, K. Seo, D. Lee, and H. Hwang, “Co-occurrence of threshold switching and memory switching in Pt/NbO_x/Pt cells for crosspoint memory applications,” *IEEE Electron Device Letters*, vol. 33, no. 2, pp. 236–238, 2012.
- [61] S. K. Nandi, X. Liu, D. K. Venkatachalam, and R. G. Elliman, “Threshold current reduction for the metal-insulator transition in NbO_{2-x}-selector devices: the effect of ReRAM integration,” *Journal of Physics D: Applied Physics*, vol. 48, no. 19, p. 195105, 2015.
- [62] D. Ielmini and R. Waser, *Resistive switching: from fundamentals of nanoionic redox processes to memristive device applications*. John Wiley & Sons, 2015.
- [63] S. Slesazek and T. Mikolajick, “Nanoscale resistive switching memory devices: a review,” *Nanotechnology*, vol. 30, no. 35, p. 352003, 2019.
- [64] R. Waser and M. Aono, “Nanoionics-based resistive switching memories,” *Nature Materials*, vol. 6, no. 11, pp. 833–840, 2007.
- [65] J. Kwon, A. A. Sharma, C.-Y. Chen, A. Fantini, M. Jurczak, A. A. Herzing, J. A. Bain, Y. N. Picard, and M. Skowronski, “Transient thermometry and high-resolution transmission electron microscopy analysis of filamentary resistive switches,” *ACS Applied Materials & Interfaces*, vol. 8, no. 31, pp. 20176–20184, 2016.
- [66] J. Zhu, T. Zhang, Y. Yang, and R. Huang, “A comprehensive review on emerging artificial neuromorphic devices,” *Applied Physics Reviews*, vol. 7, no. 1, p. 011312, 2020.

- [67] Y. Wang, K.-M. Kang, M. Kim, H.-S. Lee, R. Waser, D. Wouters, R. Dittmann, J. J. Yang, and H.-H. Park, “Mott-transition-based RRAM,” *Materials Today*, vol. 28, pp. 63–80, 2019.
- [68] A. Sawa, “Resistive switching in transition metal oxides,” *Materials today*, vol. 11, no. 6, pp. 28–36, 2008.
- [69] S. R. Ovshinsky, “Reversible electrical switching phenomena in disordered structures,” *Physical Review Letters*, vol. 21, no. 20, p. 1450, 1968.
- [70] D. Lee, M. Kwak, K. Moon, W. Choi, J. Park, J. Yoo, J. Song, S. Lim, C. Sung, W. Banerjee, *et al.*, “Various threshold switching devices for integrate and fire neuron applications,” *Advanced Electronic Materials*, vol. 5, no. 9, p. 1800866, 2019.
- [71] J. Rupp, R. Waser, and D. Wouters, “Threshold switching in amorphous Cr-doped vanadium oxide for new crossbar selector,” in *IEEE 8th International Memory Workshop (IMW)*, pp. 1–4, IEEE, 2016.
- [72] A. Fakih, *Current controlled negative differential resistance in niobium dioxide*. Thesis, Sorbonne Université Ecole Doctorale 397 - Physique et chimie des matériaux, 2019.
- [73] A. A. Sharma, J. A. Bain, and J. A. Weldon, “Phase coupling and control of oxide-based oscillators for neuromorphic computing,” *IEEE Journal on Exploratory Solid-State Computational Devices and Circuits*, vol. 1, pp. 58–66, 2015.
- [74] A. Alexandrov, A. Bratkovsky, B. Bridle, S. Savel’Ev, D. Strukov, and R. Stanley Williams, “Current-controlled negative differential resistance due to joule heating in TiO_2 ,” *Applied Physics Letters*, vol. 99, no. 20, p. 202104, 2011.
- [75] B. Ridley, “Specific negative resistance in solids,” *Proceedings of the Physical Society*, vol. 82, no. 6, p. 954, 1963.
- [76] J. Ding, K. Jin, Z. Zhang, and T. Wu, “Dependence of negative differential resistance on electronic phase separation in unpatterned manganite films,” *Applied Physics Letters*, vol. 100, no. 6, p. 062402, 2012.
- [77] G. A. Gibson, “Designing negative differential resistance devices based on self-heating,” *Advanced Functional Materials*, vol. 28, no. 22, p. 1704175, 2018.
- [78] S. Kumar, Z. Wang, N. Davila, N. Kumari, K. J. Norris, X. Huang, J. P. Strachan, D. Vine, A. D. Kilcoyne, and Y. Nishi, “Physical origins of current and temperature

- controlled negative differential resistances in NbO_2 ,” *Nature Communications*, vol. 8, no. 1, p. 658, 2017.
- [79] J. M. Goodwill, G. Ramer, D. Li, B. D. Hoskins, G. Pavlidis, J. J. McClelland, A. Centrone, J. A. Bain, and M. Skowronski, “Spontaneous current constriction in threshold switching devices,” *Nature Communications*, vol. 10, no. 1, p. 1628, 2019.
- [80] H. Mähne, H. Wylezich, S. Slesazeck, T. Mikolajick, J. Vesely, V. Klemm, and D. Rafaja, “Room temperature fabricated $\text{NbO}_x/\text{Nb}_2\text{O}_5$ memory switching device with threshold switching effect,” in *5th IEEE International Memory Workshop (IMW)*, pp. 174–177, IEEE, 2013.
- [81] H. Alagoz, K. Chow, and J. Jung, “Low-temperature coexistence of memory and threshold switchings in $\text{Pt}/\text{TiO}_x/\text{Pt}$ crossbar arrays,” *Applied Physics Letters*, vol. 114, no. 16, p. 163502, 2019.
- [82] S. Li, X. Liu, S. K. Nandi, and R. G. Elliman, “Anatomy of filamentary threshold switching in amorphous niobium oxide,” *Nanotechnology*, vol. 29, no. 37, p. 375705, 2018.
- [83] S. K. Nandi, X. Liu, D. K. Venkatachalam, and R. G. Elliman, “Self-assembly of an NbO_2 interlayer and configurable resistive switching in $\text{Pt}/\text{Nb}/\text{HfO}_2/\text{Pt}$ structures,” *Applied Physics Letters*, vol. 107, no. 13, p. 132901, 2015.
- [84] P. Periasamy, H. L. Guthrey, A. I. Abdulagatov, P. F. Ndione, J. J. Berry, D. S. Ginley, S. M. George, P. A. Parilla, and R. P. O’Hayre, “Metal-insulator-metal diodes: Role of the insulator layer on the rectification performance,” *Advanced Materials*, vol. 25, no. 9, pp. 1301–1308, 2013.
- [85] L. Michalas, M. Trapatseli, S. Stathopoulos, S. Cortese, A. Khiat, and T. Prodromakis, “Interface asymmetry induced by symmetric electrodes on Metal-Al:TiO_x-metal structures,” *IEEE Transactions on Nanotechnology*, vol. 17, no. 5, pp. 867–872, 2017.
- [86] R. H. Fowler and L. Nordheim, “Electron emission in intense electric fields,” *Proceedings of the Royal Society of London. Series A, Containing Papers of a Mathematical and Physical Character*, vol. 119, no. 781, pp. 173–181, 1928.
- [87] F.-C. Chiu, “A review on conduction mechanisms in dielectric films,” *Advances in Materials Science and Engineering*, vol. 2014, 2014.

- [88] D. K. Schroder, *Semiconductor material and device characterization*. John Wiley & Sons, 2015.
- [89] J. G. Simmons, “Poole-frenkel effect and schottky effect in metal-insulator-metal systems,” *Physical Review*, vol. 155, no. 3, p. 657, 1967.
- [90] D. Ielmini and Y. Zhang, “Analytical model for subthreshold conduction and threshold switching in chalcogenide-based memory devices,” *Journal of Applied Physics*, vol. 102, no. 5, p. 054517, 2007.
- [91] A. Miller and E. Abrahams, “Impurity conduction at low concentrations,” *Physical Review*, vol. 120, no. 3, p. 745, 1960.
- [92] N. F. Mott and E. A. Davis, *Electronic processes in non-crystalline materials*. Oxford university press, 2012.
- [93] Y. Zhou and S. Ramanathan, “Correlated electron materials and field effect transistors for logic: a review,” *Critical Reviews in Solid State and Materials Sciences*, vol. 38, no. 4, pp. 286–317, 2013.
- [94] N. Mott, *Metal-insulator transitions*. CRC Press, 2004.
- [95] N. F. Mott, “Metal-insulator transition,” *Reviews of Modern Physics*, vol. 40, no. 4, p. 677, 1968.
- [96] F. Gebhard, “Metal-insulator transitions,” *The Mott Metal-Insulator Transition*, pp. 1–48, 1997.
- [97] B.-J. Kim, Y. W. Lee, S. Choi, J.-W. Lim, S. J. Yun, H.-T. Kim, T.-J. Shin, and H.-S. Yun, “Micrometer x-ray diffraction study of VO₂ films: Separation between metal-insulator transition and structural phase transition,” *Physical Review B*, vol. 77, no. 23, p. 235401, 2008.
- [98] R. E. Peierls, *Quantum theory of solids*. Clarendon Press, 1996.
- [99] P. W. Anderson, “Absence of diffusion in certain random lattices,” *Physical Review*, vol. 109, no. 5, p. 1492, 1958.
- [100] T. Ying, Y. Gu, X. Chen, X. Wang, S. Jin, L. Zhao, W. Zhang, and X. Chen, “Anderson localization of electrons in single crystals: Li_xFe₇Se₈,” *Science Advances*, vol. 2, no. 2, p. e1501283, 2016.

- [101] C. Nico, T. Monteiro, and M. P. Graça, “Niobium oxides and niobates physical properties: Review and prospects,” *Progress in Materials Science*, vol. 80, pp. 1–37, 2016.
- [102] D. Bach, *EELS investigations of stoichiometric niobium oxides and niobium-based capacitors*. Thesis, Universität Karlsruhe, 2009.
- [103] R. Elliott, “Columbium-oxygen system,” *Trans. Am. Soc. Metals*, vol. 52, 1960.
- [104] J. Niebuhr, “Die niederen oxide des tantals,” *Journal of the Less Common Metals*, vol. 10, no. 5, pp. 312–322, 1966.
- [105] M. Grundner and J. Halbritter, “XPS and AES studies on oxide growth and oxide coatings on niobium,” *Journal of Applied Physics*, vol. 51, no. 1, pp. 397–405, 1980.
- [106] S. Andersson and A. Wadsley, “Crystallographic shear and diffusion paths in certain higher oxides of niobium, tungsten, molybdenum and titanium,” *Nature*, vol. 211, no. 5049, pp. 581–583, 1966.
- [107] A. A. McConnell, J. Aderson, and C. Rao, “Raman spectra of niobium oxides,” *Spectrochimica Acta Part A: Molecular Spectroscopy*, vol. 32, no. 5, pp. 1067–1076, 1976.
- [108] J. Halbritter, “On the oxidation and on the superconductivity of niobium,” *Applied Physics A*, vol. 43, no. 1, pp. 1–28, 1987.
- [109] B. Meyer and R. Gruehn, “Umwandlungs-und reduktionsprodukte von metastabilem Nb_2O_5 (ox2bi), elektronenoptische untersuchung,” *Journal of the Less Common Metals*, vol. 83, no. 2, pp. 185–203, 1982.
- [110] E. S. Crawford and J. S. Anderson, “Homogeneous solid state transformations in niobium oxides,” *Philosophical Transactions of the Royal Society of London. Series A, Mathematical and Physical Sciences*, vol. 304, no. 1485, pp. 327–364, 1982.
- [111] D. R. Lide, *CRC Handbook of Chemistry and Physics*, vol. 85. CRC press, 2004.
- [112] R. Tye, “Preliminary measurements on the thermal and electrical conductivities of molybdenum, niobium, tantalum and tungsten,” *Journal of the Less Common Metals*, vol. 3, no. 1, pp. 13–18, 1961.
- [113] E. R. Pollard Jr, *Electronic properties of niobium monoxide*. Thesis, Massachusetts Institute of Technology, 1968.
- [114] J. Gallego and C. Thomas, “The conductivity at high fields in films of amorphous niobium dioxide,” *Solid State Communications*, vol. 47, no. 6, pp. 419–422, 1983.

- [115] R. Janninck and D. Whitmore, “Electrical conductivity and thermoelectric power of niobium dioxide,” *Journal of Physics and Chemistry of Solids*, vol. 27, no. 6-7, pp. 1183–1187, 1966.
- [116] Y. Zhao, Z. Zhang, and Y. Lin, “Optical and dielectric properties of a nanostructured NbO₂ thin film prepared by thermal oxidation,” *Journal of Physics D: Applied Physics*, vol. 37, no. 24, p. 3392, 2004.
- [117] D. Adler, “Mechanisms for metal-nonmetal transitions in transition-metal oxides and sulfides,” *Reviews of Modern Physics*, vol. 40, no. 4, p. 714, 1968.
- [118] Z. Weibin, W. Weidong, W. Xueming, C. Xinlu, Y. Dawei, S. Changle, P. Liping, W. Yuying, and B. Li, “The investigation of NbO₂ and Nb₂O₅ electronic structure by XPS, UPS and first principles methods,” *Surface and Interface Analysis*, vol. 45, no. 8, pp. 1206–1210, 2013.
- [119] J. Lee and W. W. Durand, “Electrically stimulated optical switching of NbO₂ thin films,” *Journal of Applied Physics*, vol. 56, no. 11, pp. 3350–3352, 1984.
- [120] A. B. Posadas, A. O’Hara, S. Rangan, R. A. Bartynski, and A. A. Demkov, “Band gap of epitaxial in-plane-dimerized single-phase NbO₂ films,” *Applied Physics Letters*, vol. 104, no. 9, p. 092901, 2014.
- [121] Y. Sakai, N. Tsuda, and T. Sakata, “Electrical properties of semiconducting NbO₂,” *Journal of the Physical Society of Japan*, vol. 54, no. 4, pp. 1514–1518, 1985.
- [122] V. Fischer, H. Stormer, D. Gerthsen, M. Stenzel, H. Zillgen, and E. Ivers-Tiffée, “Niobium as new material for electrolyte capacitors with nanoscale dielectric oxide layers,” in *Proceedings of the 7th International Conference on Properties and Applications of Dielectric Materials (Cat. No. 03CH37417)*, vol. 3, pp. 1134–1137, IEEE, 2003.
- [123] H. Störmer, A. Weber, V. Fischer, E. Ivers-Tiffée, and D. Gerthsen, “Anodically formed oxide films on niobium: microstructural and electrical properties,” *Journal of the European Ceramic Society*, vol. 29, no. 9, pp. 1743–1753, 2009.
- [124] G. Jouv, “Electrical conduction mechanisms in electrochemically formed amorphous films of Nb₂O₅,” *Philosophical Magazine B*, vol. 64, no. 2, pp. 207–218, 1991.
- [125] D. B. de Filho, D. Franco, P. A Filho, and O. Alves, “Niobia films: surface morphology, surface analysis, photoelectrochemical properties and crystallization process,” *Journal of Materials Science*, vol. 33, no. 10, pp. 2607–2616, 1998.

- [126] G. Cavigliasso, M. Esplandiu, and V. Macagno, "Influence of the forming electrolyte on the electrical properties of tantalum and niobium oxide films: an EIS comparative study," *Journal of Applied Electrochemistry*, vol. 28, no. 11, pp. 1213–1219, 1998.
- [127] J. W. Schultze and M. Lohrengel, "Stability, reactivity and breakdown of passive films. problems of recent and future research," *Electrochimica Acta*, vol. 45, no. 15-16, pp. 2499–2513, 2000.
- [128] M. Maček and B. Orel, "Electrochromism of sol-gel derived niobium oxide films," *Solar Energy Materials and Solar Cells*, vol. 54, no. 1-4, pp. 121–130, 1998.
- [129] M. Soares, S. Leite, C. Nico, M. Peres, A. Fernandes, M. Graça, M. Matos, R. Monteiro, T. Monteiro, and F. Costa, "Effect of processing method on physical properties of Nb₂O₅," *Journal of the European Ceramic Society*, vol. 31, no. 4, pp. 501–506, 2011.
- [130] M. Graça, A. Meireles, C. Nico, and M. Valente, "Nb₂O₅ nanosize powders prepared by sol-gel-structure, morphology and dielectric properties," *Journal of Alloys and Compounds*, vol. 553, pp. 177–182, 2013.
- [131] H. Schäfer, D. Bergner, and R. Gruehn, "Beiträge zur chemie der elemente niob und tantal. lxxi. die thermodynamische stabilität der sieben zwischen 2, 00 und 2, 50 O/Nb existierenden phasen," *Zeitschrift für Anorganische und Allgemeine Chemie*, vol. 365, no. 1-2, pp. 31–50, 1969.
- [132] M. Kovendhan, D. P. Joseph, P. Manimuthu, S. Ganesan, S. Sambasivam, P. Maruthamuthu, S. A. Suthanthiraraj, C. Venkateswaran, and R. Mohan, "Spray deposited Nb₂O₅ thin film electrodes for fabrication of dye sensitized solar cells," *Transactions of the Indian Institute of Metals*, vol. 64, no. 1-2, p. 185, 2011.
- [133] T. El-Shazly, W. M. Hassan, S. T. A. Rahim, and N. K. Allam, "Unravelling the interplay of dopant concentration and band structure engineering of monoclinic niobium pentoxide: a model photoanode for water splitting," *International Journal of Hydrogen Energy*, vol. 40, no. 40, pp. 13867–13875, 2015.
- [134] S.-H. Lee, J.-D. Kwon, J.-H. Ahn, and J.-S. Park, "Compositional and electrical modulation of niobium oxide thin films deposited by plasma-enhanced atomic layer deposition," *Ceramics International*, vol. 43, no. 8, pp. 6580–6584, 2017.
- [135] L. Kommel, E. Kimmari, M. Saarna, and M. Viljus, "Processing and properties of bulk ultrafine-grained pure niobium," *Journal of Materials Science*, vol. 48, no. 13, pp. 4723–4729, 2013.

- [136] M. J. Donachie and S. J. Donachie, *Superalloys: a technical guide*. ASM international, 2002.
- [137] Z. Patel and K. Khul’ka, “Niobium for steelmaking,” *Metallurgist*, vol. 45, no. 11-12, pp. 477–480, 2001.
- [138] Y. Zhang, D. Sun, J. Cheng, J. K. H. Tsoi, and J. Chen, “Mechanical and biological properties of Ti-(0–25 wt%)Nb alloys for biomedical implants application,” *Regenerative Biomaterials*, vol. 7, no. 1, pp. 119–127, 2020.
- [139] A. Bowman, T. Wallace, J. Yarnell, and R. Wenzel, “The crystal structure of niobium monoxide,” *Acta Crystallographica*, vol. 21, no. 5, pp. 843–843, 1966.
- [140] J. Hulm, C. Jones, R. Hein, and J. Gibson, “Superconductivity in the TiO and NbO systems,” *Journal of Low Temperature Physics*, vol. 7, no. 3-4, pp. 291–307, 1972.
- [141] A. M. Okaz and P. Keesom, “Specific heat and magnetization of the superconducting monoxides: NbO and TiO,” *Physical Review B*, vol. 12, no. 11, p. 4917, 1975.
- [142] W. Gao, J. Conley Jr, and Y. Ono, “NbO as gate electrode for n-channel metal-oxide-semiconductor field-effect-transistors,” *Applied Physics Letters*, vol. 84, no. 23, pp. 4666–4668, 2004.
- [143] C. Nico, M. Soares, J. Rodrigues, M. Matos, R. Monteiro, M. Graça, M. Valente, F. Costa, and T. Monteiro, “Sintered NbO powders for electronic device applications,” *The Journal of Physical Chemistry C*, vol. 115, no. 11, pp. 4879–4886, 2011.
- [144] Y. Qiu, D. Smyth, and J. Kimmel, “The stabilization of niobium-based solid electrolyte capacitors,” *Active and Passive Electronic Components*, vol. 25, 2002.
- [145] A. O’Hara, T. N. Nunley, A. B. Posadas, S. Zollner, and A. A. Demkov, “Electronic and optical properties of NbO₂,” *Journal of Applied Physics*, vol. 116, no. 21, p. 213705, 2014.
- [146] S. K. E. Forghany and J. S. Anderson, “Reduction and polymorphic transformation of B-Nb₂O₅,” *Journal of the Chemical Society, Dalton Transactions*, no. 1, pp. 255–261, 1981.
- [147] A. Cheetham and C. Rao, “A neutron diffraction study of niobium dioxide,” *Acta Crystallographica Section B: Structural Crystallography and Crystal Chemistry*, vol. 32, no. 5, pp. 1579–1580, 1976.

- [148] J. Gallego and C. Thomas, “Phase transitions in films of niobium dioxide,” *Solid State Communications*, vol. 43, no. 7, pp. 547–549, 1982.
- [149] Z. Yang, C. Ko, and S. Ramanathan, “Oxide electronics utilizing ultrafast metal-insulator transitions,” *Annual Review of Materials Research*, vol. 41, pp. 337–367, 2011.
- [150] F. J. Wong, N. Hong, and S. Ramanathan, “Orbital splitting and optical conductivity of the insulating state of NbO_2 ,” *Physical Review B*, vol. 90, no. 11, p. 115135, 2014.
- [151] S. Kumar, J. P. Strachan, and R. S. Williams, “Chaotic dynamics in nanoscale NbO_2 Mott memristors for analogue computing,” *Nature*, vol. 548, no. 7667, p. 318, 2017.
- [152] S. Li, X. Liu, S. K. Nandi, S. K. Nath, and R. G. Elliman, “Origin of current-controlled negative differential resistance modes and the emergence of composite characteristics with high complexity,” *Advanced Functional Materials*, p. 1905060, 2019.
- [153] L. Huang, J. Wu, P. Han, A. M. Al-Enizi, T. M. Almutairi, L. Zhang, and G. Zheng, “ NbO_2 electrocatalyst toward 32% Faradaic efficiency for N_2 fixation,” *Small Methods*, vol. 3, no. 6, p. 1800386, 2019.
- [154] D. Music, P. Schmidt, and A. Saksena, “Experimental and theoretical exploration of mechanical stability of Pt/NbO_2 interfaces for thermoelectric applications,” *Journal of Physics D: Applied Physics*, vol. 50, no. 45, p. 455502, 2017.
- [155] H. Schäfer, R. Gruehn, and F. Schulte, “The modifications of niobium pentoxide,” *Angewandte Chemie International Edition in English*, vol. 5, no. 1, pp. 40–52, 1966.
- [156] L. Reznichenko, V. Akhnazarova, L. Shilkina, O. Razumovskaya, and S. Dudkina, “Invar effect in $n\text{-Nb}_2\text{O}_5$, $\alpha\text{-HT-Nb}_2\text{O}_5$, and $\text{L-Nb}_2\text{O}_5$,” *Crystallography Reports*, vol. 54, no. 3, pp. 483–491, 2009.
- [157] R. A. Rani, A. S. Zoolfakar, A. P. O’Mullane, M. W. Austin, and K. Kalantar-Zadeh, “Thin films and nanostructures of niobium pentoxide: fundamental properties, synthesis methods and applications,” *Journal of Materials Chemistry A*, vol. 2, no. 38, pp. 15683–15703, 2014.
- [158] A. Kohli, C. Wang, and S. Akbar, “Niobium pentoxide as a lean-range oxygen sensor,” *Sensors and Actuators B: Chemical*, vol. 56, no. 1-2, pp. 121–128, 1999.
- [159] W.-J. Chen, X. Sun, Y. Liu, M. Huang, W. Xu, X. Pan, Q. Wu, and Z. Yi, “ Nb_2O_5 nanorod bundles for photocatalytic ethylene oxidation,” *ACS Applied Nano Materials*, vol. 3, no. 3, pp. 2573–2581, 2020.

- [160] X. Deng, Y. Jiang, Z. Wei, M. Mao, R. Pothu, H. Wang, C. Wang, J. Liu, and J. Ma, “Flexible quasi-solid-state dual-ion asymmetric supercapacitor based on $\text{Ni}(\text{OH})_2$ and Nb_2O_5 nanosheet arrays,” *Green Energy & Environment*, vol. 4, no. 4, pp. 382–390, 2019.
- [161] T. Josué, L. Almeida, M. Lopes, O. Santos, and G. Lenzi, “Cr (VI) reduction by photocatalytic process: Nb_2O_5 an alternative catalyst,” *Journal of Environmental Management*, vol. 268, p. 110711, 2020.
- [162] J. Marucco, “Electrical resistance and defect structure of stable and metastable phases of the system $\text{Nb}_{12}\text{O}_{29}$ - Nb_2O_5 between 800 and 1100°C ,” *The Journal of Chemical Physics*, vol. 70, no. 2, pp. 649–654, 1979.
- [163] H. Wylezich, H. Mähne, J. Rensberg, C. Ronning, P. Zahn, S. Slesazeck, and T. Mikolajick, “Local ion irradiation-induced resistive threshold and memory switching in $\text{Nb}_2\text{O}_5/\text{NbO}_x$ films,” *ACS Applied Materials & Interfaces*, vol. 6, no. 20, pp. 17474–17480, 2014.
- [164] A. C. Kozen, Z. R. Robinson, E. R. Glaser, M. Twigg, T. J. Larrabee, H. Cho, S. Prokes, and L. B. Ruppalt, “In situ hydrogen plasma exposure for varying the stoichiometry of atomic layer deposited Niobium Oxide films for use in neuromorphic computing applications,” *ACS Applied Materials & Interfaces*, vol. 12, no. 14, pp. 16639–16647, 2020.
- [165] W. Hiatt and T. Hickmott, “Bistable switching in niobium oxide diodes,” *Applied Physics Letters*, vol. 6, no. 6, pp. 106–108, 1965.
- [166] S. Spiga, A. Lamperti, C. Wiemer, M. Perego, E. Cianci, G. Tallarida, H. Lu, M. Alia, F. Volpe, and M. Fanciulli, “Resistance switching in amorphous and crystalline binary oxides grown by electron beam evaporation and atomic layer deposition,” *Microelectronic Engineering*, vol. 85, no. 12, pp. 2414–2419, 2008.
- [167] F. Hanzig, H. Mähne, J. Veselý, H. Wylezich, S. Slesazeck, A. Leuteritz, M. Zschornak, M. Motylenko, V. Klemm, and T. Mikolajick, “Effect of the stoichiometry of niobium oxide on the resistive switching of Nb_2O_5 based metal-insulator-metal stacks,” *Journal of Electron Spectroscopy and Related Phenomena*, vol. 202, pp. 122–127, 2015.
- [168] X. Liu, S. K. Nandi, D. K. Venkatachalam, K. Belay, S. Song, and R. G. Elliman, “Reduced threshold current in NbO_2 selector by engineering device structure,” *IEEE Electron Device Letters*, vol. 35, no. 10, pp. 1055–1057, 2014.

- [169] H. Mähne, L. Berger, D. Martin, V. Klemm, S. Slesazeck, S. Jakschik, D. Rafaja, and T. Mikolajick, “Filamentary resistive switching in amorphous and polycrystalline Nb₂O₅ thin films,” *Solid-State Electronics*, vol. 72, pp. 73–77, 2012.
- [170] V. Eyert, “The metal-insulator transition of NbO₂ : An embedded peierls instability,” *EPL (Europhysics Letters)*, vol. 58, no. 6, p. 851, 2002.
- [171] G. A. Gibson, S. Musunuru, J. Zhang, K. Vandenberghe, J. Lee, C.-C. Hsieh, W. Jackson, Y. Jeon, D. Henze, and Z. Li, “An accurate locally active memristor model for s-type negative differential resistance in NbO_x,” *Applied Physics Letters*, vol. 108, no. 2, p. 023505, 2016.
- [172] Y. Lu, B. Gao, Y. Fu, B. Chen, L. Liu, X. Liu, and J. Kang, “A simplified model for resistive switching of oxide-based resistive random access memory devices,” *IEEE Electron Device Letters*, vol. 33, no. 3, pp. 306–308, 2012.
- [173] E. Cha, J. Park, J. Woo, D. Lee, A. Prakash, and H. Hwang, “Comprehensive scaling study of NbO₂ insulator-metal-transition selector for cross point array application,” *Applied Physics Letters*, vol. 108, no. 15, p. 153502, 2016.
- [174] S. Kim, J. Park, J. Woo, C. Cho, W. Lee, J. Shin, G. Choi, S. Park, D. Lee, and B. H. Lee, “Threshold-switching characteristics of a nanothin-NbO₂-layer-based Pt/NbO₂/Pt stack for use in cross-point-type resistive memories,” *Microelectronic Engineering*, vol. 107, pp. 33–36, 2013.
- [175] T. Joshi, T. R. Senty, P. Borisov, A. D. Bristow, and D. Lederman, “Preparation, characterization, and electrical properties of epitaxial NbO₂ thin film lateral devices,” *Journal of Physics D: Applied Physics*, vol. 48, no. 33, p. 335308, 2015.
- [176] J. Park, E. Cha, I. Karpov, and H. Hwang, “Dynamics of electroforming and electrically driven insulator-metal transition in NbO_x selector,” *Applied Physics Letters*, vol. 108, no. 23, p. 232101, 2016.
- [177] Y. Wang, R. B. Comes, S. A. Wolf, and J. Lu, “Threshold switching characteristics of Nb/NbO₂/TiN vertical devices,” *IEEE Journal of the Electron Devices Society*, vol. 4, no. 1, pp. 11–14, 2016.
- [178] J. Park, E. Cha, D. Lee, S. Lee, J. Song, J. Park, and H. Hwang, “Improved threshold switching characteristics of multi-layer NbO_x for 3-d selector application,” *Microelectronic Engineering*, vol. 147, pp. 318–320, 2015.

- [179] J. Yang, J. Gill, J. Kennedy, S.-Q. Wang, L. Forester, and M. Ross, “Electron beam processing for spin-on polymers and its applications to back-end-of-line (BEOL) integration,” *MRS Online Proceedings Library Archive*, vol. 511, 1998.
- [180] S. K. Nandi, X. Liu, S. Li, D. K. Venkatachalam, K. Belay, and R. G. Elliman, “Resistive switching behavior in HfO_2 with Nb as an oxygen exchange layer,” in *Conference on Optoelectronic and Microelectronic Materials & Devices (COMMAD)*, pp. 290–293, IEEE, 2014.
- [181] S. K. Nandi, X. Liu, D. K. Venkatachalam, and R. G. Elliman, “Effect of electrode roughness on electroforming in HfO_2 and defect-induced moderation of electric-field enhancement,” *Physical Review Applied*, vol. 4, no. 6, p. 064010, 2015.
- [182] R. Degraeve, J.-L. Ogier, R. Bellens, P. Roussel, G. Groeseneken, and H. Maes, “A new model for the field dependence of intrinsic and extrinsic time-dependent dielectric breakdown,” *IEEE Transactions on Electron Devices*, vol. 45, no. 2, pp. 472–481, 1998.
- [183] D. L. Crook, “Method of determining reliability screens for time dependent dielectric breakdown,” in *17th International Reliability Physics Symposium*, pp. 1–7, IEEE, 1979.
- [184] S. Diaham, S. Zelmat, M.-L. Locatelli, S. Dinculescu, M. Decup, and T. Lebey, “Dielectric breakdown of polyimide films: Area, thickness and temperature dependence,” *IEEE Transactions on Dielectrics and Electrical Insulation*, vol. 17, no. 1, pp. 18–27, 2010.
- [185] C. Nauenheim, C. Kuegeler, A. Ruediger, and R. Waser, “Investigation of the electroforming process in resistively switching TiO_2 nanocrosspoint junctions,” *Applied Physics Letters*, vol. 96, no. 12, p. 122902, 2010.
- [186] R. Waser, R. Dittmann, G. Staikov, and K. Szot, “Redox-based resistive switching memories-nanoionic mechanisms, prospects, and challenges,” *Advanced Materials*, vol. 21, no. 25-26, pp. 2632–2663, 2009.
- [187] S. Kumar, C. E. Graves, J. P. Strachan, E. M. Grafals, A. L. D. Kilcoyne, T. Tyliczszak, J. N. Weker, Y. Nishi, and R. S. Williams, “Direct observation of localized radial oxygen migration in functioning tantalum oxide memristors,” *Advanced Materials*, vol. 28, no. 14, pp. 2772–2776, 2016.
- [188] D. B. Strukov, F. Alibart, and R. S. Williams, “Thermophoresis/diffusion as a plausible mechanism for unipolar resistive switching in metal-oxide-metal memristors,” *Applied Physics A*, vol. 107, no. 3, pp. 509–518, 2012.

- [189] Y. Ma, D. Li, A. A. Herzing, D. A. Cullen, B. T. Sneed, K. L. More, N. Nuhfer, J. A. Bain, and M. Skowronski, "Formation of the conducting filament in TaO_x-resistive switching devices by thermal-gradient-induced cation accumulation," *ACS Applied Materials & Interfaces*, vol. 10, no. 27, pp. 23187–23197, 2018.
- [190] M. Uenuma, Y. Ishikawa, and Y. Uraoka, "Joule heating effect in nonpolar and bipolar resistive random access memory," *Applied Physics Letters*, vol. 107, no. 7, p. 073503, 2015.
- [191] J. Y. Ye, Y. Q. Li, J. Gao, H. Y. Peng, S. X. Wu, and T. Wu, "Nanoscale resistive switching and filamentary conduction in NiO thin films," *Applied Physics Letters*, vol. 97, no. 13, p. 132108, 2010.
- [192] S. Kumar and R. S. Williams, "Separation of current density and electric field domains caused by nonlinear electronic instabilities," *Nature Communications*, vol. 9, 2018.
- [193] P. Calka, E. Martinez, V. Delaye, D. Lafond, G. Audoit, D. Mariolle, N. Chevalier, H. Grampeix, C. Cagli, and V. Jousseau, "Chemical and structural properties of conducting nanofilaments in TiN/HfO₂-based resistive switching structures," *Nanotechnology*, vol. 24, no. 8, p. 085706, 2013.
- [194] J.-Y. Chen, C.-L. Hsin, C.-W. Huang, C.-H. Chiu, Y.-T. Huang, S.-J. Lin, W.-W. Wu, and L.-J. Chen, "Dynamic evolution of conducting nanofilament in resistive switching memories," *Nano Letters*, vol. 13, no. 8, pp. 3671–3677, 2013.
- [195] J. M. Goodwill, D. K. Gala, J. A. Bain, and M. Skowronski, "Switching dynamics of TaO_x-based threshold switching devices," *Journal of Applied Physics*, vol. 123, no. 11, p. 115105, 2018.
- [196] J. M. Goodwill, A. A. Sharma, D. Li, J. A. Bain, and M. Skowronski, "Electro-thermal model of threshold switching in TaO_x-based devices," *ACS Applied Materials & Interfaces*, vol. 9, no. 13, pp. 11704–11710, 2017.
- [197] Y. Ma, J. M. Goodwill, D. Li, D. A. Cullen, J. D. Poplawsky, K. L. More, J. A. Bain, and M. Skowronski, "Stable metallic enrichment in conductive filaments in TaO_x-based resistive switches arising from competing diffusive fluxes," *Advanced Electronic Materials*, vol. 5, no. 7, p. 1800954, 2019.
- [198] J. J. Yang, F. Miao, M. D. Pickett, D. A. Ohlberg, D. R. Stewart, C. N. Lau, and R. S. Williams, "The mechanism of electroforming of metal oxide memristive switches," *Nanotechnology*, vol. 20, no. 21, p. 215201, 2009.

- [199] A. A. Sharma, M. Noman, M. Abdelmoula, M. Skowronski, and J. A. Bain, “Electronic instabilities leading to electroformation of binary metal oxide-based resistive switches,” *Advanced Functional Materials*, vol. 24, no. 35, pp. 5522–5529, 2014.
- [200] D. Morgan, M. Howes, R. Pollard, and D. Waters, “Electroforming and dielectric breakdown in thin aluminium oxide films,” *Thin Solid Films*, vol. 15, no. 1, pp. 123–131, 1973.
- [201] C.-Y. Lin, P.-H. Chen, T.-C. Chang, K.-C. Chang, S.-D. Zhang, T.-M. Tsai, C.-H. Pan, M.-C. Chen, Y.-T. Su, and Y.-T. Tseng, “Attaining resistive switching characteristics and selector properties by varying forming polarities in a single HfO₂-based RRAM device with a vanadium electrode,” *Nanoscale*, vol. 9, no. 25, pp. 8586–8590, 2017.
- [202] D.-Y. Cho, M. Luebben, S. Wiefels, K.-S. Lee, and I. Valov, “Interfacial Metal-Oxide interactions in resistive switching memories,” *ACS Applied Materials & Interfaces*, vol. 9, no. 22, pp. 19287–19295, 2017.
- [203] U. Celano, J. Op de Beeck, S. Clima, M. Luebben, P. M. Koenraad, L. Goux, I. Valov, and W. Vandervorst, “Direct probing of the dielectric scavenging-layer interface in oxide filamentary-based valence change memory,” *ACS Applied Materials & Interfaces*, vol. 9, no. 12, pp. 10820–10824, 2017.
- [204] Z. Wei, Y. Kanzawa, K. Arita, Y. Katoh, K. Kawai, S. Muraoka, S. Mitani, S. Fujii, K. Katayama, and M. Iijima, “Highly reliable TaO_x ReRAM and direct evidence of redox reaction mechanism,” in *IEEE International Electron Devices Meeting*, pp. 1–4, IEEE, 2008.
- [205] I. Valov, S. Tappertzhofen, E. Linn, S. Menzel, J. van den Hurk, and R. Waser, “(keynote) atomic scale and interface interactions in Redox-based resistive switching memories,” *ECS Transactions*, vol. 64, no. 14, p. 3, 2014.
- [206] I. Valov, “Redox-based resistive switching memories (ReRAMs): Electrochemical systems at the atomic scale,” *ChemElectroChem*, vol. 1, no. 1, pp. 26–36, 2014.
- [207] W. Chien, Y. Chen, E. Lai, F. Lee, Y. Lin, A. T. Chuang, K. Chang, Y. Yao, T. Chou, and H. Lin, “A study of the switching mechanism and electrode material of fully CMOS compatible tungsten oxide ReRAM,” *Applied Physics A*, vol. 102, no. 4, pp. 901–907, 2011.
- [208] T. Tsuruoka, I. Valov, S. Tappertzhofen, J. van den Hurk, T. Hasegawa, R. Waser, and M. Aono, “Redox reactions at Cu, Ag/Ta₂O₅ interfaces and the effects of Ta₂O₅

- film density on the forming process in atomic switch structures,” *Advanced Functional Materials*, vol. 25, no. 40, pp. 6374–6381, 2015.
- [209] W. Kim, S. Menzel, D. J. Wouters, Y. Guo, J. Robertson, B. Roesgen, R. Waser, and V. Rana, “Impact of oxygen exchange reaction at the ohmic interface in Ta₂O₅-based ReRAM devices,” *Nanoscale*, vol. 8, no. 41, pp. 17774–17781, 2016.
- [210] H. Peng, L. Pu, J. Wu, D. Cha, J. Hong, W. Lin, Y. Li, J. Ding, A. David, K. Li, *et al.*, “Effects of electrode material and configuration on the characteristics of planar resistive switching devices,” *APL Materials*, vol. 1, no. 5, p. 052106, 2013.
- [211] D.-Y. Cho, S. Tappertzhofen, R. Waser, and I. Valov, “Chemically-inactive interfaces in thin film Ag/AgI systems for resistive switching memories,” *Scientific Reports*, vol. 3, no. 1, pp. 1–5, 2013.
- [212] D. Cho, I. Valov, J. van den Hurk, S. Tappertzhofen, and R. Waser, “Direct observation of charge transfer in solid electrolyte for electrochemical metallization memory,” *Advanced Materials*, vol. 24, no. 33, pp. 4552–4556, 2012.
- [213] Y. Yang, P. Gao, L. Li, X. Pan, S. Tappertzhofen, S. Choi, R. Waser, I. Valov, and W. D. Lu, “Electrochemical dynamics of nanoscale metallic inclusions in dielectrics,” *Nature Communications*, vol. 5, no. 1, pp. 1–9, 2014.
- [214] A. Kindsmüller, A. Meledin, J. Mayer, R. Waser, and D. J. Wouters, “On the role of the metal oxide/reactive electrode interface during the forming procedure of valence change ReRAM devices,” *Nanoscale*, 2019.
- [215] A. Wedig, M. Luebben, D.-Y. Cho, M. Moors, K. Skaja, V. Rana, T. Hasegawa, K. K. Adepli, B. Yildiz, and R. Waser, “Nanoscale cation motion in TaO_x, HfO_x and TiO_x memristive systems,” *Nature Nanotechnology*, vol. 11, no. 1, pp. 67–74, 2016.
- [216] M.-J. Lee, C. B. Lee, D. Lee, S. R. Lee, M. Chang, J. H. Hur, Y.-B. Kim, C.-J. Kim, D. H. Seo, and S. Seo, “A fast, high-endurance and scalable non-volatile memory device made from asymmetric Ta₂O_{5-x}/TaO_{2-x} bilayer structures,” *Nature Materials*, vol. 10, no. 8, pp. 625–630, 2011.
- [217] D. Li, J. M. Goodwill, J. A. Bain, and M. Skowronski, “Scaling behavior of oxide-based electrothermal threshold switching devices,” *Nanoscale*, vol. 9, no. 37, pp. 14139–14148, 2017.

- [218] J. A. Rupp, M. Querré, A. Kinds Müller, M.-P. Besland, E. Janod, R. Dittmann, R. Waser, and D. J. Wouters, “Different threshold and bipolar resistive switching mechanisms in reactively sputtered amorphous undoped and Cr-doped vanadium oxide thin films,” *Journal of Applied Physics*, vol. 123, no. 4, p. 044502, 2018.
- [219] L. Gao, P.-Y. Chen, and S. Yu, “NbO_x based oscillation neuron for neuromorphic computing,” *Applied Physics Letters*, vol. 111, no. 10, p. 103503, 2017.
- [220] M. Herzig, M. Weiher, A. Ascoli, R. Tetzlaff, T. Mikolajick, and S. Slesazeck, “Improvement of NbO_x-based threshold switching devices by implementing multilayer stacks,” *Semiconductor Science and Technology*, vol. 34, no. 7, p. 075005, 2019.
- [221] E. Cha, J. Woo, D. Lee, S. Lee, J. Song, Y. Koo, J. Lee, C. G. Park, M. Y. Yang, and K. Kamiya, “Nanoscale (10nm) 3D vertical ReRAM and NbO₂ threshold selector with TiN electrode,” in *IEEE International Electron Devices Meeting*, pp. 10.5.1–10.5.4, IEEE, 2013.
- [222] T. Joshi, P. Borisov, and D. Lederman, “Structural and electrical characterization of polycrystalline NbO₂ thin film vertical devices grown on TiN-coated SiO₂/Si substrates,” *Journal of Applied Physics*, vol. 124, no. 11, p. 114502, 2018.
- [223] Y. Wang, Q. Liu, S. Long, W. Wang, Q. Wang, M. Zhang, S. Zhang, Y. Li, Q. Zuo, and J. Yang, “Investigation of resistive switching in Cu-doped HfO₂ thin film for multilevel non-volatile memory applications,” *Nanotechnology*, vol. 21, no. 4, p. 045202, 2009.
- [224] Z. Wang, W. Zhu, A. Du, L. Wu, Z. Fang, X. A. Tran, W. Liu, K. Zhang, and H.-Y. Yu, “Highly uniform, self-compliance, and forming-free ald HfO₂-based RRAM with Ge doping,” *IEEE Transactions on Electron Devices*, vol. 59, no. 4, pp. 1203–1208, 2012.
- [225] H. Zhang, L. Liu, B. Gao, Y. Qiu, X. Liu, J. Lu, R. Han, J. Kang, and B. Yu, “Gd-doping effect on performance of HfO₂ based resistive switching memory devices using implantation approach,” *Applied Physics Letters*, vol. 98, no. 4, p. 042105, 2011.
- [226] S.-S. Li and Y.-K. Su, “Improvement of the performance in Cr-doped ZnO memory devices via control of oxygen defects,” *RSC Advances*, vol. 9, no. 6, pp. 2941–2947, 2019.
- [227] M. Ismail, E. Ahmed, A. M. Rana, F. Hussain, I. Talib, M. Nadeem, D. Panda, and N. Shah, “Improved endurance and resistive switching stability in ceria thin films due to charge transfer ability of Al dopant,” *ACS Applied Materials & Interfaces*, vol. 8, no. 9, pp. 6127–6136, 2016.

- [228] C. Funck, S. Menzel, N. Aslam, H. Zhang, A. Hardtdegen, R. Waser, and S. Hoffmann-Eifert, “Multidimensional simulation of threshold switching in NbO₂ based on an electric field triggered thermal runaway model,” *Advanced Electronic Materials*, vol. 2, no. 7, p. 1600169, 2016.
- [229] S. Slesazeck, H. Mähne, H. Wylezich, A. Wachowiak, J. Radhakrishnan, A. Ascoli, R. Tetzlaff, and T. Mikolajick, “Physical model of threshold switching in NbO₂ based memristors,” *RSC Advances*, vol. 5, no. 124, pp. 102318–102322, 2015.
- [230] T. Chen, M. Tse, C. Sun, S. Fung, and K. Lo, “Snapback behaviour and its similarity to the switching behaviour in ultra-thin silicon dioxide films after hard breakdown,” *Journal of Physics D: Applied Physics*, vol. 34, no. 17, p. L95, 2001.
- [231] T. Suntola, “On the mechanism of switching effects in chalcogenide thin films,” *Solid State Electronics*, vol. 14, no. 10, pp. 933–938, 1971.
- [232] “Microchemicals photoresists, ancillaries, etchants, solvents, and technical support for all stages of microstructuring and lithography.” <https://www.microchemicals.net>.
- [233] M. Thompson and L. Doolittle, “Rump-rbs analysis and simulation package,” *Computer Graphic Service, Version 0.950*, 2002.
- [234] NIST, “X-ray photoelectron spectroscopy database [internet],” *National Institute of Standards and Technology*, 2000.
- [235] Y. Wang, R. B. Comes, S. Kittiwatanakul, S. A. Wolf, and J. Lu, “Epitaxial niobium dioxide thin films by reactive-biased target ion beam deposition,” *Journal of Vacuum Science & Technology A: Vacuum, Surfaces, and Films*, vol. 33, no. 2, p. 021516, 2015.
- [236] M. Kuznetsov, A. Razinkin, and E. Shalaeva, “Photoelectron spectroscopy and diffraction of surface nanoscale NbO/Nb (110) structures,” *Journal of Structural Chemistry*, vol. 50, no. 3, pp. 514–521, 2009.
- [237] A. El Helou, P. E. Raad, A. Venugopal, and D. Kande, “Thermal characterization of Si BEOL microelectronic structures,” in *International Technical Conference and Exhibition on Packaging and Integration of Electronic and Photonic Microsystems*, vol. 51920, p. V001T03A002, American Society of Mechanical Engineers, 2018.
- [238] M. Lanza, U. Celano, and F. Miao, “Nanoscale characterization of resistive switching using advanced conductive atomic force microscopy based setups,” *Journal of Electroceramics*, vol. 39, no. 1-4, pp. 94–108, 2017.

- [239] M. Vos, X. Liu, P. Grande, S. Nandi, D. Venkatachalam, and R. Elliman, “The use of electron rutherford backscattering to characterize novel electronic materials as illustrated by a case study of sputter-deposited NbO_x films,” *Nuclear Instruments and Methods in Physics Research Section B: Beam Interactions with Materials and Atoms*, vol. 340, pp. 58–62, 2014.
- [240] J. P. Strachan, J. J. Yang, R. Münstermann, A. Scholl, G. Medeiros-Ribeiro, D. R. Stewart, and R. S. Williams, “Structural and chemical characterization of TiO₂ memristive devices by spatially-resolved NEXAFS,” *Nanotechnology*, vol. 20, no. 48, p. 485701, 2009.
- [241] J. P. Strachan, D. B. Strukov, J. Borghetti, J. J. Yang, G. Medeiros-Ribeiro, and R. S. Williams, “The switching location of a bipolar memristor: chemical, thermal and structural mapping,” *Nanotechnology*, vol. 22, no. 25, p. 254015, 2011.
- [242] S. Li, X. Liu, S. K. Nandi, D. K. Venkatachalam, and R. G. Elliman, “Temperature dependence of threshold switching in NbO_x thin films,” in *Conference on Optoelectronic and Microelectronic Materials & Devices*, pp. 138–140, 2014.
- [243] J. Wang and S. S. Nonnenmann, “Area-dependent electroforming and switching polarity reversal across TiO₂/Nb:SrTiO₃ oxide interfaces,” *Journal of Materials Science*, vol. 52, no. 11, pp. 6469–6475, 2017.
- [244] A. Chen, “Area and thickness scaling of forming voltage of resistive switching memories,” *IEEE Electron Device Letters*, vol. 35, no. 1, pp. 57–59, 2014.
- [245] J. Leroy, A. Crunteanu, A. Bessaudou, F. Cosset, C. Champeaux, and J.-C. Orlianges, “High-speed metal-insulator transition in vanadium dioxide films induced by an electrical pulsed voltage over nano-gap electrodes,” *Applied Physics Letters*, vol. 100, no. 21, p. 213507, 2012.
- [246] S. Kumar, Z. Wang, X. Huang, N. Kumari, N. Davila, J. P. Strachan, D. Vine, A. D. Kilcoyne, Y. Nishi, and R. S. Williams, “Conduction channel formation and dissolution due to oxygen thermophoresis/diffusion in hafnium oxide memristors,” *ACS Nano*, vol. 10, no. 12, pp. 11205–11210, 2016.
- [247] Z. Cheng, A. Weidenbach, T. Feng, M. B. Tellekamp, S. Howard, M. J. Wahila, B. Zivasatienraj, B. Foley, S. T. Pantelides, and L. F. Piper, “Diffusion-driven ultralow thermal conductivity in amorphous Nb₂O₅ thin films,” *Physical Review Materials*, vol. 3, no. 2, p. 025002, 2019.

- [248] K. Chopra, "Avalanche-induced negative resistance in thin oxide films," *Journal of Applied Physics*, vol. 36, no. 1, pp. 184–187, 1965.
- [249] S. K. Nandi, S. Li, X. Liu, and R. G. Elliman, "Temperature dependent frequency tuning of NbO_x relaxation oscillators," *Applied Physics Letters*, vol. 111, no. 20, p. 202901, 2017.
- [250] F. Chudnovskii, L. Odynets, A. Pergament, and G. Stefanovich, "Electroforming and switching in oxides of transition metals: The role of metal-insulator transition in the switching mechanism," *Journal of Solid State Chemistry*, vol. 122, no. 1, pp. 95–99, 1996.
- [251] H. Shimizu, H. Sato, S. Nishimura, and M. Honda, "Electrical properties of anodically oxidized Nb₂O₅ and Si-doped Nb₂O₅ films," *Japanese Journal of Applied Physics*, vol. 44, no. 9R, p. 6664, 2005.
- [252] B. Ihsan, "Thermochemical data of pure substances," *VCH Verlagsgesellschaft mbH, Weinheim (Federal Republic of Germany) VCH Publishers, Inc., New York, NY (USA)*, vol. 934, p. 587, 1995.
- [253] N. Iosad, G. Ruis, E. Morks, A. Morpurgo, N. Van Der Pers, P. Alkemade, and V. Sivel, "Dielectric response of sputtered transition metal oxides," *Journal of Applied Physics*, vol. 95, no. 12, pp. 8087–8091, 2004.
- [254] J. Robertson, "High dielectric constant oxides," *The European Physical Journal-Applied Physics*, vol. 28, no. 3, pp. 265–291, 2004.
- [255] E. Hildebrandt, J. Kurian, M. M. Müller, T. Schroeder, H.-J. Kleebe, and L. Alff, "Controlled oxygen vacancy induced p-type conductivity in HfO_{2-x} thin films," *Applied Physics Letters*, vol. 99, no. 11, p. 112902, 2011.
- [256] C. D. Landon, R. H. Wilke, M. T. Brumbach, G. L. Brennecke, M. Blea-Kirby, J. F. Ihlefeld, M. J. Marinella, and T. E. Beechem, "Thermal transport in tantalum oxide films for memristive applications," *Applied Physics Letters*, vol. 107, no. 2, p. 023108, 2015.
- [257] L. Cojocaru, T. Costea, and I. Negoescu, "Electrical properties of non-stoichiometric oxides of CrO₃-Cr₂O₃ systems," *Zeitschrift für Physikalische Chemie*, vol. 60, no. 1-6, pp. 152–158, 1968.

- [258] J. M. Gallego and C. B. Thomas, "Preparation and characterization of thin films of NbO₂," *Thin Solid Films*, vol. 98, no. 1, pp. 11–22, 1982.
- [259] S. Springer, P. Schmid, R. Sanjines, and F. Levy, "Morphology and electrical properties of titanium oxide nanometric multilayers deposited by DC reactive sputtering," *Surface and Coatings Technology*, vol. 151, pp. 51–54, 2002.
- [260] Z. Wang, S. Kumar, H.-S. P. Wong, and Y. Nishi, "Effect of thermal insulation on the electrical characteristics of NbO_x threshold switches," *Applied Physics Letters*, vol. 112, no. 7, p. 073102, 2018.
- [261] A. Beaumont, J. Leroy, J.-C. Orlianges, and A. Crunteanu, "Current-induced electrical self-oscillations across out-of-plane threshold switches based on VO₂ layers integrated in crossbars geometry," *Journal of Applied Physics*, vol. 115, no. 15, p. 154502, 2014.
- [262] M. Son, J. Lee, J. Park, J. Shin, G. Choi, S. Jung, W. Lee, S. Kim, S. Park, and H. Hwang, "Excellent selector characteristics of nanoscale VO₂ for high-density bipolar ReRAM applications," *IEEE Electron Device Letters*, vol. 32, no. 11, pp. 1579–1581, 2011.
- [263] S. M. Bohaichuk, S. Kumar, G. Pitner, C. J. McClellan, J. Jeong, M. G. Samant, H.-S. P. Wong, S. S. Parkin, R. S. Williams, and E. Pop, "Fast spiking of a Mott VO₂-Carbon Nanotube composite device," *Nano Letters*, vol. 19, no. 10, pp. 6751–6755, 2019.
- [264] X. Zhou, D. Gu, Y. Li, H. Qin, Y. Jiang, and J. Xu, "A high performance electroformed single-crystallite VO₂ threshold switch," *Nanoscale*, vol. 11, no. 45, pp. 22070–22078, 2019.
- [265] D. Li, A. A. Sharma, N. Shukla, H. Paik, J. M. Goodwill, S. Datta, D. G. Schlom, J. A. Bain, and M. Skowronski, "On-state evolution in lateral and vertical VO₂ threshold switching devices," *Nanotechnology*, vol. 28, no. 40, p. 405201, 2017.
- [266] V. Atuchin, I. Kalabin, V. Kesler, and N. Pervukhina, "Nb 3d and O 1s core levels and chemical bonding in niobates," *Journal of Electron Spectroscopy and Related Phenomena*, vol. 142, no. 2, pp. 129–134, 2005.
- [267] S. Hashimoto and A. Tanaka, "Alteration of Ti 2p XPS spectrum for titanium oxide by low-energy Ar ion bombardment," *Surface and Interface Analysis: An International Journal devoted to the development and application of techniques for the analysis of surfaces, interfaces and thin films*, vol. 34, no. 1, pp. 262–265, 2002.

- [268] M. Atashbar, H. Sun, B. Gong, W. Wlodarski, and R. Lamb, “XPS study of Nb-doped oxygen sensing TiO_2 thin films prepared by sol-gel method,” *Thin Solid Films*, vol. 326, no. 1-2, pp. 238–244, 1998.
- [269] A. K. Rumaiz, B. Ali, A. Ceylan, M. Boggs, T. Beebe, and S. I. Shah, “Experimental studies on vacancy induced ferromagnetism in undoped TiO_2 ,” *Solid State Communications*, vol. 144, no. 7-8, pp. 334–338, 2007.
- [270] H. Y. Jeong, J. Y. Lee, M. Ryu, and S. Choi, “Bipolar resistive switching in amorphous titanium oxide thin film,” *Physica Status Solidi (RRL)-Rapid Research Letters*, vol. 4, no. 1-2, pp. 28–30, 2010.
- [271] C. Funck, S. Hoffmann-Eifert, R. Waser, and S. Menzel, “Simulation of threshold switching based on an electric field induced thermal runaway,” in *International Conference of Simulation on Semiconductor Processes and Devices (SISPAD)*, pp. 319–322, IEEE, 2016.
- [272] N. Alimardani, J. M. McGlone, J. F. Wager, and J. F. Conley Jr, “Conduction processes in metal-insulator-metal diodes with Ta_2O_5 and Nb_2O_5 insulators deposited by atomic layer deposition,” *Journal of Vacuum Science & Technology A: Vacuum, Surfaces, and Films*, vol. 32, no. 1, p. 01A122, 2014.
- [273] A. Velichko, M. Belyaev, V. Putrolaynen, A. Pergament, and V. Perminov, “Switching dynamics of single and coupled VO_2 -based oscillators as elements of neural networks,” *International Journal of Modern Physics B*, vol. 31, no. 2, p. 1650261, 2017.
- [274] S. Menzel, S. Tappertzhofen, R. Waser, and I. Valov, “Switching kinetics of electrochemical metallization memory cells,” *Physical Chemistry Chemical Physics*, vol. 15, no. 18, pp. 6945–6952, 2013.